TESE DE DOUTORADO Nº 339

OFFLINE SIGNAL PROCESSING TOOLS FOR ELECTROMAGNETIC COMPATIBILITY APPLICATIONS

Artur Nogueira de São José

DATA DA DEFESA: 30/09/2020

Artur Nogueira de São José

Offline signal processing tools for electromagnetic compatibility applications

Belo Horizonte, Brazil

September, 2020

Universidade Federal de Minas Gerais

Escola de Engenharia

Programa de Pós-Graduação em Engenharia Elétrica

OFFLINE SIGNAL PROCESSING TOOLS FOR ELECTROMAGNETIC COMPATIBILITY APPLICATIONS

Artur Nogueira de São José

Tese de Doutorado submetida à Banca Examinadora designada pelo Colegiado do Programa de Pós-Graduação em Engenharia Elétrica da Escola de Engenharia da Universidade Federal de Minas Gerais, como requisito para obtenção do Título de Doutor em Engenharia Elétrica.

Orientador: Ricardo Luiz da Silva Adriano
Coorientadora: Úrsula do Carmo Resende

Belo Horizonte - MG

Setembro de 2020

Artur Nogueira de São José

Offline signal processing tools for electromagnetic compatibility applications

A dissertation submitted in partial fulfillment of the requirements for the degree of Doctor in Electrical Engineering at the Federal University of Minas Gerais.

Federal University of Minas Gerais

Graduate Program in Electrical Engineering

Supervisor: Prof. Dr. Ricardo Luiz da Silva Adriano
Co-supervisor: Prof. Dr. Úrsula do Carmo Resende

Belo Horizonte, Brazil
September, 2020

S239o São José, Artur Nogueira de.
Offline signal processing tools for electromagnetic compatibility applications [recurso eletrônico] / Artur Nogueira de São José. - 2020.
1 recurso online (127 f. : il., color.) : pdf.

Orientador: Ricardo Luiz da Silva Adriano.
Coorientador: Úrsula do Carmo Resende.

Tese (doutorado) - Universidade Federal de Minas Gerais, Escola de Engenharia.

Apêndices: f. 106-127.

Bibliografia: f. 99-105.
Exigências do sistema: Adobe Acrobat Reader.

1. Engenharia elétrica - Teses. 2. Compatibilidade eletromagnética - Teses. 3. Interferência eletromagnética - Teses. I. Adriano, Ricardo Luiz da Silva. II. Resende, Úrsula do Carmo. III. Universidade Federal de Minas Gerais. Escola de Engenharia. IV. Título.

CDU: 621.3(043)

Ficha catalográfica: Biblioteca Prof. Mário Werneck, Escola de Engenharia da UFMG.

"Offline Signal Processing Tools For Electromagnetic Compatibility Applications"

Artur Nogueira de São José

Tese de Doutorado submetida à Banca Examinadora designada pelo Colegiado do Programa de Pós-Graduação em Engenharia Elétrica da Escola de Engenharia da Universidade Federal de Minas Gerais, como requisito para obtenção do grau de Doutor em Engenharia Elétrica.

Aprovada em 30 de setembro de 2020.

Por:

____
Prof. Dr. Ricardo Luiz da Silva Adriano
DEE (UFMG) - Orientador

____
Prof. Dr. Úrsula do Carmo Resende
DEPTO DE ENGENHARIA ELETRICA
(CEFET MG) – Coorientadora

____
Prof. Dr. Sandro Trindade Mordente Gonçalves
DEPTO DE ENGENHARIA ELETRICA (CEFET MG)

____
Dr. Virginie Deniau
LEOST (Université Gustave Eiffel)

____
Prof. Dr. Cássio Guimarães Lopes
Departamento de Engenharia de Sistemas Eletrônicos (USP)

____
Prof. Dr. Adriano Vilela Barbosa
DELT (UFMG)

I dedicate this work to my aunt Zilma Reis. Her devotion to science and research, combined with her will of making technological innovations accessible to everyone, are definitely an inspiration to me.

Acknowledgements

This work would not have been possible without the precious help that I received from many people.

I would like to thank my parents, Paulo and Lilia, my sister Carolina and my brother Hugo for giving me all the support and encouragement I needed to invest my time and (scarce) money on a scientific career. I know you completely understood my absences during this period in order to focus on my studies and such a support was very important to me. I am very greatful for that!

The success of a Ph.D. project is strongly dependent on the help the researcher receives from his supervisors. In this sense, I was fortunate to have three brilliant supervisors. It was an honor and a privilege to work with Professors Ricardo Adriano and Úrsula Resende during these four years and with Dr. Virginie Deniau during my seven-month internship at the IFSTTAR.

The always precise technical comments from Professor Ricardo Adriano were definitely crucial in the process of turning my initial ideas into concrete results. In addition to his technical support, he was always concerned about my work conditions, either by encouraging me to interact more with other researchers, or by constantly asking me about my scholarship (and making all he could to ensure I would not have problems with it) or by simply making jokes. Furthermore, without his constant encouragement about going to France for a research internship, I would never have had such a great opportunity. So thank you, Professor Ricardo, for all your technical and non-technical support, for sharing with me a little of your excellent research background and for accepting me as your Ph.D. student.

The importance of my co-supervisor, Professor Úrsula Resende, in my career is undeniable. She has supervised me since 2012, when I started my undergraduate final project. It is a pleasure to work with her because she is as passionate about research as me. So it is natural that we have a very good connection. She is a very hard-working person and being around her makes me more and more motivated. Thank you very much, Professor Úrsula, for accepting me as your student for all these years and for giving me all the support and incentives that I needed.

I would like to take this opportunity to express how grateful I am to Dr. Virginie Deniau. Since the very first contact I had with her, she was very receptive and kind to me. During my internship at the IFSTTAR, she not only helped me with the lab experiments, paper writing and other research activities but also encouraged me to attend conferences and other interesting events. Finally, I thank her for receiving me in France and for giving me the opportunity of working on the very exciting IEMI topic.

I cannot forget all the people who helped me during numerous measurement campaigns. The handmade stand for antennas produced by Mr. Henrique Bianco Pinheiro, a lab technician from CEFET-MG, was as excellent solution to the antennas alignment problem I was facing. Mr. Christophe Rosinki, a research engineer from IFSTTAR, not only helped me in several lab experiments, but also kindly let me use his LabVIEW routine in order to more easily acquire measurement data. Finally, Mr. Christophe Gransart, a researcher from IFSTTAR, saved my life by establishing the communication between GNU Radio and the HackRF units. His support regarding the installation and configuration of this software was crucial for my last measurement campaign, since I would definitely not have been able to do it by myself.

During my stay in Lille (France), I was warmly received and guided by a few people without whom everything would have been more difficult for me. Since my very first day there, I was supported by my friends Dalay, Fabrício and Thaísa. They made sure that everything was OK for me, from my cell phone account to the pillows and bed sheets in my appartment! Besides, I was hosted by Fabrício for a few days at his house in Valenciennes and I am deeply grateful for that. I also have to mention all the guidance and kindness from my friend Malick, who helped me a lot with daily life issues and turned the workplace into a very pleasant and funny place to be. Besides, I was lucky of having Caio and Malu living so close to me at the *Maison Internationale des Chercheurs*. We shared very good moments during this time. I am very grateful to all of you, guys!

I would like to thank Dr. Jonathan Villain, from IFSTTAR, and Professor Lucas Batista, from DEE/UFMG, for the very productive discussions about the PSO algorithm. I also thank Juliano Mologni, an engineer from ANSYS, for his support with the electromagnetic simulations in our 2017 GEMCCON paper. I am grateful to Saulo Fróes, from IBGE, author of the DAE-2 technique. He gently provided me with important information about his method, which I used in this research.

I would like to thank my friends Magno Menezes and Arnaud Colin for the fruitful technical discussions (whether or not related to my Ph.D. research), jokes and *good EMC practices.* I am grateful to my cousin Paula Sales and her husband Cadu for all the support they gave me before, during and after my internship in France concerning my CAPES scholarship and other related questions. I thank my friend Maria Contreras for kindly lending me her antenna prototypes so I could evaluate my filtering methodologies and also

for her contributions to our 2017 GEMCCON paper.

Finally, it was of an immense importance all the feedback comments I received from Professors Wallace Boaventura, Hilton Mota, Adriano Vilela and Cassio Lopes, during my Qualifying Exam. Their comments served as an initial validation of my research and as a guide for the second half of my Ph.D. In special, I thank Professor Adriano Vilela, for the Signal Processing classes and for all the support he gave me at that time, during which he many times patiently received me in his office in order to clarify all my questions. I am also very grateful to Professor Cassio Lopes, from the University of Sao Paulo, for quickly and thoroughly answering all my e-mails concerning the adaptive filters.

This study was financed in part by the Coordenação de Aperfeiçoamento de Pessoal de Nível Superior - Brasil (CAPES) - Finance Code 001, by FAPEMIG and by IFSTTAR.

Abstract

The electromagnetic compatibility field has gained more and more attention from both academia and industry in the past few years. Following its basic design, testing and mitigation procedures is essential to ensure the correct operation of products and complex infra-structures. In this work, we deal with scenarios where these classical procedures are not sufficient to avoid interference problems or are not accessible due to high implementation costs. To explore this subject, we propose two case studies: antenna calibration in non-ideal test sites and security of railway communications under jamming attacks. To deal with these issues, we developed a new technique based on principles of design and analysis of experiments, called DAE-1, and two new signal processing tools, called ASP-1 and ASP-2. The first two (DAE-1 and ASP-1) were applied to the antenna calibration problem, while the last one (ASP-2) was applied to the intentional electromagnetic interference problem. We designed these tools to be easily handled by an electromagnetic compatibility professional without a signal processing background. In particular, ASP-1 has two routines that automatically set the adaptive filters and time gating parameters. The DAE-1 and ASP-1 techniques were validated after an extensive process involving experimental measurements in four different test sites, three different antennas and a benchmark analysis with two state-of-the-art approaches. In our analyses, we compared three antenna gain curves with anechoic chamber measurements. A performance metric based on the Pearson correlation coefficient indicates performance gains that range from 27% to 30% for DAE-1 and from 21% to 25% for ASP-1. Although with smaller gains, ASP-1 significantly reduces the total test time when compared to DAE-1. Then, we artificially increased the interference levels and evaluated ASP-1 under two different configurations, one of them being inspired by a state-of-the-art approach. The performance gains ranged from 15% to 25%. Finally, we used a computational environment to validate the ASP-2 technique. To do so, we generated a simplified version of the global system for mobile communications-railway (GSM-R) signal with and without jamming contributions. During this stage, we noticed an average bit error rate reduction for signal-to-jamming ratios (SJR) ranging from -2.77 dB to 1.16 dB thanks to the ASP-2 algorithm. These reductions are approximately 10 % when the SJR is -2.77 dB. The threshold SJR level (above which the GSM-R communication can be lost) changed from approximately -0.84 dB to -1.95 dB, expanding thus the operating range of the GSM-R system. This suggests that the adaptive line enhancer is a promising tool to deal with jamming attacks.

Keywords: Electromagnetic Compatibility, Adaptive Filtering, Time Gating, Particle Swarm Optimization, Intentional Electromagnetic Interference, Antenna Calibration.

List of Figures

List of Tables

List of Algorithms

List of abbreviations and acronyms

ACF	Autocorrelation Function
ADC	Analog-to-Digital Converter
AF	Adaptive Filtering
AiP	Antenna-in-Package
AiM	Antenna-in-Module
ALE	Adaptive Line Enhancer
ANC	Adaptive Noise Canceller
AP	Access Point
ASP	Adaptive Signal Processing
AUT	Antenna Under Test
BER	Bit Error Rate
BI	Beacon Interval
CFO	Carrier Frequency Offset
CISPR	*Comité International Spécial des Perturbations Radioélectriques*
CW	Continuous Wave
DAE	Design and Analysis of Experiments
DL	Downlink
DOA	Direction-of-Arrival
DOE	Design of Experiments
DoS	Denial of Service
DR	Data reuse

DSP	Digital Signal Processing
DUT	Device Under Test
EIRENE	European Integrated Radio Enhanced NEtwork
EM	Electromagnetic
EMC	Electromagnetic Compatibility
EMI	Electromagnetic Interference
ERTMS	European Rail Traffic Management System.
EVM	Error Vector Magnitude
FDMA	Frequency Division Multiple Access
FM	Frequency Modulation
FRMCS	Future Railway Mobile Communication System
GMSK	Gaussian Minimum Shift Keying
GPR	Ground-Penetrating Radar
GPS	Global Positioning System
GSM	Global System for Mobile Communications
GSM-R	Global System for Mobile Communications -– Railway
GTEM	Gigahertz Transverse Electromagnetic
HSR	High-Speed Railways
IEMI	Intentional Electromagnetic Interference
IFFT	Inverse Fast Fourier Transform
IFSTTAR	*Institut Français des Sciences et Technologies des Transports, de l'Aménagement et des Réseaux*
ISO	International Organization for Standardization
LEOST	*Laboratoire Électronique Ondes et Signaux pour les Transports*
LTE-R	Long-Term Evolution – Railway
MSK	Minimum Shift Keying

NLMS	Normalized Least Mean Squares
OATS	Open Area Test Site
OFDM	Orthogonal Frequency Division Multiplexing
PSO	Particle Swarm Optimization
SAR	Synthetic-Aperture Radar
SAS	Smart Antenna System
SDR	Software-Defined Radio
SJR	Signal-to-Jamming Ratio
SNR	Signal-to-Noise Ratio
SOLT	Short-Open-Load-Through
STFT	Short-Time Fourier Transform
TDMA	Time Division Multiple Access
TG	Time Gating
UFMG	*Universidade Federal de Minas Gerais*
UIC	*Union Internationale des Chemins de fer*
UL	Uplink
VCO	Voltage-Controlled Oscillator
VNA	Vector Network Analyzer
VoIP	Voice over Internet Protocol
VSWR	Voltage Standing Wave Ratio

List of symbols

AUT1	A directive patch antenna
AUT2	An omnidirectional patch antenna
AUT3	A directive horn antenna
AUT4	A directive patch antenna
ASP-1	Signal processing technique proposed to solve the antenna calibration problem
ASP-2	Signal processing technique proposed to solve the intentional electromagnetic interference problem
B	Frequency resolution of a vector network analyzer
BT	Product between the bandwidth of a gaussian filter in a gaussian minimum shift keying modulator and the bit period
Cha1	Anechoic Chamber from the Federal University of Minas Gerais, Brazil
Cha2	Anechoic Chamber from the French Institute of Science and Technology for Transport, Development and Networks, France
$cov(X, Y)$	Covariance between two random variables X and Y
DAE-1	Design and analysis of experiments-based technique proposed to solve the antenna calibration problem
DAE-2	Design and analysis of experiments-based technique proposed by Froes *et al* (2019) to solve the antenna calibration problem
d	Distance between two antennas in a calibration procedure
d_x	Distance between two antennas in a calibration procedure
d_y	Distance between two antennas in a calibration procedure

$D(\theta, \phi)$	Antenna directivity evaluated at the direction given by the (θ, ϕ) solid angle
e	Error signal of an adaptive filter
$\mathbb{E}\{.\}$	Expectation operator
f	A function that is inversely proportional to the filter performance
g	An index that identifies the current generation in a PSO implementation
$\mathbf{G}$	Antenna gain curve
$G(\theta, \phi)$	Antenna gain evaluated at the direction given by the (θ, ϕ) solid angle
$G_{AUT}(dB)$	Peak gain of the antenna under test, expressed in dB
$\mathbf{G}_{ref}$	A reference antenna gain curve
$\mathbf{h}$	Adaptive filter impulse response, also known as the *weights vector*
h_A	Antenna height used during a calibration procedure
h_B	Antenna height used during a calibration procedure
h_1	Antenna height used during a calibration procedure
h_2	Antenna height used during a calibration procedure
$H(z)$	Adaptive filter transfer function in the ANC and ALE configurations
$H_1(z)$	Adaptive filter transfer function in the system identification configuration
$H_2(z)$	Unknown system's transfer function in the system identification configuration
IQ	In-Phase and Quadrature
j_1	Measurement noise
j_1^{Δ}	Delayed version of j_1, Δ being the lag
$\widehat{j_1}$	Measurement noise estimate
j_2	Noise floor sample
K	Number of signal replicates plus 1 in a data reuse process
k	Boltzman constant

L	Order (length) of a NLMS filter or the total number of a signal samples
lags	Time shift used to plot the autocorrelation function
Lab1	Applied Electromagnetics Laboratory from the Federal University of Minas Gerais, Brazil
Lab2	Electromagnetic Compatibility Laboratory from the French Institute of Science and Technology for Transport, Development and Networks, France
M	Measurement containing useful signal, multipath, electromagnetic interference and random noise
$\overline{M}$	Averaged measurement containing useful signal, multipath, electromagnetic interference and random noise, obtained from N realizations
n	Discrete-time index
N	Number of experimental runs
N_1	Number of multipath sources influencing a measurement
N_2	Number of electromagnetic interference sources influencing a measurement
N_3	Number of random sources influencing a measurement
P_{in}	Antenna input power
P_{rad}	Antenna radiated power
P_{TN}	Thermal noise power
$P(.)$	Probability function
Q	Sum of electromagnetic interference, multipath and random noise estimates
$\mathrm{RES}_{EMI}^{(A)}$	Residual term associated with electromagnetic interference, inherent to the DAE-1 technique
$\mathrm{RES}_{MP}^{(A)}$	Residual term associated with multipath, inherent to the DAE-1 technique
$\mathrm{RES}_{RN}^{(A)}$	Residual term associated with random noise, inherent to the DAE-1 technique

$\mathrm{RES}_{EMI}^{(B)}$	Residual term associated with electromagnetic interference, inherent to the ASP-1 and ASP-2 techniques
$\mathrm{RES}_{MP}^{(B)}$	Residual term associated with multipath, inherent to the ASP-1 and ASP-2 techniques
$\mathrm{RES}_{RN}^{(B)}$	Residual term associated with random noise, inherent to the ASP-1 and ASP-2 techniques
s	Useful signal
s^{Δ}	Delayed version of s, Δ being the lag
Sa/Sym	Samples per symbol
S_{11}	Reflection parameter, also known as the *return loss*
S_{12}	Transmission parameter, also known as the *insertion loss*
$S_{12}(dB)$	Transmission parameter magnitude expressed in dB
$\widehat{S}$	Useful signal estimate
$\overline{S}$	Averaged useful signal obtained from N realizations
T	Temperature
v_1	Useful voice signal coming from speaker 1
$v_{1,echo}$	Echo associated with the useful voice signal coming from speaker 1
$\widehat{v}_{1,echo}$	Estimate of the echo associated with the useful voice signal coming from speaker 1
v_2	Useful voice signal coming from speaker 2
X	Discrete random variable
x_i	i^{th} observation of a discrete random variable
$\mathbf{x}$	A sample of X, defined as the following set of observations: $\mathbf{x} = \{x_1, x_2, \cdots, x_N\}$
$U(\theta, \phi)$	Antenna radiated power evaluated at the direction given by the (θ, ϕ) solid angle
α_i	Attenuation introduced by the i^{th} multipath source
$\widehat{\alpha}_i$	Estimate of the attenuation introduced by the i^{th} multipath source

θ	A given statistical parameter that characterizes the random variable X
$\widehat{\theta}$	A point estimate of θ, provided by an estimator
$\widehat{\Theta}$	A point estimator, *i.e.* a function of the observations, $f(\mathbf{x})$, that returns $\widehat{\theta}$
θ_i	Phase lag introduced by the i^{th} multipath source
$\widehat{\theta}_i$	Estimate of the phase lag introduced by the i^{th} multipath source
η_i	i^{th} electromagnetic interference source
$\widehat{\eta}_i$	Estimate of the i^{th} electromagnetic interference source
$\overline{\eta}$	Averaged electromagnetic interference obtained from N realizations
ϵ	Regularization parameter of a NLMS filter
ϵ_i	i^{th} random noise source
$\widehat{\epsilon}_i$	Estimate of the i^{th} random noise source
$\overline{\epsilon}$	Averaged random noise obtained from N realizations
Ω	Sample space associated with a discrete random variable
$\overline{\Theta}$	Mean estimator
μ	Step-size of a NLMS filter
μ_0	A constant bigger than 0 and smaller than 1 used to calculate the step-size of a NLMS filter
Π	Number of frequency samples used to plot a gain curve
$\nabla(.)$	Gradient operator
$\widehat{\nabla}(.)$	Gradient estimate
$(.)^H$	Hermitian operator
$(.)\|_{2<f<3GHz}$	Evaluation over the $2 < f < 3$ GHz frequency band
$(.)\|_{2.4GHz}$	Evaluation only at 2.4GHz
$\Delta\phi$	Phase difference between the line-of-sight and multipath signals in a radiofrequency transmission considering the two-ray model

Δl	Path difference (in distance units) between the line-of-sight and multipath signals in a radiofrequency transmission considering the two-ray model
λ	Wavelength
ϕ_{MP_A}	Phase of the multipath signal "seen" by the receiving antenna at the height h_A
ϕ_{MP_B}	Phase of the multipath signal "seen" by the receiving antenna at the height h_B
$\rho(X, Y)$	Pearson correlation coefficient calculated from two random variables X and Y
ρ_X	Standard deviation of the random variable X
ρ_Y	Standard deviation of the random variable Y
Δ	Decorrelation parameter of an adaptive line enhancer
$z^{-\Delta}$	Delay block of an adaptive line enhancer

Contents

Chapter 1

Introduction

1.1 Context and motivations

Electromagnetism is increasingly present in people's daily life. To demonstrate this, one can give many practical examples. Among them, one can mention the use of electromagnetic (EM) energy by telecommunications companies. Most of them use antenna systems to wirelessly transmit EM waves containing audio, voice and other types of information to their customers – usually in addition to the traditional wired systems. However, the use of EM energy is not restricted to data transmission. Alternatively, it can be used to heat food in a microwave oven, to identify an object in a radar system, to name just a few.

Unfortunately, the EM energy can also be present in situations where it is unwanted. Mologni (1), for example, describes the effects of mobile telephony signals (an *agressor*) over an automotive sound system (a *victim*). Evidently, such a coupling is unintentional but it can happen if adequate electromagnetic interference (EMI) mitigation techniques are not incorporated into the victim system's design. In this particular example, the undesirable EM energy can induce acoustic noise on the speakers, which can interrupt a radio reception.

To avoid situations like this, manufacturers shall test their products before starting large-scale production. More specifically, the general rule to avoid EMI problems is to test prototypes according to electromagnetic compatibility (EMC) standards (2). Following these procedures does not ensure that the mentioned problems will not happen but it considerably reduces the probabilities.

In this work, we are particularly concerned with EMI problems which cannot be handled by the mentioned EMC standards. In order to demonstrate the existence of such scenarios and propose solutions to them, we bring two case studies for this investigation.

The first one refers to antenna calibration in non-ideal test sites. Antenna calibration is a test procedure that allows manufacturers to know if their prototypes follow the design requirements. This is only possible when one can establish a measurement system which informs about the antenna properties without registering other phenomena. If this premise is not verified, the measurement data is not reliable as one cannot make a distinction between useful antenna signals and noise floor.

In order to meet the above requirement, a test site must offer EM isolation among many other features. Its compliance can be checked based on the criteria defined by antenna calibration standards such as ANSI C63.5-2017 (3) (see Section J.2.1.3). These conditions can in turn restrict the number of certified labs in a given region, since the required infra-structure can be very expensive. Consequently, many small manufacturers and research laboratories with restricted budget cannot use their facilities to test antennas (either developed by them or commercial ones). In this context, it is desirable to develop methodologies that allow these companies and labs to run pre-compliance tests with more reliable results.

The second case study concerns the malicious use of jamming devices in railway environments. In such a situation, one may want to disturb important railway communication systems in order to cause trouble. To do so, these devices radiate EM disturbances within the victim system's operating frequency band. Therefore, this equipment produces intentional electromagnetic interference (IEMI) to significantly increase the bit error rates (BERs) of the victim's communication systems. In the past few decades, the use of these devices have been widely reported - a survey can be found in (4).

The major challenge when dealing with IEMI is the unpredictability of the attack. When manufacturers test their prototypes according to the EMC standards, the device immunity against radiated EM disturbances is indeed verified. Nevertheless, the *radiated immunity* test is based on the power and frequencies related to known disturbances, such as amplitude-modulated signals coming from radio stations – in (5), one can find a discussion about the radiated immunity test. Jamming devices, on the other hand, are not designed to follow any standards so their power, waveform and other characteristics are not previously known. Furthermore, these devices are usually portable so a person can walk with it following a random path in the neighborhood of the victim system's receiving or transmitting antenna. Thus, the signal-to-jamming ratio (SJR) can vary with time in an unpredictable way, turning the mitigation a challenging task.

The main goal of our research is to find alternatives for these scenarios where the classical EMC solutions are not accessible. In the next section, we give an overview of the most recent approaches on EMI mitigation. More specifically, we focus our attention on signal processing techniques applied to antenna measurements and IEMI mitigation.

1.2 Literature review

1.2.1 Antenna measurements

Antenna measurements refer to the set of equipment and procedures necessary to estimate certain properties of an antenna. According to Kummer and Gillespie (6), there were two decisive moments in history for the development of such techniques: the World War II and the American space program in the 1960's. However, the authors point out that no big changes on the methods themselves were observed along the years. Instead, new equipment has been developed in order to increase the measurement accuracy – a topic that continues to attract the attention from the researchers.

Recent studies suggest that adaptive signal processing (ASP) techniques can be used to reduce the noise levels in antenna measurements and other related tests. Specifically, adaptive filters have been recently applied to the *radiated emissions* test. In this test, the main goal is to measure the EM emissions of a device under test (DUT). However, in open areas containing a significant number of EM scatterers and EMI sources, it is not possible to distinguish the actual DUT emissions from the noise floor.

To solve this problem, some authors propose the use of real-time adaptive filtering techniques to recover the actual DUT emissions. For example, Frech (7; 8) proposes a pre-filtering real-time acquisition system that operates in the time domain. This approach is faster than the traditional frequency-domain acquisition for a broadband measurement. On the other hand, Sheng (9) proposes to split the broadband measurements into several narrower band signal components through a wavelet transform unit. This leads to a parallel processing of the resulting components, which increases the overall efficiency of the signal processing structure. Similar approaches can be found on (10; 11).

Another recent research topic involving digital signal processing (DSP) techniques applied to the antenna field refers to the concept of *smart antenna systems*[1] (SAS). These systems are based on antenna arrays, *i.e.* on sets of individual antennas forming specific arrangements. Furthermore, the individual antennas can be electronically controlled in order to produce a customized pattern (either for transmission or reception), as exemplified in Fig. 1.1. The control strategy used in these cases is based on manipulating the amplitudes and phases of the signals that enter or leave the individual antennas (13).

Figure 1.1 illustrates a SAS composed of a given number of individual antennas connected to a radiofrequency (RF) front-end (modulators/demodulators, filters *etc*), an analog-to-digital converter (ADC) and a DSP unit. The latter is responsible to identify the location of a mobile user, Θ – also known as direction-of-arrival (DOA) – and to use this information to produce an antenna pattern directed towards this user. In general, the SAS

---

[1] This is a vast research field that encompasses various types of technologies such as beamforming, phased arrays, to name just a few. In (12), one can find most of these definitions as well as a glossary.

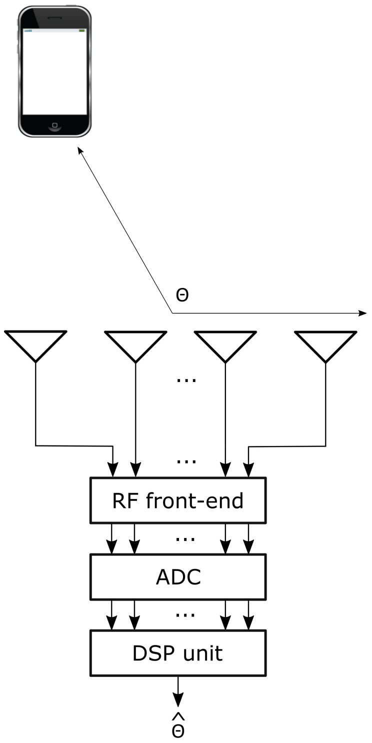

Figure 1.1 – Example of a smart antenna system, composed of a set of individual antennas and a receiving/transmitting/processing circuitry. In this illustration, the mobile user is represented by a cell phone and by the corresponding DOA, Θ. Based on $\widehat{\Theta}$, a DOA estimation, the DSP unit can generate a customized antenna pattern for this user. Adapted from (14).

can identify any signal nearby that reaches the antenna array. Nevertheless, one can find in the literature algorithms that distinguish between useful and non-useful signals (15).

Because the antenna pattern is electronically controlled, the calibration of a SAS is particularly challenging. In such a scenario, the calibration process must identify and compensate for any spurious environmental contributions that can alter the desired antenna pattern. For example, in (16) the authors propose the addition of a calibration antenna to the original array. This antenna sends and receives calibration signals which are used by the DSP processor to compensate for phase shifts between the individual antennas of the array – according to Cordeau (17), these phase shifts can affect the DOA estimation. In (14), the authors propose a SAS calibration methodology based on neural networks. According to them, the proposed technique has low complexity and therefore is suitable for real-time applications. Furthermore, it can be applied to any antenna array topology.

In (18), the authors describe a scenario where a SAS is used to monitor elderly people. In this particular case, the DOA represents the monitored person's location in an indoor environment. The authors propose a calibration technique to work in such circumstances despite the presence of multipath. This technique uses channel information obtained from a known DOA to generate the correct positioning estimates in other directions. In (19), the authors describe the difficulties in characterizing the antenna pattern of a SAS system installed in a synthetic-aperture radar (SAR) satellite. According to the authors, most techniques used with this purpose have limited accuracy or retrieve only the main lobe of the antenna pattern. The proposed technique is based on already available data coming from an electronic module installed on-board. It can recover the entire antenna pattern, *i.e.* both main and side lobes.

It is also important to highlight the emerging antenna manufacturing processes aiming at 5G technologies and beyond. Most of them explore the mm-wave frequencies and use modern packaging processes to incorporate the antennas into the chips. Technologies such as antenna-in-package (AiP) and antenna-in-module (AiM) offer reduced antenna sizes (20), which turns the process of measuring the electrical properties of such devices a challenging task. Therefore, the development of new calibration techniques for these integrated devices seems to be a promising research field (21).

In this work, we develop methodologies to retrieve an important antenna parameter: its gain. We do not deal with SAS, so we assume that the gain is constant even if we move the antennas or the interfering sources. During our investigations, we were inspired by all the state-of-the-art approaches above described. In particular, the works developed by Sheng (9) and Froes (22) were used in our benchmark analyses. By doing so, we compare our techniques with other related works.

1.2.2 Intentional electromagnetic interference

One of the most recent trends in telecommunications concerns the intense data exchange between a large number of devices and systems. Although a number of advantages can be derived from this concept, privacy and security remain important concerns. Nowadays, there are many different types of cyber-security attacks against wireless networks, each of them with a certain complexity, ability to not be detected by anti-jamming devices and to damage the target (23; 24; 25). These attacks usually present low power and aim to degrade the communication throughput or even cause a service disruption by an excessive number of requests – this is known as denial-of-service (DoS). Nevertheless, the wireless networks can also be subject to high-power attacks which can damage the electrical and electronic devices (26).

Modern European railway systems have incorporated several wireless technologies in the last decades. Such features aim to increase the performance of the train, enhance its autonomy by reducing the human intervention during operation, provide interoperability along the geographical borders and provide users with comfort and better services. According to Deniau (4), the railway system comprises a large number of communication networks, whose signals range in complexity from simple control-command information (*e.g.* track switches activation) to the continuous voice data exchange between train and base-station by means of the global system for mobile communications – railway (GSM-R) standard. These and other railway communication systems are all subject to attacks.

Villain (27) describes two possible attacks directed to the railway WiFi networks. The first one is a physical layer jamming attack which consists of low power electromagnetic emissions covering the downlink (DL) and/or uplink (UL) frequency bands. The second one is a protocol-based attack called man-in-the-middle. Lyamin (28) describes another potential protocol-based attack directed to a WiFi network. They describe a scenario where the positions and velocities of a group of cars in a smart road, also known as a *platoon*, are managed by a leading vehicle through the IEEE 802.11p standard. In this case, the attacks can affect the vehicular network dynamics and even cause collisions. The corruption of the same type of information is also described by Wu (29) but in a different context. The authors explore the use of jammers close to the balise, which is a device placed in certain positions on a railway track. When a train passes over such a device, a short-range communication between them is established. However, if this link is corrupted, the train speed control can be affected and so the safety of the passengers.

Throughout this research work, we investigate jamming attacks directed to the GSM-R physical layer. Related works explore both identification and mitigation techniques. For example, Mili *et al* propose two identification approaches. In (30), the authors propose statistical models for the channel in a normal situation (*i.e.* without jamming) and under attack, considering different jamming signal behaviors. On the other hand, in (31), they propose a real-time monitoring algorithm based on the error vector magnitude (EVM). The EVM is a metric of the digital transmission quality and is adopted by the authors as an indicator of jamming activity. Finally, Villain (27) proposes a machine learning-based algorithm which can not only identify such activities but also distinguish between physical layer and man-in-the-middle attacks.

Mitigation techniques for physical layer attacks usually involve power management, use of directional antennas and frequency hopping (23; 25). For example, Heddebaut (32) proposes a few mitigation techniques that include base-station adaptive power control and smart antenna-based approaches. They use simple propagation models to delineate critical zones within the GSM-R cells where the communication can be severely compromised or even lost.

In this work, we propose a signal processing technique to deal with jamming attacks directed to GSM-R networks. This is a relevant topic since the railway systems play a strategic role in many countries. Therefore, any disruption on this communication system can compromise the safety of a large number of people or even the integrity of products when it comes to cargo transport. Even though we conduct analyses based on the European railway system, the results obtained here are not restricted to it since high-speed railways (HSR) are present in many countries nowadays (33).

1.3 Objectives

This research emerged under the premises that (i) many EMI problems could be more efficiently solved with signal processing, as an alternative or a complement to the traditional EMC mitigation techniques; and (ii) most signal processing advances do not reach the EMC community. So, the first and more general objective of this work is to shorten the gap between the signal processing and electromagnetic compatibility fields.

In practical terms, we aim to develop signal processing tools to solve the previously mentioned antenna calibration and IEMI problems. More specific objectives include the incorporation of mechanisms that facilitate the use of these tools, since our main public is the EMC community. Therefore, the final user can be an EMC professional who does not necessarily have a signal processing background. Besides, we aim to develop techniques with improvements in terms of speed and accuracy when compared to other approaches reported in the recent literature.

In summary, these are the main objectives of this work:

- to develop signal processing algorithms and codes to enhance the quality of antenna calibration measurements performed in non-ideal test sites;
- to develop signal processing algorithms and codes to minimize the impacts of IEMI over railway communication networks;
- to create mechanisms that facilitate the use of such tools by EMC professionals.

1.4 Methodology

Before starting the development of these tools, we worked on a simpler methodology that allowed us to get preliminary results. These results not only represented the first achievement of this research, but were also useful for the further benchmark analyses involving the proposed signal processing tools.

The developed signal processing codes were written in the MATLAB language. These codes are based on existing techniques, such as adaptive filtering, time gating and data reuse. Nevertheless, we observed during our investigations that if we use these structures as described in most papers we do not get the best results for our problems. So, one of the major contributions of this research consists of a new set of filter arrangements and parameters for EMC applications.

The developed tools work *offline*, which means that they are designed for post-processing. In other words, we first collect measurement data and then they are processed. This is not a constraint on the antenna calibration problem, since it does not require real-time filtering. However, we expect that our work can be the first step for future *online* filtering solutions for the IEMI problem.

To validate all the proposed techniques, we ran the tests in both ideal and non-ideal conditions. In the antenna calibration problem, these two test environments are anechoic and non-anechoic rooms. In the IEMI problem, on the other hand, these conditions are equivalent to a railway communication link with and without the presence of jammers. The general framework is based on comparing the measurements performed in ideal conditions with those obtained in non-ideal conditions after being treated by one of the proposed mitigation techniques. The more correlated these two quantities are, the more efficient the mitigation technique is. To take this framework into account, we defined specific metrics for each application. So, when approaching the antenna calibration problem we compare gain *versus* frequency curves using the Pearson correlation coefficient. And when we are dealing with the IEMI problem, we compare the BER levels of a GSM-R system under a jamming attack with and without the proposed filtering structure.

Finally, we highlight that part of this work was carried out at the *Institut Français des Sciences et Technologies des Transports, de l'Aménagement et des Réseaux* (IFSTTAR) (currently *Université Gustave Eiffel*), in Villeneuve d'Ascq, France. More specifically, the author developed part of his research at the *Laboratoire Électronique Ondes et Signaux pour les Transports* (LEOST), during the period from 2019 August to 2020 February, under the supervision of Dr. Virginie Deniau. This was possible thanks to a scholarship from the Brazilian agency CAPES.

1.5 Publications and codes

As a result of this research, 3 techniques have been developed. Throughout this dissertation, they are referred to as: DAE-1, ASP-1 and ASP-2. They have been published in the following papers:

Technique: DAE-1
A. N. de São José, M. V. A. Contreras, R. Adriano, Ú. d. C. Resende and J. F. Mologni, "Uncertainties minimization in open environment antenna gain estimations," 2017 IEEE 3rd Global Electromagnetic Compatibility Conference (GEMCCON), Sao Paulo, 2017, pp. 1-5, doi: 10.1109/GEMCCON.2017.8400666.

Technique: ASP-1
Artur N. de São José, Virginie Deniau, Úrsula do C. Resende, Ricardo Adriano, Improving antenna gain estimations in non-ideal test sites with auto-tunable filters, Measurement, Volume 159, 2020, 107720, doi: 10.1016/j.measurement.2020.107720.

Technique: ASP-2
A. N. d. S. José, V. Deniau, Ú. d. C. Resende and R. Adriano, "Mitigating Intentional Electromagnetic Interferences over the GSM-R System with Adaptive Filters," 2019 23rd International Conference on Applied Electromagnetics and Communications (ICECOM), Dubrovnik, Croatia, 2019, pp. 1-6, doi: 10.1109/ICECOM48045.2019.9163653.

It is worthwhile to mention that some preliminary results concerning the ASP-2 technique were presented in a poster session at the URSI Benelux Forum, in Belgium[2]. Besides, a few conference publications regarding my Masters research and a journal paper containing improvements on it were also published during this Ph.D[3].

All the codes, measurement data and other files related to this dissertation can be found at: <https://github.com/ansj1988>. This is an open-source repository and therefore all the results presented here can be checked any time by anyone. By doing so, we aim to produce reproducible research.

1.6 Dissertation organization

This dissertation is organized as follows. In Chapter 2, we provide an overview of two interference problems: antenna calibration in non-ideal test sites and railway communications under jamming attacks. This chapter also includes some basic EMC principles. In Chapter 3, we continue with the problems description but now with specific details of the test facilities, equipment and software used during our experiments and simulations. Besides, we also detail the main characteristics of the signals behind the antenna calibration and IEMI problems, preliminary experiments and pre-conditioning strategies. In Chapter 4, we describe some candidate mitigation techniques to minimize interference in our problems as well as their limitations. Based on these limitations, we describe, in Chapter 5, three new interference mitigation techniques: DAE-1, ASP-1 and ASP-2. They are described according to their respective applications: DAE-1 and ASP-1 are used in the antenna calibration problem, while ASP-2 is applied to the IEMI issue. Then, we present the experimental and computational results in Chapter 6. Finally, we summarize the main findings and contributions of this research in Chapter 7. In this chapter, we also detail a few other problems that emerge from this research, which can serve as guidelines for future works. Additionally, Appendices A and B are included in this dissertation. In these appendices, one can find basic concepts on two pieces of equipment

---

[2] A. N. de São José, V. Deniau, Úrsula do C. Resende and Ricardo Adriano, "Performance of offline adaptive filters applied to railway security," URSI Benelux Forum, Brussels, 2019. Available at: <http://www.ursi.org/proceedings/MC-Belgium/Forum2019/poster16.pdf>.

[3] A. Nogueira de São José, R. Adriano, Ú. d. C. Resende, M. A. d. Menezes, R. Mary de Souza Batalha and J. Fujioka Mologni, Evaluation of radiated immunity tests using adjusted pulse modulated signals, IET Science, Measurement & Technology, Volume 13, 2019, p.1231-1238, doi: 10.1049/iet-smt.2018.5199.

used in this research: the vector network analyzer and the software-defined radio. Therefore, they serve as a support for those who are not familiar with the EMC field.

Chapter 2

Problem statement

In this chapter, we first present some EMC basic principles, whose core is the notion of interfering sources. With these concepts, it is possible to create mathematical models for the two case studies considered here. Then, we contextualize the antenna calibration and IEMI problems so the reader can better comprehend their origins. We also present some state-of-the-art mitigation techniques for RF measurements in non-ideal open areas and for jamming attacks as well.

2.1 Principles of electromagnetic compatibility

EMC is an Electrical Engineering branch concerned about the undesirable interactions between electrical devices. Even if not designed to do so, an electrical equipment can radiate EM energy or even propagate it through power supply or communication cables. This undesirable energy can reach other devices and, as a consequence, it can cause malfunction or even make them stop working. The reason for that resides in the inseparable relationship between the electrical and electromagnetic phenomena, which can be fully described by Maxwell's equations of Electromagnetism (2).

In order to avoid EMI problems and ensure the correct operation of electrical systems, manufacturers are required to run a set of standardized EMC tests on their products. These tests aim to verify both the emissions and susceptibility levels of a device, by measuring them and comparing them to reference tolerable values. This type of test is described by several standards from organizations such as the International Organization for Standardization (ISO) and the *Comité International Spécial des Perturbations Radioélectriques* (CISPR). In some situations, the EMC conformity of a product can be required by governments in order to authorize its commercialization in a given country (34; 2). In this work, we explore situations in which the EMC standards are not applicable or are not sufficient to avoid EMI problems.

Besides the equipment required to run standardized procedures, other tools can also be found in a typical EMC lab. These can serve many purposes, *e.g. in situ* measurements for quick diagnostics. In this work, the two main pieces of equipment used during the experiments are a vector network analyzer (VNA) and a software-defined radio (SDR). The VNA is used here to investigate an antenna calibration problem, while the SDR is employed in a case study involving IEMI. Details about these pieces of equipment can be found on Appendixes A and B, respectively.

2.2 Mathematical description

There is a wide variety of EMC problems. They can differ in many aspects, *e.g.* aggressor and victim systems hardware, EMI propagation mechanism (radiated or conducted), EMI frequency range and power levels, to name just a few. In this section, we define a generic mathematical model which can describe a wide range of EMC problems. This model is used to state, in a closed analytical form, the general problem under investigation in this dissertation.

Evidently, the mathematical model developed here is just an approximation for actual physical phenomena. In this sense, one of the constraints of our model is the finite number of multipath, EMI and random noise sources. Although these quantities may be large or even infinite in practical measurements, we truncate them in order to allow further computational implementations.

The main issue we deal with in this work refers to the addition of undesirable contributions to a useful signal. The resulting sum represents the signal captured by a measurement instrument. In such cases, each component of the measured signal comes from a specific source. Nevertheless, one cannot usually make a distinction between these individual contributions, once they are all combined into a single measurement. The resulting signal can be represented with the following mathematical model

$$M[n] = s[n] + \sum_{i=1}^{N_1} \alpha_i s[n+\theta_i] + \sum_{i=1}^{N_2} \eta_i[n] + \sum_{i=1}^{N_3} \epsilon_i[n] \tag{2.1}$$

where n is the discrete-time index, $M[n]$ is the measurement, $s[n]$ is the useful signal and $\alpha_i s[n+\theta_i]$ is its i^{th} multipath version with α_i and θ_i being the corresponding attenuation and time delay, respectively; $\eta_i[n]$ and $\epsilon_i[n]$ represent the i^{th} EMI and random noise contributions; finally, N_1, N_2 and N_3 represent the total amount of multipaths, EMI and random noise contributions, respectively. Evidently, the random noise is a type of EMI. In this work, however, the term EMI stands for the undesirable contributions which follow a known pattern, while the random noise refers to signals whose behavior cannot be predicted (*uncorrelated signals*, in a signal processing vocabulary).

According to Eq. 2.1, a useful signal measurement can be compromised by multipath, EMI and random noise. These three spurious contributions are present in the antenna calibration problem, as it will be further detailed in Section 2.3. However, we consider that the multipath and random noise effects are negligible when dealing with the IEMI problem, to be detailed in Section 2.4. This assumption is based on the following observations. First, the jammer output power is usually high when compared to that of the random noise. Therefore, the jamming effects, represented in Eq. 2.1 by the term $\sum_{i=1}^{N_2} \eta_i$, prevail over the random events, $\sum_{i=1}^{N_3} \epsilon_i$, whose impact was mainly noticed in low-power transmissions during our investigations. Second, we assume that the number of EM scatterers, N_1, present in the open space between the base-station and the moving train can be small in non-urban areas (more details about the GSM-R network topology will be given in Section 2.4.2). Given the long extension of the European railway network, these areas represent the channel conditions most of the time. Besides, the distances between the base-stations and the train are usually long. Therefore, even if there is an EM scatterer in between, the resulting multipath components will face a severe attenuation. So, we consider $\alpha_i << 1, \forall i$ in Eq. 2.1.

Based on Eq. 2.1, we develop two mathematical formulations to better describe how the techniques proposed here can improve the quality of the measurements. One of them describes our first approach, called DAE-1, which is based on principles of design and analysis of experiments. The second mathematical formulation refers to the signal processing techniques developed here, called ASP-1 and ASP-2.

The DAE-1 technique is based on the premises that (i) the classical mean estimator, $\overline{\Theta} = (1/N)\sum_{n=1}^{N} \Theta_n$, is unbiased and consistent and (ii) most spurious signal components present spatial and/or time symmetry. These concepts will be discussed in Sections 4.1 and 5.1.1. For the moment, it is sufficient to say that the referred technique is based on averages. Therefore, we expect that, with a certain number of experimental runs (N), the average resulting signal given by

$$\overline{M}[n] = s[n] + \sum_{i=1}^{N_1} \alpha_i \overline{s}[n+\theta_i] + \sum_{i=1}^{N_2} \overline{\eta_i}[n] + \sum_{i=1}^{N_3} \overline{\epsilon_i}[n] \tag{2.2}$$

can be a good $s[n]$ estimate. Equation 2.2 is obtained by applying the sample average estimator, expressed by a horizontal bar, to Eq. 2.1. In this case, we consider that the average operator does not change the useful signal, *i.e.* $\overline{s}[n] = s[n]$.

The premise that $\overline{M}[n] \to s[n]$ only holds true if the test methodology ensures that the residuals, defined here as $\text{RES}_{MP}^{(A)}[n] = \sum_{i=1}^{N_1} \alpha_i \overline{s}[n+\theta_i]$, $\text{RES}_{EMI}^{(A)}[n] = \sum_{i=1}^{N_2} \overline{\eta_i}[n]$ and $\text{RES}_{RN}^{(A)}[n] = \sum_{i=1}^{N_3} \overline{\epsilon_i}[n]$ (referring to multipath, EMI and random noise, respectively), vanish with an increasing N or with a significant number of time samples[1]. In an ideal scenario, $N \to \infty$ and $n \to \infty$. However, considering practical test conditions, we truncate these variables and assume small residues. It means that the expression

$$\overline{M}[n] = s[n] + \mathrm{RES}^{(A)}_{MP}[n] + \mathrm{RES}^{(A)}_{EMI}[n] + \mathrm{RES}^{(A)}_{RN}[n] \tag{2.3}$$

results in a useful signal estimate, as follows

$$\widehat{s}[n] = \overline{M}[n]. \tag{2.4}$$

On the other hand, the signal processing approaches proposed here are based on multipath, EMI and random noise estimates. If subtracted from Eq. 2.1, these estimates give rise to an *error signal*, defined by

$$e[n] \equiv M[n] - Q[n] \tag{2.5}$$

where $Q[n]$ is the sum of all the spurious signals estimates, *i.e.*

$$Q[n] = \sum_{i=1}^{N_1} \widehat{\alpha}_i \widehat{s}[n + \widehat{\theta}_i] + \sum_{i=1}^{N_2} \widehat{\eta}_i[n] + \sum_{i=1}^{N_3} \widehat{\epsilon}_i[n] \tag{2.6}$$

where $\sum_{i=1}^{N_1} \widehat{\alpha}_i \widehat{s}[n + \widehat{\theta}_i]$, $\sum_{i=1}^{N_2} \widehat{\eta}_i[n]$ and $\sum_{i=1}^{N_3} \widehat{\epsilon}_i[n]$ are multipath, EMI and random noise estimates, respectively. So, if we substitute Eqs. 2.1 and 2.6 in Eq. 2.5, we obtain

$$\begin{aligned} e[n] = {} & \left(s[n] + \sum_{i=1}^{N_1} \alpha_i s[n + \theta_i] + \sum_{i=1}^{N_2} \eta_i[n] + \sum_{i=1}^{N_3} \epsilon_i[n] \right) - \left(\sum_{i=1}^{N_1} \widehat{\alpha}_i \widehat{s}[n + \widehat{\theta}_i] \right. \\ & \left. + \sum_{i=1}^{N_2} \widehat{\eta}_i[n] + \sum_{i=1}^{N_3} \widehat{\epsilon}_i[n] \right). \end{aligned} \tag{2.7}$$

We can re-write this expression by grouping the signal components with their respective estimates, resulting in:

$$\begin{aligned} e[n] = s[n] & + \left(\sum_{i=1}^{N_1} \alpha_i s[n + \theta_i] - \sum_{i=1}^{N_1} \widehat{\alpha}_i \widehat{s}[n + \widehat{\theta}_i] \right) + \left(\sum_{i=1}^{N_2} \eta_i[n] - \sum_{i=1}^{N_2} \widehat{\eta}_i[n] \right) \\ & + \left(\sum_{i=1}^{N_3} \epsilon_i[n] - \sum_{i=1}^{N_3} \widehat{\epsilon}_i[n] \right) \end{aligned} \tag{2.8}$$

---

[1] The superscript (A) is used here to make a distinction from the other residual terms that appear in this section.

which is equivalent to:

$$e[n] = s[n] + \mathrm{RES}_{MP}^{(B)}[n] + \mathrm{RES}_{EMI}^{(B)}[n] + \mathrm{RES}_{RN}^{(B)}[n] \tag{2.9}$$

where $\mathrm{RES}_{MP}^{(B)}[n]$, $\mathrm{RES}_{EMI}^{(B)}[n]$ and $\mathrm{RES}_{RN}^{(B)}[n]$ are the multipath, EMI and random noise estimates residuals, respectively. Observe that their evaluation is no longer based on averages. Instead, we define $\mathrm{RES}_{MP}^{(B)}[n] = \sum_{i=1}^{N_1} \alpha_i s[n+\theta_i] - \sum_{i=1}^{N_1} \widehat{\alpha}_i \widehat{s}[n+\widehat{\theta}_i]$, $\mathrm{RES}_{EMI}^{(B)}[n] = \sum_{i=1}^{N_2} \eta_i[n] - \sum_{i=1}^{N_2} \widehat{\eta}_i[n]$ and $\mathrm{RES}_{RN}^{(B)}[n] = \sum_{i=1}^{N_3} \epsilon_i[n] - \sum_{i=1}^{N_3} \widehat{\epsilon}_i[n]$.

From the above equations, it is evident that the better the spurious signals estimates are, the closer the error and useful signals become. If a finite set of candidate estimates is available, *i.e.* $\widehat{\alpha}_{i,k}\widehat{s}_k[n+\widehat{\theta}_{i,k}]$, $\widehat{\epsilon}_{i,k}[n]$ and $\widehat{\eta}_{i,k}[n]$ (where $k = 1, 2, ..., K$ and K is the number of available estimates), then the main task is to find those that minimize the residual terms in Eq. 2.9. More specifically, in the signal processing literature, it is common to find techniques which are based on the mean squared error (MSE) minimization.

Unfortunately, the MSE is of difficult calculation in practice. It is defined as $\mathbb{E}\{e^2[n]\}$ where $\mathbb{E}\{.\}$ is the expectation operator. In other words, it is the true mean of the random variable $e^2[n]$. As it will be further discussed in Section 4.1, this calculation is unpractical because of the required amount of observations of the random variable. Most of the times, the expectation is truncated with a finite number of realizations, N. Thus, if we truncate the mean quadratic version of Eq. 2.9 and then minimize the resulting expression, we have

$$\widehat{s}[n] = \min \overline{(s[n] + \mathrm{RES}_{MP}^{(B)}[n] + \mathrm{RES}_{EMI}^{(B)}[n] + \mathrm{RES}_{RN}^{(B)}[n])^2}. \tag{2.10}$$

Still, this MSE-based calculation remains difficult even with the truncation. Real-time systems, for instance, need instantaneous useful signal estimates in order to operate properly. Fortunately, there are signal processing techniques that allows us to evaluate Eq. 2.10 with a single experimental run. In this work, we use the normalized least mean squares (NLMS) method. The mathematical formulation of this class of algorithms is in turn based on the truncation of the MSE by its instantaneous values – see, for instance, Section 10.2 in (35) or 3.2 in (36). Therefore, we can define the following formulation to describe the ASP-1 and ASP-2 techniques

$$\widehat{s}[n] = \min(s[n] + \mathrm{RES}_{MP}^{(B)}[n] + \mathrm{RES}_{EMI}^{(B)}[n] + \mathrm{RES}_{RN}^{(B)}[n])^2. \tag{2.11}$$

2.3 Antenna calibration in non-ideal test sites

2.3.1 General aspects

Antennas are widespread devices and therefore they are constantly present in our daily lives by means of technologies like cell phones, televisions etc. They are also used to generate or receive EMI over wide frequency ranges in EMC tests. Evidently, their parameters may change from one application to another. Some antenna properties are bandwidth, voltage standing wave ratio (VSWR), gain and directivity, the last two being similar but not identical. In this work, we focus on gain estimation.

Gain and directivity are spatial variables, meaning that they describe the antenna radiation strength at a given direction. They are essentially power ratios, as described by the following equations (37):

$$G(\theta, \phi) = 4\pi \frac{U(\theta, \phi)}{P_{in}} \tag{2.12}$$

$$D(\theta, \phi) = 4\pi \frac{U(\theta, \phi)}{P_{rad}}. \tag{2.13}$$

In the above equations, (θ, ϕ) is a pair of spherical coordinates forming a solid angle, *i.e.* the direction; $G(\theta, \phi)$, $D(\theta, \phi)$ and $U(\theta, \phi)$ are the gain, directivity and radiation intensity through this angle, respectively; P_{in} and P_{rad} are the input and total radiated powers, respectively. The slight difference between Eqs. 2.12 and 2.13 means that the directivity calculation does not take into account the losses introduced by the antenna itself. When nothing is said about the direction, it is usual to consider the solid angle related to the peak gain. In this work, we consider the peak gain and its frequency dependency.

In order to check if an antenna prototype or even its final version follows the gain design specifications, manufacturers are required to test it. Such a procedure is also known as antenna calibration. Standardized antenna calibration procedures can be found in IEEE 149 (38), IEEE C63.5-2017 (3) or other similar documents. Test setups usually include the antenna under test (AUT) and other auxiliary antennas. Furthermore, these standards impose certain requirements regarding the test site conditions. Anechoic chambers and OATS are typical test environments. Anechoic chambers are shielded rooms with EM absorbers in its internal surfaces (when the absorbers are not present in the floor, it is said that the chamber is *semi-anechoic*). On the other hand, OATS are open spaces which are sufficiently free from EMI sources and reflecting surfaces. Nevertheless, anechoic chambers are expensive solutions and OATS measurements can require large areas in non-urban locations. Therefore, these conditions can represent constraints. In this work, we explore ways of improving the test conditions of non-ideal OATS environments.

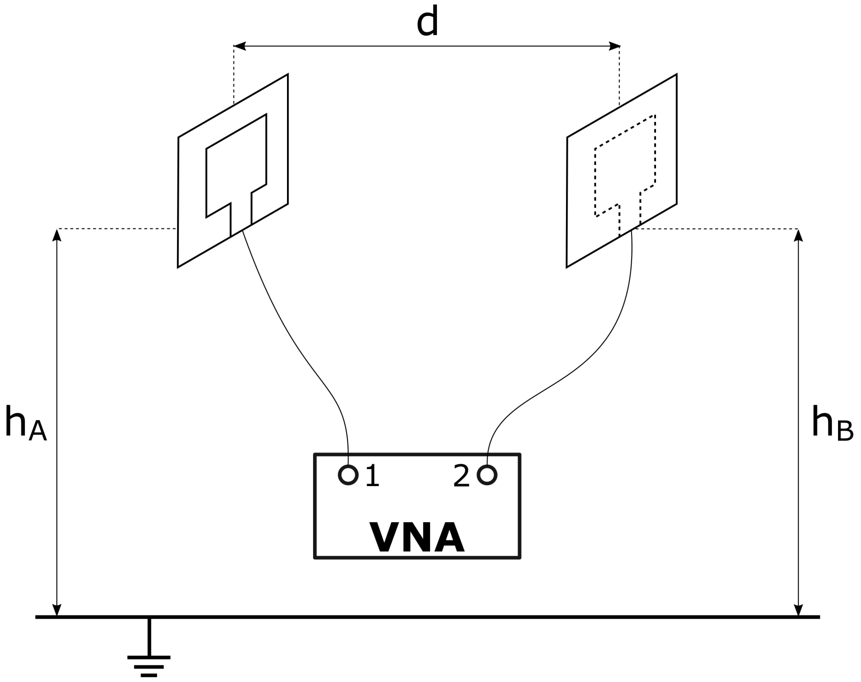

Figure 2.1 – Generic antenna calibration setup, containing an antenna under test and an auxiliary antenna, h_A and h_B meters above the metallic floor, respectively. The distance between them, d, must be sufficient to ensure the far-field condition. The VNA estimates the S_{12} parameter, which is used for the gain calculation.

2.3.2 Test setup

Figure 2.1 illustrates the basic equipment which are commonly used for antenna calibration. In this generic representation, two antennas are present. The first one is the AUT. It is located h_A meters above the floor, while an auxiliary antenna is placed at a h_B meters height. Some test procedures may require a varying h_B, but in our investigation we consider $h_A = h_B$. According to the IEEE 149 standard (38), the separation distance between them, d, must be sufficient to ensure the far-field condition.

Another important aspect of the test setup in Fig. 2.1 is the floor. In this figure, we illustrate a metallic reference floor – this is a standard requirement for test frequencies up to 1 GHz. Since the AUTs adopted for this investigation operate in higher frequencies, we do not use this type of floor during the reference (chamber) measurements. Instead, we use RF absorbing materials in the floor. However, when measuring in non-ideal conditions, reflections coming from the floor can occur.

As a last remark on this generic test setup, we highlight the presence of a VNA. This 2-port device contains an internal source that excites the antenna attached to the Port 2. At the same time, it monitors the power received in Port 1. Knowing the transmitted and received powers, the device calculates the S_{12} parameter along the AUT operating frequency range (for more details, please refer to the Appendix A). This information is necessary for the gain estimation. The other parameters provided by the VNA (S_{11}, S_{22} and S_{21}) are not used in this investigation.

In order to define the particular aspects of a given AUT calibration setup, one may consider its operating frequency range and if a reference antenna is available. The first item is crucial to define whether a metallic ground plane is necessary or not. The IEEE 149 standard (38) defines the frequency range above 1 GHz as the *free-space antenna range*, in which experiments without ground planes can be performed. It also defines the range between 0.1 and 1 GHz as the *ground-reflection range*. In fact, practical antennas operating in this range are usually attached to a device through a metallic plane[2]. In this work, we deal with frequencies sufficiently higher than 1 GHz, so the adopted method is the free-space antenna range. The second item refers to the availability of a reference antenna, *i.e.* an antenna whose gain is previously known. Regarding this point, IEEE 149 defines the *absolute-gain* and the *gain-transfer measurements*. The first method does not demand any knowledge about the auxiliary antenna properties, while the second one does. In gain-transfer measurements, the AUT gain is compared to a calibrated antenna gain. For this investigation, we consider absolute-gain measurements. The reason for that is: small labs rarely have a reference antenna and even when they acquire one of these from a professional supplier, it is not periodically calibrated on a certified lab.

2.3.3 Gain estimates obtained from the S_{12} measurements

At this point, we define a notation that will help the comprehension of the proposed methodologies. In this work, the term S_{12} *parameter* is a qualitative reference to the strength of the aerial link between two antennas. Therefore, there is no specific numerical value associated to it (unless we explicitly mention a quantity, *e.g.* the measurements reveal that the S_{12} parameter magnitude is -5 dB in 2.4 GHz). On the other hand, when we refer to a given S_{12} *signal*, we mean a set of values (*i.e.* a vector, in computational terms) that describe this variable along the time or frequency. If the domain is time, then the S_{12} signal is real. Otherwise, it is a complex quantity.

The gain calculation can be obtained from the S_{12} parameter through the Friis equation, valid in the far-field region

$$G_{AUT}(dB) = 10\log(4\pi d/\lambda) + S_{12}(dB)/2. \tag{2.14}$$

In this equation, adapted from (38), $G_{AUT}(dB)$ is the unknown AUT gain, λ is the wavelength and $S_{12}(dB) = 10\log P_r/P_t$, with P_r and P_t being the received and transmitted powers, respectively. To obtain this expression, we consider that the AUT and the auxiliary

---

[2] In general, the antenna dimensions are proportional to the wavelength. Therefore, for lower frequencies the required dimensions can be impracticable. Solutions usually rely on the Image Theory-based use of a ground plane.

antenna have the same gain. One interesting implication of this assumption is that no matter whether the AUT is the transmitting or the receiving unit. When this assumption is not reasonable, one shall adopt the *three-antenna method* (38).

2.4 Intentional electromagnetic interference in railway systems

Modern railway systems, or simply HSRs, provide efficient and safe transportation to a large number of people nowadays. Moreover, customers are provided with multimedia services and access to WiFi networks (33; 27). All these advantages are possible thanks to interconnected railway networks that use a common communication standard that ensure proper train operation. Such a communication system allows voice calls involving the railway staff (both on-board and off the train). It also allows data exchange between sensors and control systems. To illustrate the geographical extension of these interconnected railway networks, we show in Fig. 2.2 a map containing some train routes offered by a French company.

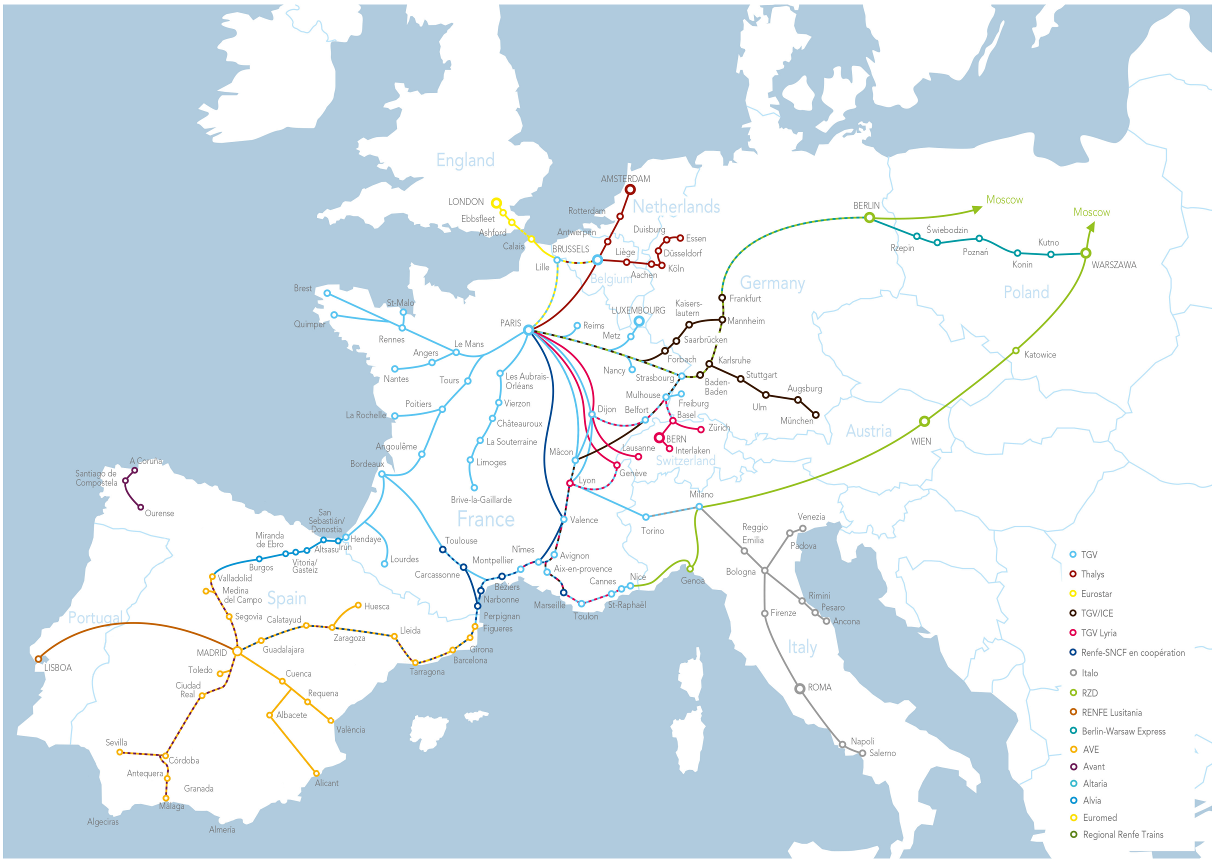

Figure 2.2 – European railway system's geographical extension, exemplified with the train routes offered by a French company (39).

In the next sub-sections, we describe the most common standard adopted nowadays by the railway market: the GSM-R. We also provide an overview of the most common types of jamming attacks aiming at disturbing GSM-R networks.

2.4.1 Brief history of the GSM-R standard

The GSM-R standard emerged in a context where most European countries had their own railway systems. For example, there were 14 different security systems throughout Europe in the 1980s. This scenario constituted a barrier for the international transportation of people and products. Some of the many constraints were that the railway personnel usually had to carry more than one radio equipment on board and that drivers were changed when the train was crossing borders (40).

So, in 1993 a group formed by eight companies, the European Union and stakeholders created the European rail traffic management system (ERTMS) (40; 41). The goal was to define common guidelines and standards to be adopted by different European countries. Besides the GSM-R standard, the ERTMS also specifies the Eurobalise system. It consists of certain devices called beacons, which are installed along the track. When the train is nearby a beacon, a short-range communication is established and positioning data is updated – this can be used *e.g.* to calibrate the odometer (4; 29).

In the following years, other initiatives were taken to make the standardization possible. In 1996, the Directive 96/48/EC was launched in order to define the conditions for the HSR systems' interoperability. From 1992 to 1997, an effort was made by an organization called *union internationale des chemins de fer* (UIC) to define the technical specifications of the new railway communication system. This project, which became known as the European integrated radio enhanced network (EIRENE), finally resulted in the GSM-R standard, whose first implementations occurred in the beginning of the 2000s (41; 40).

As we can see, the deployment of GSM-R took a long time – almost one decade from idealization to implementation. During this period, mobile communications have evolved quickly. As a consequence, there is nowadays an increasing discrepancy between the GSM-R standard – which is based on the global system for mobile communications (GSM), a second-generation mobile communications standard – and the current wireless technologies. So, UIC now conducts the future railway mobile communication system (FRMCS) project, aiming at defining the substitute for the GSM-R technology. The new technology, which will progressively replace GSM-R, is called the long-term evolution-railway (LTE-R) (33).

2.4.2 Technical aspects

The GSM-R standard derives from GSM, a second-generation mobile telephony technology which emerged in the beginning of the 1990s. So, many characteristics of the

GSM system were extended to GSM-R. Nevertheless, GSM-R has some exclusive features oriented to the railway environment, most of them being related to voice communication.

Some of the exclusive features of the GSM-R standard are the *functional addressing* and the *location-dependent addressing*. With these schemes, identification numbers are attributed to the train driver's or operator's terminals/handsets. These numbers are not conventional phone numbers but addresses that facilitate the communication between train drivers and operators, including group calls. Furthermore, priority is given to emergency calls – other calls can be interrupted if necessary (33; 40).

In terms of infra-structure, a GSM-R network involves many equipment – in (42), one can find a detailed description of the GSM architecture. However, our analyses are restricted to the radio sub-system, responsible for the physical layer communication. This sub-system is composed of the mobile (train) and base stations as well as the base station controller (42). Figure 2.3 illustrates the bi-directional communication between the base and mobile stations under jamming attack.

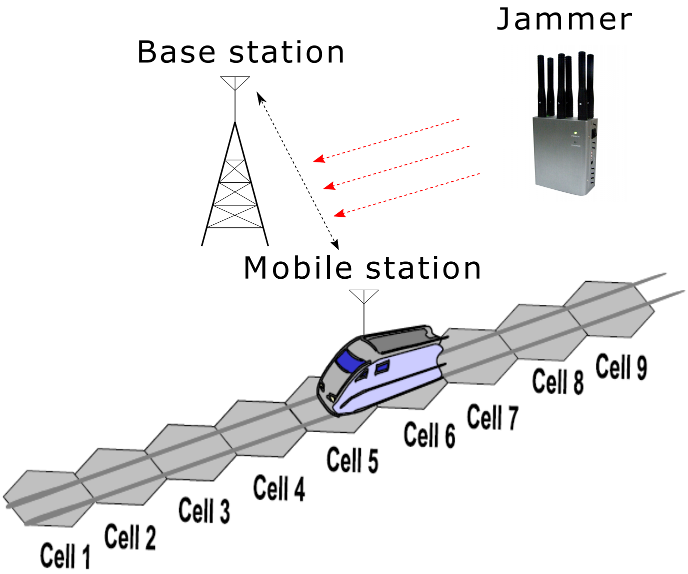

Figure 2.3 – Illustration of the GSM-R uplink and downlink communications (double-headed black arrow) under a jamming attack (red arrow). The train progressively changes from one cell to another along the route. Adapted from (32).

In Fig. 2.3, we highlight with a double-headed black arrow both the downlink (DL) and uplink (UL) signals exchanged between the base and mobile stations. The UL (train → base-station) channel occupies the $876 - 915$ MHz range, while the DL (base-station → train) band is $921 - 960$ MHz (4). We also highlight the division of the train route in terms of cells – a concept which was adapted from the conventional GSM systems. On the other hand, the unidirectional red arrows represent undesirable jamming signals directed towards the GSM-R transmitters and/or receivers.

Among the advantages introduced by the GSM technology over the previous ones, one can highlight the introduction of digital modulation and time division multiple access (TDMA). By combining TDMA with frequency division multiple access (FDMA), the base station started to allocate more users within a given cell (42).

Multiple users can share these bands via TDMA. Gaussian minimum shift keying (GMSK) data is then transmitted in groups of $577\mu s$ time slots. A complete frame comprises 8 time slots (4). In this work, we analyse the effects of IEMI over a DL time slot. Throughout this work, we refer to this signal as a GSM-R *burst*. Based on the exposed, Table 2.1 summarizes the main characteristics of GSM-R networks.

Table 2.1 – Main characteristics of GSM-R networks. Adapted from (33).

Parameter	Value
Uplink frequency band	876–915 MHz;
Downlink frequency band	921–925 MHz
Bandwidth	200 kHz
Modulation	GMSK
Cell range	8 km
Peak data rate (UL/DL)	172/172 kbps
Mobility	Max. 500 km/h

2.4.3 Jamming attacks

Jamming attacks consists in emitting EM fields aiming at disturbing a certain communication system or even damaging equipment. In (43), the authors propose certain attributes that allow one to classify these attacks. Some of these attributes are: the incident field waveform, the technology behind the EM source (level of sophistication) and the potential effects (*e.g.* permanent or momentary loss of function). Figure 2.4 illustrates two simple EM attack strategies, in terms of magnitude spectra: continuous wave (CW) and frequency modulation (FM).

In this work, we deal with FM-based jamming attacks. This type of attack has been used by other researchers in recent publications (32; 44). More details about this signal will be given in the next chapter.

2.5 Final considerations

In this chapter, we defined important mathematical models for the current investigation. The first one, Eq. 2.1, summarizes the main undesirable phenomena that affect the antenna gain estimates and the GSM-R communication. Furthermore, with Eqs. 2.4 and 2.11, we explain how we aim to mitigate these spurious effects.

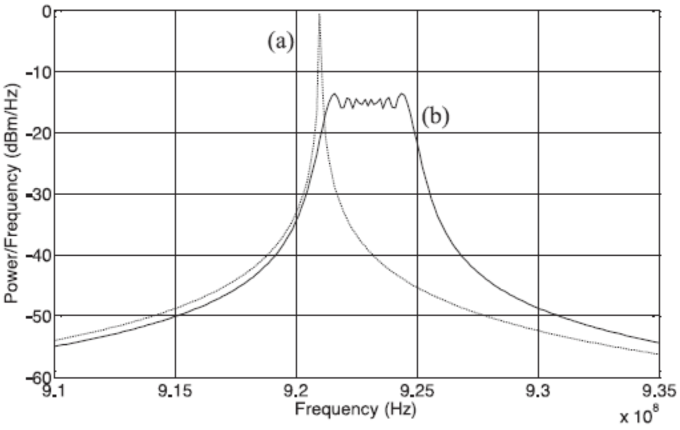

Figure 2.4 – Two examples of EM attack strategies: (a) CW and (b) FM. Extracted from (32).

We also provided up-to-date information concerning the two problems under investigation. Besides the technical details, we presented several state-of-the-art related studies, which reinforce the need for new researches in the antenna calibration and IEMI fields. In particular, the emerging antenna packaging techniques indicate that the development of new calibration techniques is necessary for these 5G (and beyond) integrated devices.

Chapter 3

Signals and test setups

Following the general aspects of the antenna calibration and IEMI problems discussed in the previous chapter, we now show the particularities of the signals and systems under analysis in this work. In this chapter, we detail the equipment arrangement, its configuration and the four test facilities used to collect experimental data for further processing. Furthermore, we show some preliminary experiments that allow us to characterize the main signals behind the problems under analysis.

3.1 Test facilities

In order to evaluate the methodologies proposed to solve the antenna calibration problem, four different facilities were used. Two of them are located at the Federal University of Minas Gerais (UFMG) and the other two are located at the French Institute of Science and Technology for Transport, Development and Networks (IFSTTAR). To facilitate the identification of the test setups according to the host institution and specific facility, we adopt the notations shown in Table 3.1. This table also indicates which test places are adequate to run the tests and which are not.

Table 3.1 – Test facilities used for the experiments.

Notation	Facility	Institution	Test condition
Lab1	Applied Electromagnetics Lab	UFMG	Non-ideal
Lab2	Electromagnetic Compatibility Lab	IFSTTAR	Non-ideal
Cha1	Anechoic Chamber	UFMG	Ideal
Cha2	Anechoic Chamber	IFSTTAR	Ideal

To investigate the IEMI problem, a virtual test setup was created with MATLAB codes. These codes allow us to simulate the GSM-R transmission and reception processes in an ideal lossless channel. Furthermore, we simplify the synthesis of the GSM-R signals by eliminating many stages of an actual transmission. All these simplifications allow us to focus our attention on the filters' performances.

In Appendix B, we detail some lab experiments that were run during this research in an attempt to generate more realistic signals. The resulting measurements could not be considered for our analyses due to some hardware problems. The possible causes are also discussed in this appendix.

3.2 Antenna calibration problem

3.2.1 Equipment arrangement and configuration

The analyses concerning the antenna calibration problem are carried out in both ideal and non-ideal test conditions. By doing so, we get two data sets: (A) measurements taken in non-ideal conditions and (B) measurements taken in ideal conditions. In a first moment, we compare (A) and (B) in an attempt to show that the cross-correlation levels are relatively low. In a second moment, we apply the DAE-1 or the ASP-1 technique (to be described in Chapter 5) to (A) and get another data set, called (C). Now we compare (C) and (B). Our expectation is that the cross-correlation between (C) and (B) is higher than that obtained from the comparison between (A) and (B). A general post-processing framework applied to the signals measured in non-ideal conditions is then proposed.

Table 3.1 contains two ideal (Cha1, Cha2) and two non-ideal (Lab1, Lab2) facilities for antenna calibration. The equipment arrangements established in Lab1 and Lab2 are illustrated in Figs. 3.1a and 3.1b. In these places, one can find a number of objects, each of them with its particular constituent material, shape and size. Therefore, unpredictable multipath contributions can be present on the measurements. This phenomenon can be more intense in omnidirectional antennas, since they are designed to radiate in all directions. Although an interesting feature for some applications, such a radiation pattern can cause multipath signals to add with those coming from the line-of-sight direction. Consequently, the signal power levels read by the receiving antenna can be higher or lower than the actual one, depending on the type of interaction between the signals (*i.e.* totally/partially constructive/destructive). Thus, the estimated gain can differ from the actual one if no multipath control is established.

Furthermore, these labs are equipped with WiFi routers, which operate within the antennas frequency bands. Depending on the distance they are from the test setup, a significant amount of power coming from the internet activity will be noted on the VNA S_{12} *versus* frequency plot. Consequently, this can lead to a misinterpretation of the antenna resonance profile. If the S_{12} peak produced by the WiFi activity coincides in frequency with the actual antenna resonance point, the gain reading can be higher of lower than it should. However, if the spurious peak does not coincide with the actual one but if their powers are comparable, then one could think the antenna has more than one resonance frequency, when it actually has only one.

From the exposed, we conclude that the gain estimates' accuracy can be compromised by the presence of objects and communication devices nearby the test setup. It is also clear that the test setups from Figs. 3.1a and 3.1b offer no alternatives to contour these issues.

On the other hand, Figs. 3.2a and 3.2b illustrate the test setup arrangements in Cha1 and Cha2. These places offer shielding against external influences, ensuring that almost no signal enters the test place. Besides, these chambers offer electromagnetic absorbing conditions in their internal walls. Such condition significantly reduces the multipath effects.

Table 3.2 summarizes the main characteristics of the antennas used in our investigations. The antennas denoted as AUT1, AUT2 and AUT3 are used in the filters' performance evaluation, while AUT4 is only used to explore the signals characteristics, as further described in Section 3.2.2[1]. Besides the main antenna parameters, this table contains bibliographical references with more information about them.

Table 3.2 – Antennas used during this investigation, in terms of notation, type, properties and references for more details.

Notation	Type	Directivity	Range	Reference
AUT1	Patch	Directive	1.5-4.5 GHz	(45)
AUT2	Patch	Omnidirectional	1.5-4.5 GHz	(45)
AUT3	Horn	Directive	700 MHz-18 GHz	(46)
AUT4	Patch	Directive	2-3 GHz	(47)

To give a better understanding about these antennas, we show them in Fig. 3.3. The antennas illustrated in Figs. 3.3a and 3.3b represent AUT1 and AUT2. They were designed by (45) for ground-penetrating radar (GPR) applications. GPR systems are those that try to identify an underground material based on electromagnetic wave reflections. The horn antenna in Figs. 3.3c, AUT3, is designed for two types of EMC testing: radiated immunity and radiated emissions. During the immunity test, one monitors a DUT when exposed to a controlled electric field (which represents an EMI). On the other hand, the spurious RF emissions coming from the DUT are measured in the second test. In both

---

[1] We chose AUT4 to start this investigation but later on we had access to other antennas with better manufacturing quality. Nevertheless, this does not represent a constraint on our investigation because the analyses carried out in Section 3.2.2 are qualitative. Our aim at this point is to analyse the impacts of EMI and multipath over a typical antenna "signature". For such reason, the results obtained here can be extended to other antennas.

(a)

(b)

Figure 3.1 – Antenna calibration test setups in non-ideal OATS. (a) Lab1. (b) Lab2.

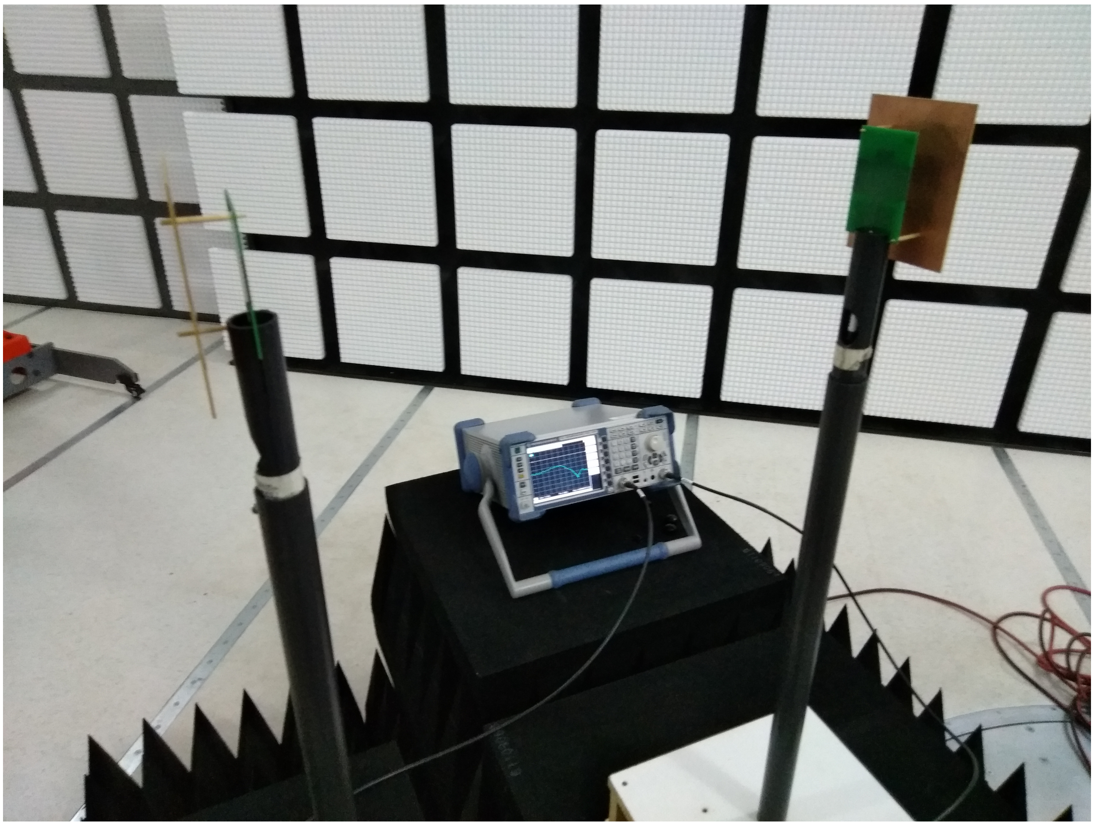

(a)

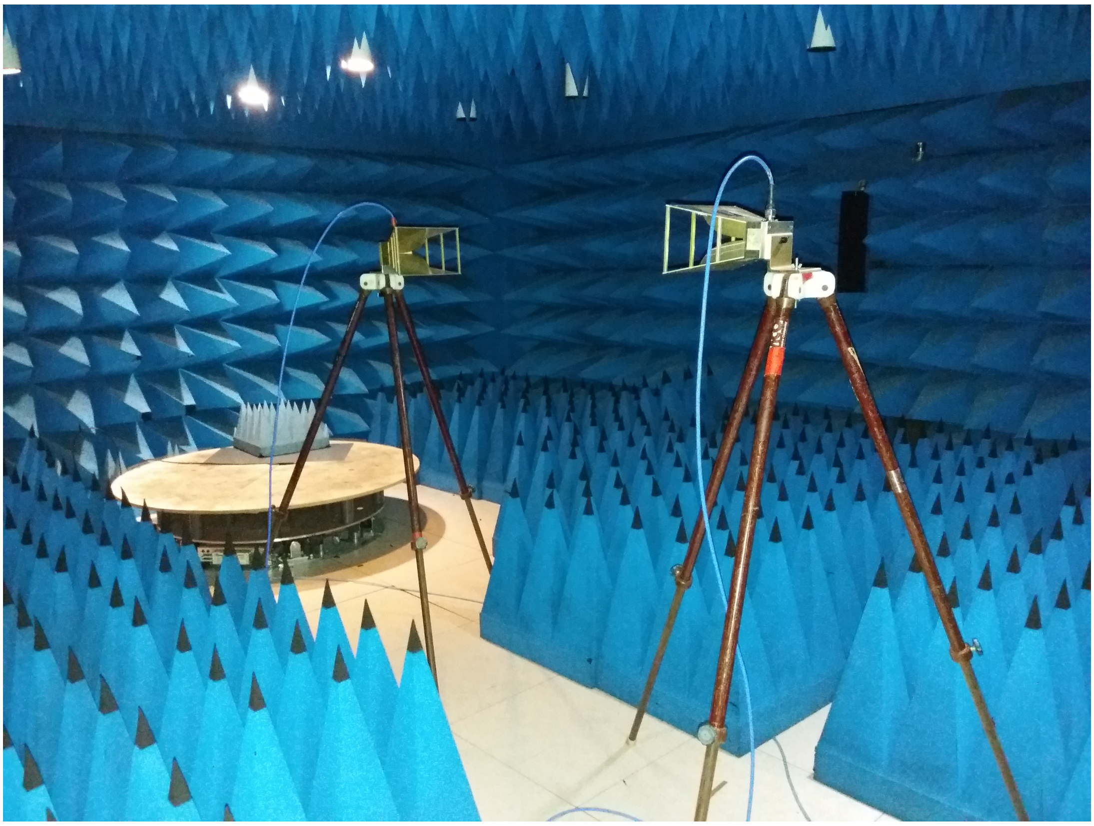

(b)

Figure 3.2 – Antenna calibration test setups in anechoic chambers. (a) Cha1. (b) Cha2.

cases, a broad-band antenna with high gains and low VSWR levels is required. Finally, the antenna illustrated in Fig. 3.3d, AUT4, was designed for energy harvesting applications.

As a last remark, we highlight that the proposed techniques are analysed under different multipath conditions. This is possible thanks to the use of both directive and omnidirectional antennas. To illustrate that, we show in Figs. 3.4, 3.5 and 3.6 the AUT1, AUT2 and AUT3 radiation patterns, respectively. Before proceeding with the analysis, it is important to mention that AUT1 and AUT2 are almost identical: the difference is that AUT1 has a mettalic plane parallel to the printed circuit board while AUT2 has not – compare the pictures in Figs. 3.3a and 3.3b. Now, if we compare 3.4a and 3.5a, we realize how the introduction of this plane affects the antenna directivity. In Fig. 3.4a, we see a directive pattern mostly concentrated around the 0 deg direction – similarly to the AUT3 pattern illustrated in Fig. 3.6. On the other hand, we see in Fig. 3.4a that the absence of the metallic surface allows AUT2 to have both a front and a back lobes. The metallic plane, however, does not affect the radiation in the vertical plane – see Figs. 3.4b and 3.5b. We expect that these different radiation patterns lead to different multipath conditions during the measurement campaigns.

3.2.2 Full characterization of the signals

The first step in the present investigation consists of fully characterizing both the S_{12} signal and the undesirable phenomena which are typically present in non-ideal test environments. We propose a few procedures that aim to isolate the undesirable phenomena, which are usually superimposed in a lab measurement. In the present investigation, these contributions are grouped into three categories: multipath, EMI and thermal noise. Each of them will be explored in the next sub-sections.

At this time, the signal analyses are performed over the time domain (in opposition to the spectral analyses described in Chapter 6). We choose time instead of frequency for convenience, given the purposes of this investigation. One reason is that the multipath effects can be easily identified in the S_{12} waveform by means of secondary peak values. The same type of analysis would be more difficult in frequency because it would not only require a visual inspection of the magnitude spectrum but also of the phase plot. Besides, the proposed signal processing approaches, to be later described, are based on filtering tools that operate primarily in the time domain (although adaptive filters can also operate in the frequency domain – see (35), Chapter 26).

The VNA operates primarily in the frequency domain. So, to operate in the time domain, a transformation is required. This operation can be usually made using the graphical interface of the VNA. Nevertheless, we choose to export the raw data provided by the VNA to a flash drive and then we apply an inverse Fourier transform (IFFT) using a personal computer equipped with MATLAB.

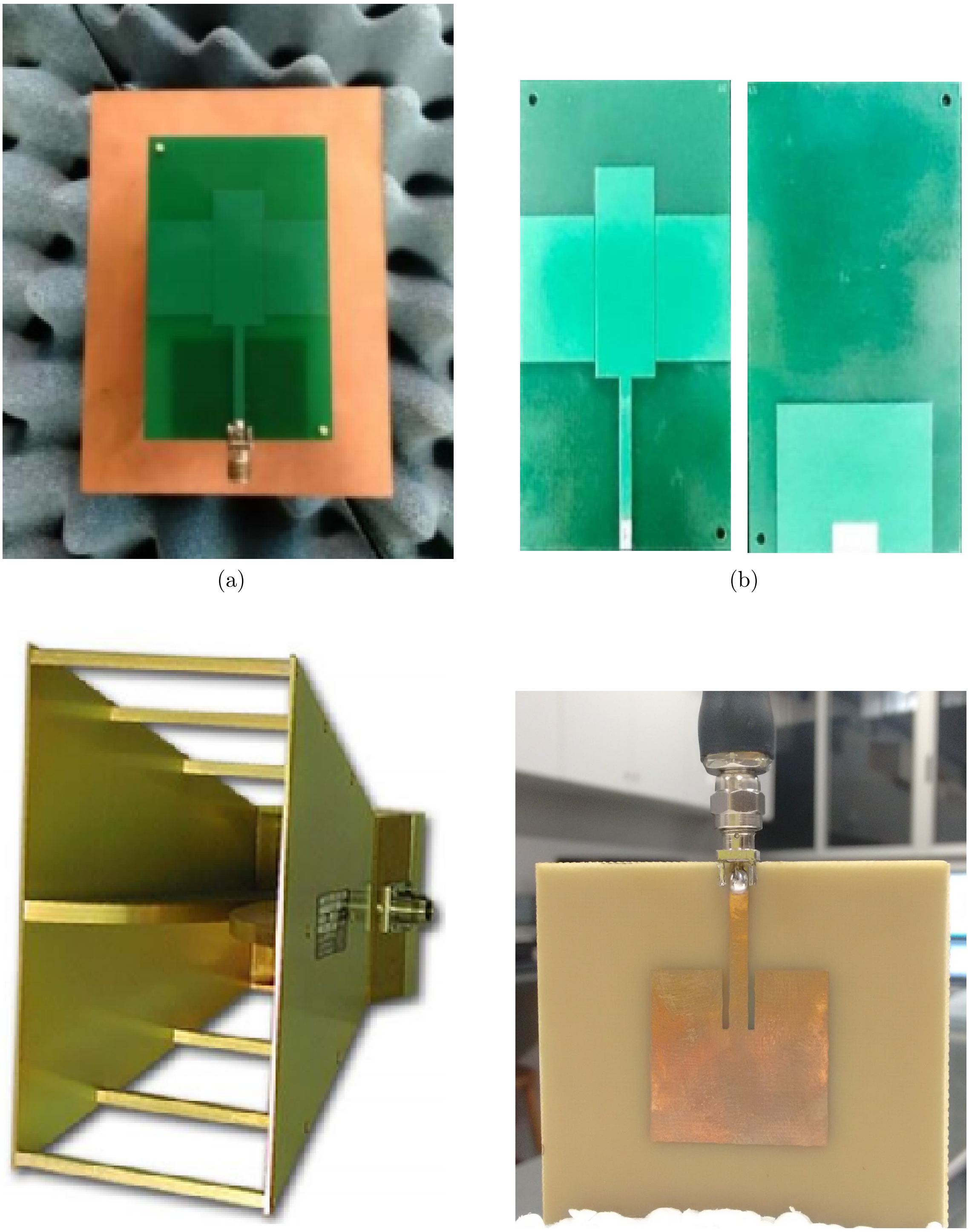

(a) (b)

(c) (d)

Figure 3.3 – Antennas used in this work. (a) AUT1: a directive patch antenna (45). (b) AUT2: an omnidirectional patch antenna (45). It has the same circuit board as AUT1, but it has no reflecting plane. (c) AUT3: a directive horn antenna (46). (d) AUT4: a directive patch antenna (47).

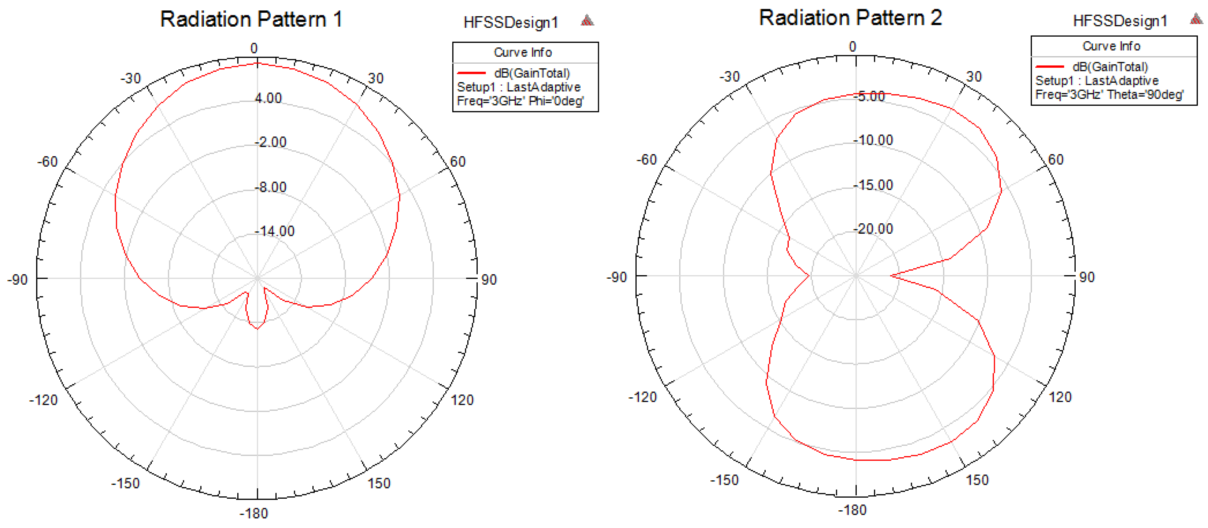

(a) (b)

Figure 3.4 – AUT1 radiation pattern. (a) Horizontal plane. (b) Vertical plane.

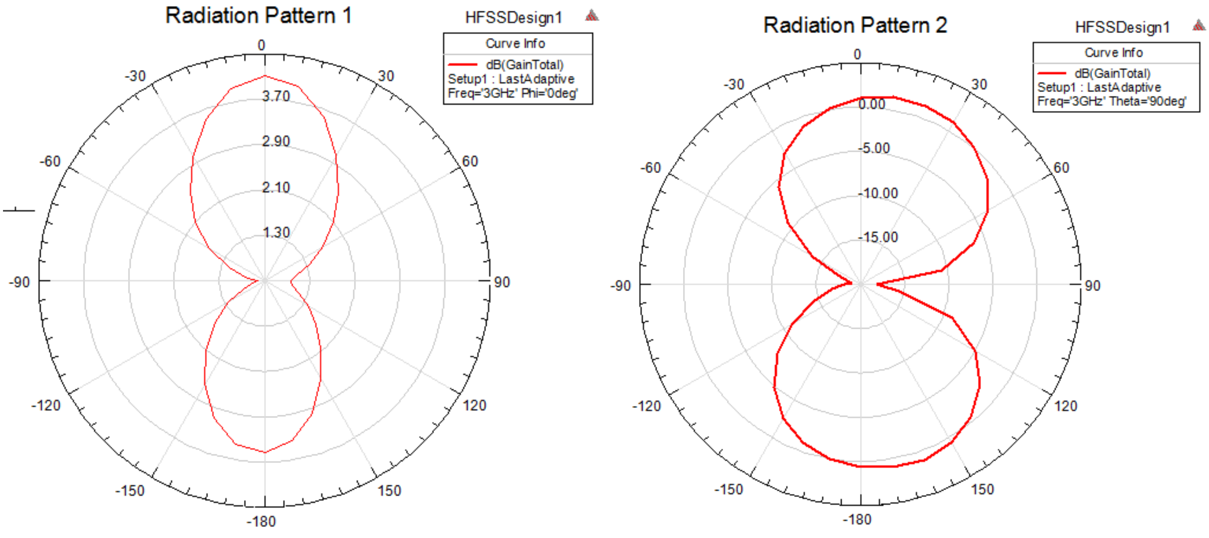

(a) (b)

Figure 3.5 – AUT2 radiation pattern. (a) Horizontal plane. (b) Vertical plane.

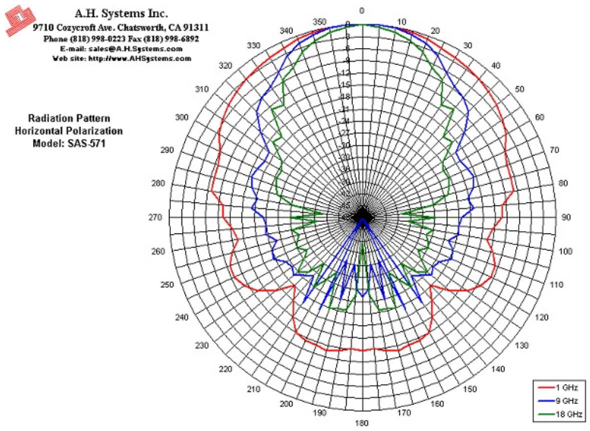

Figure 3.6 – AUT3 radiation pattern (48).

3.2.2.1 S_{12} and multipath

The full characterization of the S_{12} signal is based on the coupling between the VNA ports 1 and 2. This equipment is provided with an internal source, as detailed in Appendix A. This source can supply both ports but not simultaneously. When the VNA calculates the S_{12} parameter, it feeds port 2 while port 1 serves as a 50 Ω termination. In this context, we analyze three types of coupling, to be detailed in the next paragraphs. They allow us to know the original VNA excitation signal and the effects caused on it by the introduction of the antennas as well as the multipath.

However, before any measurement we calibrate the VNA using a procedure known as short-open-load-through (SOLT). This process aims to eliminate the power attenuation, reflections losses due to impedance mismatches and other effects of the instrumentation system from the measurements. It demands the use of a calibration kit, which is usually sold together with the VNA. More details about the VNA calibration procedure can be found in the Appendix A.

The first waveform we aim to obtain is that of the VNA supply signal. Unfortunately, we cannot extract samples of this signal directly from the VNA output terminals. Given this scenario, we propose a special approach. To obtain the excitation signal, a direct connection between the VNA ports 1 and 2 is established. To do so, we use two coaxial cables and, again, the VNA calibration kit. More specifically, we use a pair of terminals from this kit known as *through* (sometimes referred as *thru*). From this point on, we call this connection a *short-circuit*. Although it does not involve overcurrents/overheating and therefore it does not configure a classical short-circuit, we define this notation in order to make a clear distinction from the other connections, to be detailed in the next paragraphs.

The next step of our analysis consists in understanding the effects caused by the introduction of antennas and EM scatterers (*i.e.* multipath sources) on the VNA excitation signal. To do so, we first substitute the short-circuit configuration by an aerial link between the pair of antennas (AUT and an auxiliary antenna). By doing so, we reproduce the test setup from Fig. 3.2a and get the AUT time-domain response. In a second moment, we keep this test setup and simply introduce a metallic surface between the antennas, as illustrated in Fig. 3.7. Besides, we also increase the distance between them in order to intensify the multipath effects – this is discussed in Section 5.1.1.

Results from the time-domain analyses are summarized in Figs. 3.8-3.10. In Fig. 3.8, two waveforms are illustrated: the VNA excitation signal and the AUT response. The VNA excitation waveform reveals two things. First, the propagation time is negligible, as expected. The SOLT calibration procedure cancels the propagation delay introduced by the cables. Second, the apparent non-causality related to the presence of energy in negative time instants is due to a windowing effect. This results from the user-defined

Figure 3.7 – Measurements in Cha1 using a copper plate as reflector to introduce multipath.

frequency span, which represents a frequency domain window.

By comparing the curves in Fig. 3.8, one can conclude that the substitution of a short-circuit by an antenna set introduces a delay of approximately 5 ns. This amount of time is compatible with the wave propagation time for a distance of approximately 1 m between the antennas. However, the most important fact revealed by Fig. 3.8 is that AUT4 spreads the VNA excitation pulse. This is due to the fact that every antenna has a particular response face to a standard excitation waveform. For example, in (49) the authors analyze the time-domain step responses of a few patch antennas. They call theses responses the antenna *electromagnetic signature*. Although we do not use the same antenna characterization technique adopted by these authors, we keep the notation. So, throughout this work we consider that the S_{12} waveform in time domain, obtained with the AUT and an auxiliary antenna, represents the AUT electromagnetic signature.

Multipath is another aspect analysed here. Figure 3.9 shows a comparison between the antennas link strength obtained through the test setup in Fig. 3.7 with and without a reflector. From the black graph, it can be seen that a second pulse arrives at the receiving antenna almost at the same time than the line-of-sight version does, causing a total constructive combination. This can lead to an over-estimation of the AUT4 gain values. Furthermore, since this combination is not always totally constructive, there can be other effects as well, as exemplified in Fig. 3.10.

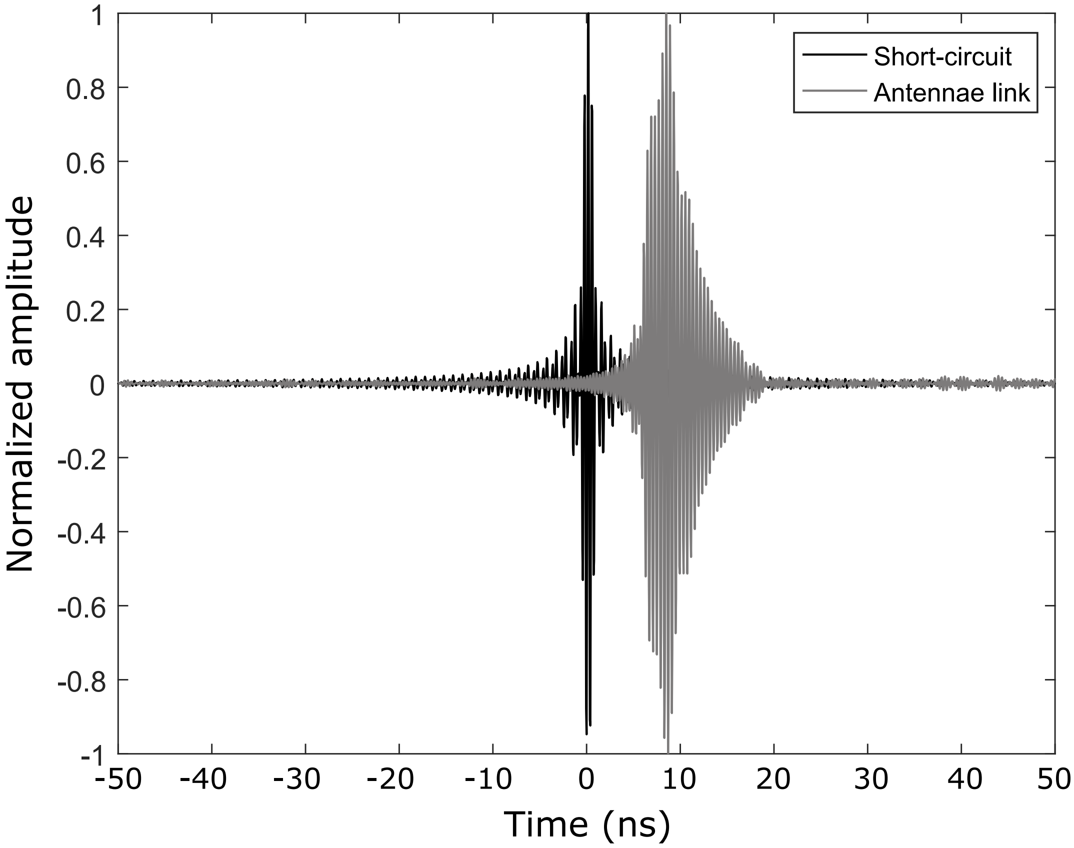

Figure 3.8 – S_{12} time-domain behavior obtained in Cha1 by short-circuiting the VNA ports (black curve) and by establishing an antenna link (gray curve). This graph evidences the channel propagation delay and the AUT4 electromagnetic signature.

After a series of chamber measurements, we now show the AUT4 electromagnetic signature obtained in non-ideal conditions. Figure 3.10 shows such a waveform, which was measured in Lab1. This figure contains two traces: the S_{12} signal (electromagnetic signature) and an envelope function – the last one was added to facilitate the analyses. A comparison between the gray graphs in Figs. 3.8 (chamber measurements) and 3.10 (lab measurements) reveals different measurements for the same antenna. The most relevant aspect in this comparison is the presence of a second pulse in the lab measurement, which is not seen in the chamber waveform. According to Fig. 3.10, it arrives at the VNA receiving port just a few nanoseconds after the first one. Given these characteristics, we attribute it to one or more multipath sources present in the neighborhood of the test setup in Lab1. As a consequence, the AUT4 electromagnetic signature is distorted, as evidenced by the envelope function. One possible consequence is an under-estimation of the antenna bandwidth (BW), once the original time-domain pulse is enlarged.

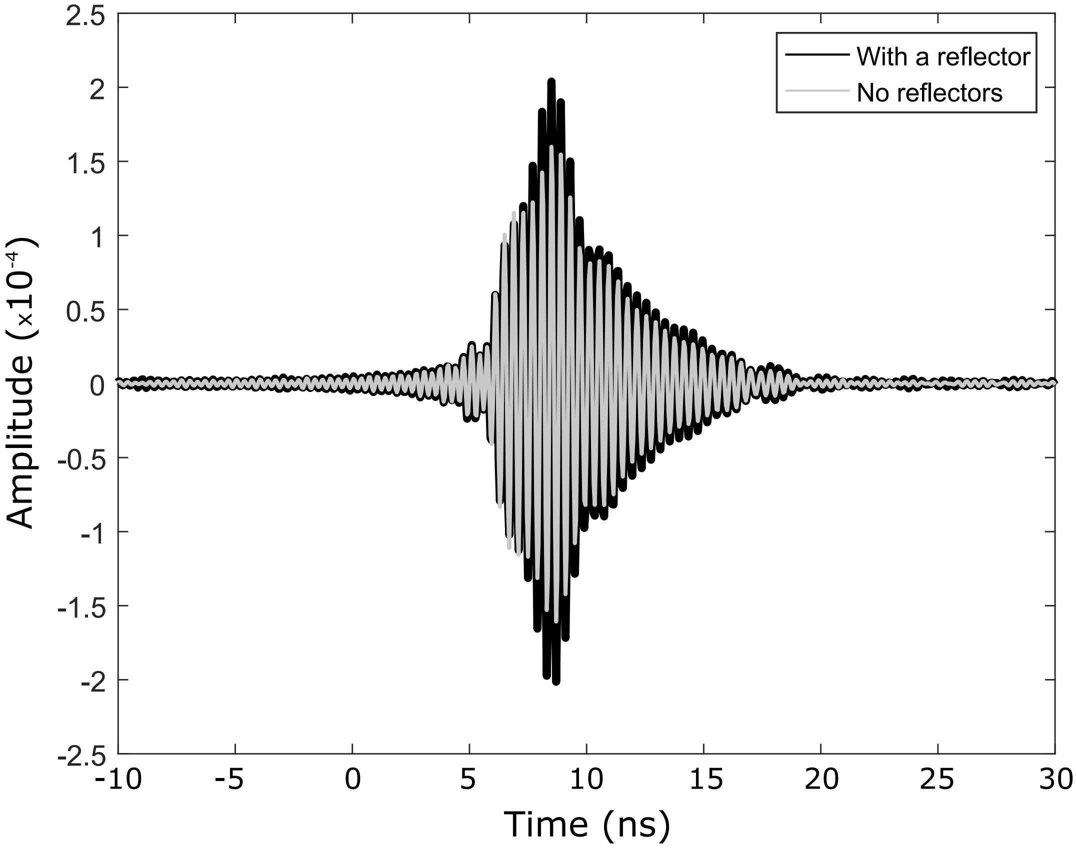

Figure 3.9 – AUT4 S_{12} time-domain behavior, obtained in Cha1 with and without a reflector, evidencing a strong multipath peak that coindides with the actual one.

3.2.2.2 EMI

The main EMI sources identified during the experiments are the wireless internet routers located nearby the test setups from Figs. 3.1a and 3.1b. Understanding the dynamic behavior of such undesirable signals is then crucial to predict worst case scenarios and their impacts over the gain estimation. To do so, a specific test setup comprising an EMC analyser (Agilent E7402A) connected to a computer via an IEEE 488 bus and a horn antenna (DRG SAS-200/571) was set in Lab2, as illustrated in Fig. 3.11.

The time domain behavior of the IEEE 802.11 network at Lab2 was then obtained for 50 ms duration intervals, as illustrated in Figs. 3.12a and 3.12b. These are power *versus* time plots for the 2.44 GHz frequency. They were recorded in sequence with a very short period of time in between.

The waveforms from Figs. 3.12a and 3.12b essentially reveal two different transmission patterns. One of them has a relatively long duration and a constant low power level of approximately -80 dBm. The second pattern is very short, more recurrent and with much higher power levels, reaching approximately -40 dBm. We attribute the first

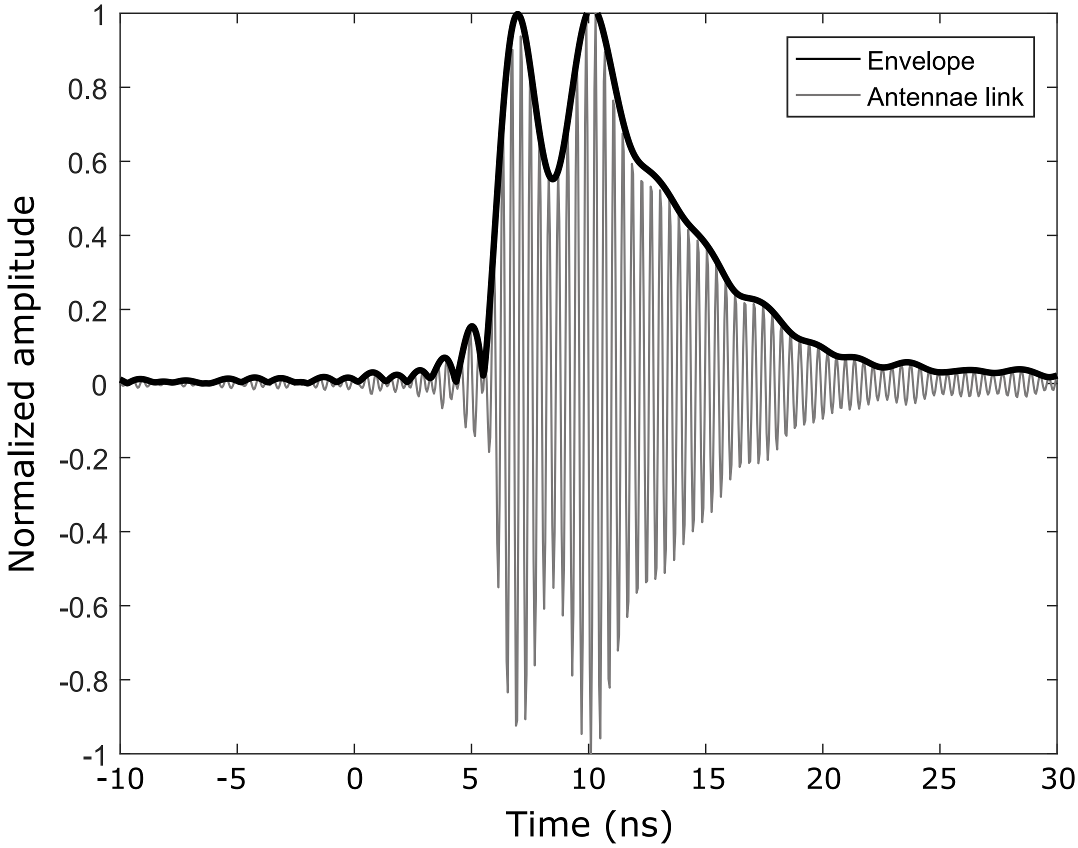

Figure 3.10 – AUT4 S_{12} time-domain behavior, obtained in Lab1, and the corresponding envelope function evidencing a strong multipath peak a few nanoseconds after the actual one.

one to data exchanges between the router and a mobile station. On the other hand, the short, high power pulses are attributed to beacon signals sent by the router.

Beacons are signals broadcast by WiFi access points (APs). They allow potential clients within a given area to know about the existence of an AP. Among other things, they allow roaming, meaning that a given mobile client can change from one AP to a nearer one (27). So, for example, if a client is moving between two APs, it receives two beacon signals with different power levels. With this information, it can start the process to switch from one AP (with low-power beacon) to another one (with high-power beacon).

An analysis of Figs. 3.12a and 3.12b focused on the beacon signaling occurrence reveals different scenarios. While in Fig. 3.12a these beacons appear less frequently, in Fig. 3.12b they are quite more numerous. This happens because the AP controls the beacon broadcast according to the channel traffic, as specified by the IEEE 802.11 protocol. In nominal conditions, a constant beacon interval (BI) makes this broadcast to be periodic. In busy channels, however, the AP has to wait for the traffic to slow down so it can broadcast data. Meanwhile, the beacons stay in a queue. The resulting delays cause the actual BI to

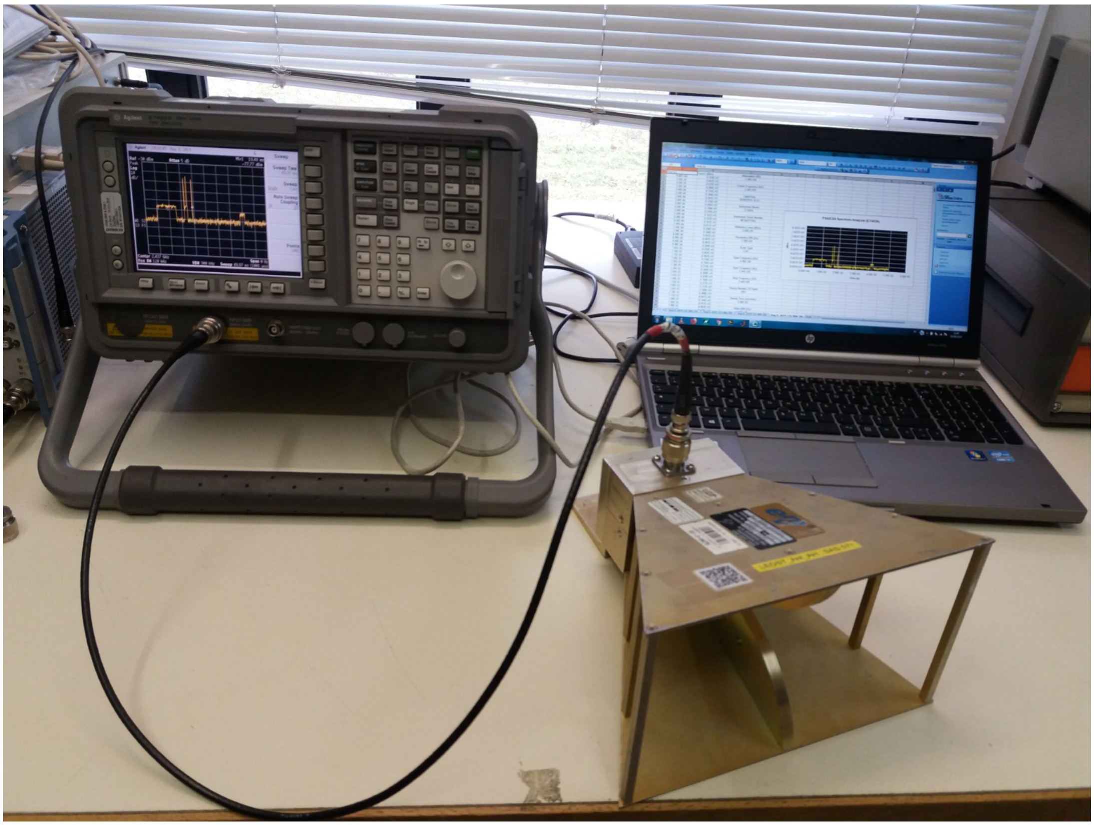

Figure 3.11 – Test setup for the monitoring of the IEEE 802.11 network at Lab2.

be different from the previously established one (50). Based on this, we conclude that the network traffic is much more intense in Fig. 3.12a than in Fig. 3.12b.

From the antenna calibration problem perspective, the most critical aspect of the mentioned signals is their power. More specifically, the power in the moment an S_{12} measurement is recorded. Since this is a time-varying unpredictable event (once it depends on the instantaneous channel conditions among other uncontrollable variables), adaptive filtering is a particularly attractive solution.

3.2.2.3 Thermal noise

The thermal noise is an undesirable but unavoidable phenomenon which is noted in electronic devices in general. It consists on the random movement of electrons in conductors despite of an external supply. It is due to their thermal activity and therefore it is associated with temperature only (51). From a measurement perspective, the thermal noise manifests itself as random, low power levels along a broad range of frequencies, similar in shape to white noise. Given its random nature, its effects cannot be compensated via calibration before the measurements, in opposition to the power attenuation and time delay introduced by the cables, for instance (52). Details about the VNA calibration can be found in Appendix B.

In the present investigation, we are concerned about the thermal noise in VNAs.

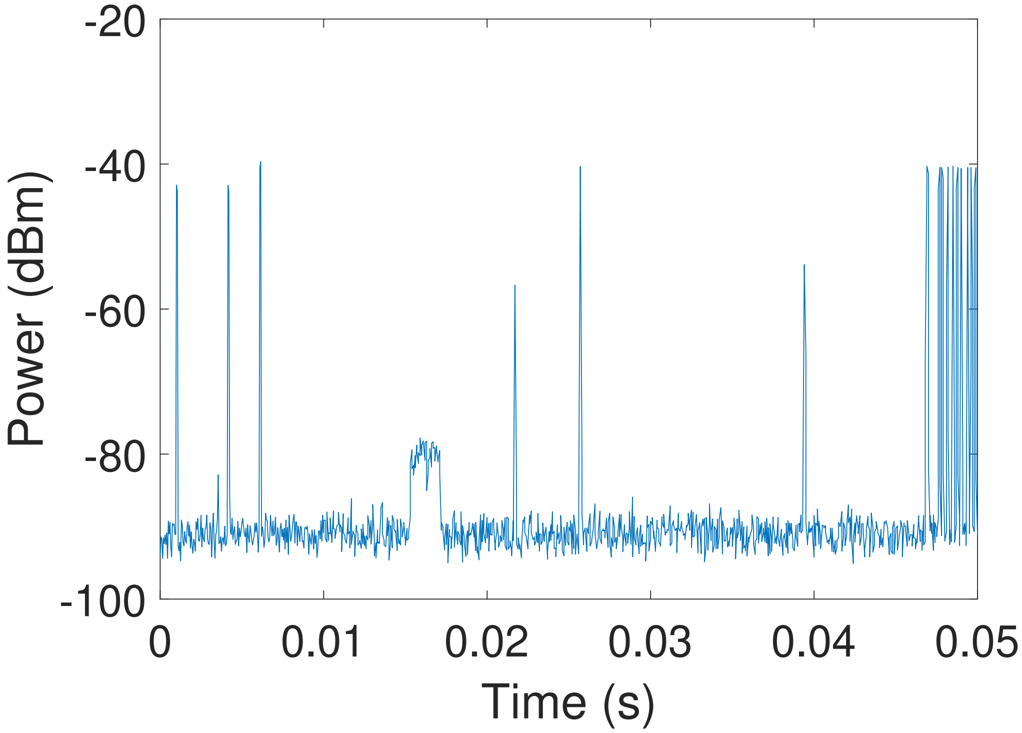

(a)

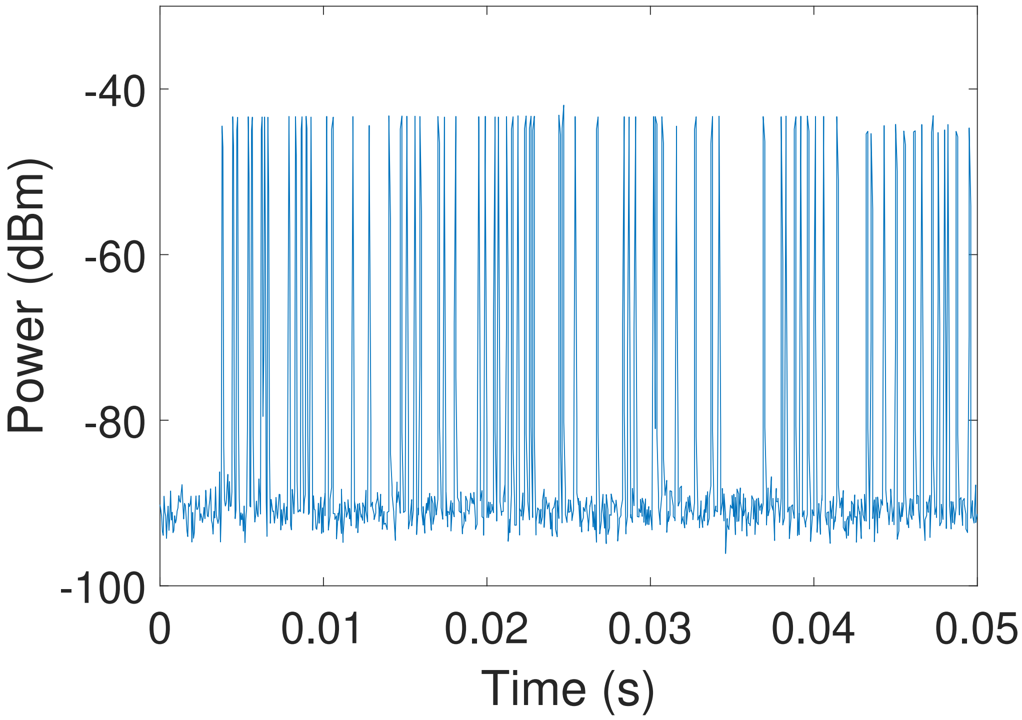

(b)

Figure 3.12 – WiFi traffic in Lab2 expressed through the power dynamics in 2.44 GHz. These waveforms reveal two different patterns: low-power less recurrent longer pulses (communication between AP and client) and high-power more recurrent shorter pulses (beacon signaling). (a) Intense traffic. (b) Low traffic.

The main consequence in this case is a reduction in the equipment dynamic range, *i.e.* the difference between the maximum and minimum tolerable/detecTable power levels. This results from the fact that the minimum detecTable power equals the thermal noise, which is given by $P_{TN} = k \times B \times T$, with k being the Boltzman constant (in joules per kelvin), B the VNA frequency resolution (also known as the resolution bandwidth or simply RBW, in 1/seconds) and T the room temperature (in kelvin) (53). This expression reveals that the thermal noise is not frequency-dependent and hence it is usually treated as white noise. Still, other noise sources coming from the VNA internal circuit can make the measurement noise floor increase for higher frequencies (52).

For the present purposes, the thermal noise effects over the S_{12} measurements are of major interest. This is because noisy contributions over these measurements can result in antenna gain estimation errors. Fortunately, the thermal noise effects tend to be more severe in S_{11} (reflection) parameters than in S_{12} (52). According to the mentioned author, this is due to the fact that the DUT reflection power levels are measured by the VNA internal circuit in the same port where the incident wave is evaluated (for more details about the VNA measurement mechanism, please refer to the Appendix A). Since the incident wave power is much higher than that of the reflected wave, this sort of measurement becomes more susceptible to errors. On the other hand, since the VNA uses different ports to measure the S_{12} (*i.e.* port 1 for incident power and port 2 for the transmitted power), it becomes less susceptible to estimation errors in this condition and therefore more robust to thermal noise.

Thus, analyses involving thermal noise in DUTs reflection coefficient extraction are more common (54). Based on the assumption that one may want to use our methodology in the *realized gain* extraction, which is an antenna property that takes into account the reflections, we analyse thermal noise worst-case scenarios. To do so, we reduce the VNA power levels in some measurements in an attempt to reach its minimum power threshold.

3.3 IEMI problem

3.3.1 GSM-R and jamming signals

The GSM-R communications are based on the GMSK digital modulation technique. This is a phase modulation scheme derived from the minimum shift keying (MSK). Both GMSK and MSK are quadrature schemes, which means they allow the simultaneous transmission of two data sets. This requires two carriers with a 90 degrees shift between them. Consequently, the GMSK signal results from the sum of two signals: in-phase (I) and quadrature (Q) (55).

The difference between these two techniques is the presence of a pre-modulation

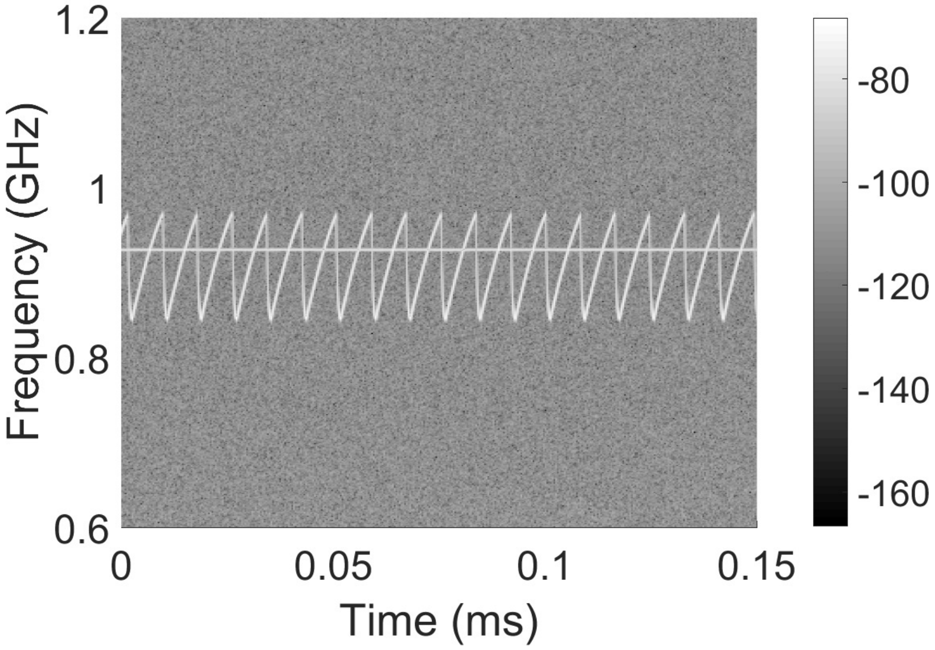

Figure 3.13 – Spectrogram of typical GSM-R and jamming signals. These signals are represented by a straight line and by a sawtooth waveform, respectively.

gaussian filter in GMSK. Such a feature allows smoother phase transitions and therefore less out-of-band radiation. By limiting the filter bandwidth with an important parameter called BT product (B is the filter bandwidth and T is the bit period), it is possible to eliminate the frequency content associated with the sharp phase transitions present in MSK (55).

The GSM-R signal power levels at the receiving antenna of the mobile station vary according to the train position within a cell. According to (4), these levels usually vary between -95 dBm (far from the base-station) and -25 dBm (close to the base-station). The signal bandwidth is 200 kHz.

A typical jamming waveform, on the other hand, consists of frequency modulated signals with very fast sweeps. These waveforms can vary from one jamming device to another in terms of power, sweep rate and bandwidth (31). The interaction between typical GSM-R and jamming signals is illustrated in Fig. 3.13. From this spectrogram, one can notice that the jamming signal bandwidth is much wider than that of the GSM-R. Such a characteristic allows the jamming device to cover not only the DL/UL channels of a given cell but all the GSM-R frequency sub-bands used by different base-stations along a given route.

We highlight that, with the virtual test setup described in the following subsection, we try to create simplified versions of the actual GSM-R signals. While a real process contains numerous stages, here we adopt a series of simplifications. For instance, we generate binary sequences that do not follow any standard frame structure, we only consider one user (and therefore we omit the multiple access techniques) *etc.* However, none of these simplifications compromises our analyses. This is because we do not interpret the bit sequences during our investigations. Instead, we only compare if the transmitted bits are present at the receiver. Furthermore, we try to generate a realistic GSM-R spectrum, mainly in terms of shape and bandwidth. .

3.3.2 Virtual test setup

A virtual test setup was implemented in MATLAB. In this step, we used built-in voltage-controlled oscillators (VCOs) and GMSK modulators to generate the jamming and GSM-R signals. The jamming signal was generated by exciting the VCO with a sawtooth waveform. Table 3.3 exhibits the parameters used to generate the signals, where BT is the bandwidth-time product and Sa/Sym stands for samples per symbol. After generating these signals, we controled their amplitudes in order to manipulate the SJR.

Once these signals are generated, they are summed and then they are ready to be processed by the ASP-2 algorithm. No channel model is employed. This corresponds to ideal propagation conditions. To analyse the ASP-2 output, which corresponds to the filtered GSM-R signal, we first demodulate it and then we use a built-in BER calculator – the concept of BER will be formally introduced in Section 5.2.3; here, we just need to know that lower BERs are desirable for a reliable GSM-R communication.

Figure 3.14 summarizes this process with a block diagram. Besides the already mentioned functionalities, it contains other elements. Two of these items are the bit sequence generators, identified in this diagram as *Random Bit Sequence* and *Periodic Bit Sequence*. We use these two digital sequences to analyse different autocorrelation patterns related to the GMSK signal – this topic is further discussed in Chapter 5. Besides, we create a null sequence so we can analyse the consistency of the codes. During this stage, we expect to see a null BER at the output since there is no jamming signal. If this holds true, we enable the jamming signal by connecting the VCO output to the summation block. However, if the BER is not null in the absence of jamming signals, then one has to review the code and signals. Finally, a third switch allows us to estimate the BER reduction provided by the ASP-2 algorithm. To do so, we compare the BER with and without the filters. Evidently, the switches and the other elements present in this diagram are just an illustrative representation of the codes.

Table 3.3 – Parameters used to generate the signals.

GMSK		Sawtooth waveform (VCO input)	
BT	Sa/Sym	Amplitude	Frequency
0.3	12800	0.3 V	122 kHz

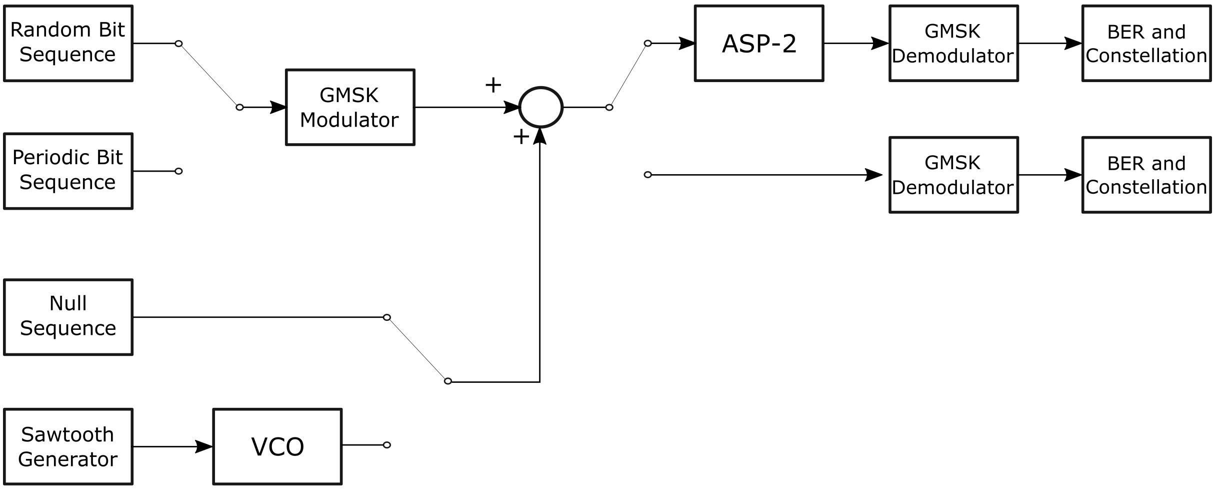

Figure 3.14 – Block diagram summarizing the computational analyses involving the GMSK signal and the ASP-2 algorithm. The switches evidence the following comparisons: random *versus* periodic bit sequences, no jamming *versus* jamming conditions and BER with and without the filters.

As a last remark, we observe that the built-in GMSK modulator output is a complex number in the time domain. Its real and imaginary parts correspond to the I and Q components of the modulated signal. This is a convenient mathematical representation which allows signal analyses such as those based on constellation diagrams. Nevertheless, the actual signals transmitted by antennas are purely real. In other words, the signal that enters the transmitting antenna is not $I + jQ$ but $I + Q$ instead.

To take this into account, we made two manipulations which were omitted from Fig. 3.14 for ease of representation. The first one is the real and imaginary parts extraction from the GMSK Modulator output and further storage in separated variables. This operation is followed by an algebraic summation which results in a purely real sequence. The second signal manipulation occurs at the GMSK Demodulator input. Considering that this block expects to receive a complex number, we have to convert a purely real sequence into a complex one. To do so, we extract the cosine and sine of the ASP-2 output signal when this block is enabled. When it is not enabled, we apply these trigonometric operators to the summation block output (see the switch after the summation block in Fig. 3.14). Then, we create a complex vector having its real and imaginary parts filled with the cosine and sine operators outputs, respectively. These manipulations are based on the GMSK modulation and demodulation schemes (55).

3.4 Final considerations

In this chapter, we provided an overview of the available experimental conditions, including some preliminary signal analyses. These analyses allows us to better comprehend the effects caused by the multipath and EMI over the S_{12} measurements. Without these special test setups, it would be difficult to comprehend the role played by each of these sources once their effects would be superimposed. Furthermore, we monitored the WiFi activity in one of the labs used for antenna calibration. This allows us to predict worst-case scenarios in terms of spurious power emissions.

Finally, we showed the frequency *versus* time behavior of typical GSM-R and jamming signals. We also detailed the computational analyses proposed for the IEMI problem. Such methodology will be used to extract some properties of the GMSK signal and to evaluate the ASP-2 technique as well.

Chapter 4

Candidate mitigation techniques

In this chapter, we review two signal processing techniques and some basic principles of design and analysis of experiments. These three approaches are potential interference mitigation techniques for the antenna calibration and IEMI problems. We show some of their advantages and possible constraints to deal with the mentioned systems.

4.1 Design and analysis of experiments

A crucial part in scientific research is the experimental planning. In this stage, one defines the most suitable way of running the tests and analyzing the results. By doing so, one can optimize the experiment execution time and avoid misinterpretation of the results. This type of approach is known as design of experiments (DOE) or design and analysis of experiments (DAE) (56; 57).

These principles are currently used by applied sciences researchers from diverse fields. For example, (58) applies a DAE principle called *sensitivity analysis* during an antenna design phase. The author wants to identify the antenna geometric parameters with higher performance impact. Such an information can be useful during the production stage, since higher tolerances can be attributed to lower impact variables. Consequently, this can ensure good performances with lower costs. Many other examples involving the use of DAE during a product or system design and/or validation phases can be found in the literature (59; 60; 61).

In this work, the main DAE-related concept that we explore is the notion of an estimator and its properties. However, before proceeding with the main definitions about estimators, let us establish the following notation:

- X: discrete random variable;
- $\mathbf{x} = \{x_1, x_2, \cdots, x_N\}$: a sample of X, where $x_1, x_2, \cdots, x_N$ are the observations and N is the sample size;

- θ: a given statistical parameter that characterizes X;
- $\widehat{\theta}$: a point estimate of θ, provided by an estimator;
- $\widehat{\Theta}$: a point estimator, *i.e.* a function of the observations, $f(\mathbf{x})$, that returns $\widehat{\theta}$.

When dealing with a random variable X, it is important to know its *expected value* (56)

$$\mathbb{E}\left\{X\right\} = \sum_{x_i \in \Omega} x_i P(x_i) \tag{4.1}$$

where $\mathbb{E}\left\{.\right\}$ is the expectation operator, $P(.)$ is the probability function and Ω is the sample space. Nevertheless, the evaluation of Eq. 4.1 in most experiments might present an important constraint: if Ω is not finite, an infinite number of observations is required. In these situations, the solution is to truncate this calculation by means of an *estimator*, $\widehat{\Theta}$, and a finite number of observations, N.

The main characteristics of an estimator are (56; 57):

1. **bias**: $\widehat{\Theta}$ is *unbiased* if $\mathbb{E}\left\{\widehat{\Theta}\right\} = \theta$, *i.e.* after all possible observations, the true statistical parameter is available – if this condition does not hold true, then the estimator has a bias given by $\mathbb{E}\left\{\widehat{\Theta}\right\} - \theta$;
2. **variance**: given a set of unbiased estimators, the most suitable one presents minimum variance around θ, being called a *consistent* estimator.

These properties are important elements of the DAE-derived methodology (to be detailed in Chapter 5) developed during the investigation of the antenna calibration problem. The proposed technique is strongly based on average calculations of antenna gain curves after a certain number of experimental runs. All the subsequent developments are possible thanks to the premise that the mean estimator, $\overline{X} = f(\mathbf{x}) = (1/N)\sum_{n=1}^{N} x_i$, is unbiased with minimum variance for a sufficiently high value of N[1] (56; 57). More specifically, since we apply this estimator to measured antenna characteristic curves, we treat each waveform as a sample and we further extract the average curve. This concept is known as *ensemble average* (62).

In this work, we developed a DAE-based technique (DAE-1), which is further compared to a similar approach reported in the literature (22), which we call DAE-2. These approaches have the conceptual simplicity and ease of implementation as attractive features. Nevertheless, the main drawback is the excessive number of experimental runs required

---

[1] This is true for Gaussian variables. But it can be extended to other distributions with a large N by means of the Central Limit Theorem (57).

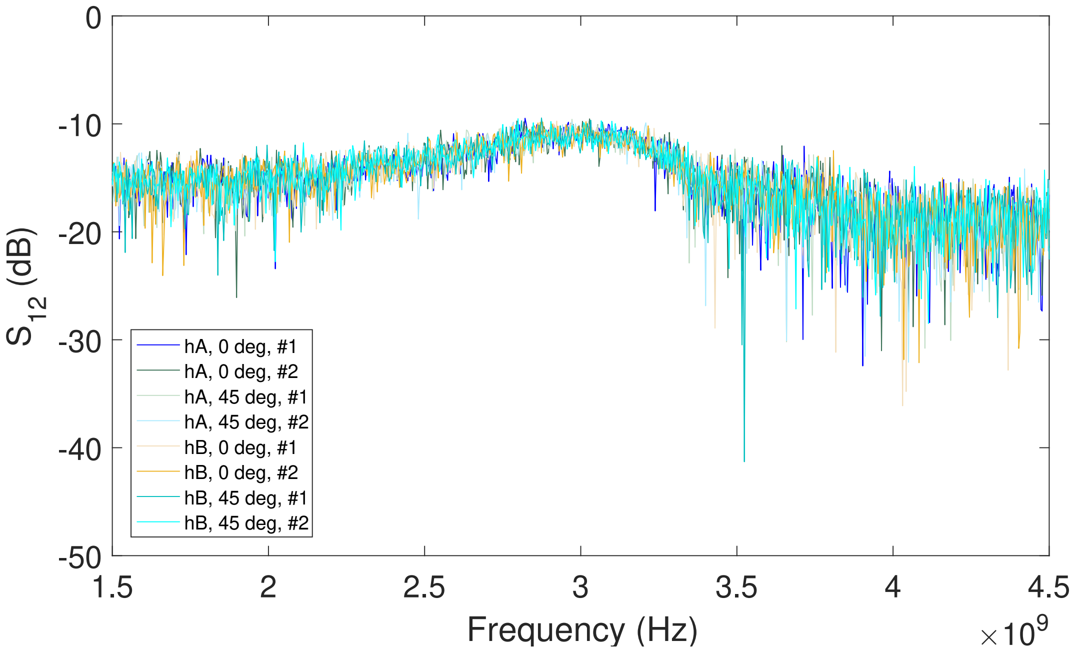

Figure 4.1 – Some measurements taken for further processing via DAE-1 and DAE-2. Legend: height of the antennas (hA or hB), rotation angle applied to the test setup (0 or 45 degrees) and a label for each sampled waveform taken from a given configuration (#1 or #2).

for an acceptable accuracy level. This long test time results from different test setup arrangements inside the lab and the need for replicated measurements. When conducting the DAE-based analyses, we considered 4 arrangements. Additionally, collected 10 samples (waveforms) for each of them, resulting in 40 experimental runs.

In order to illustrate this disadvantage, Fig. 4.1 shows a few measurements taken for further processing via DAE-1 and DAE-2. This measurement campaign was performed with AUT1 in Lab1 and with the VNA power set to -50 dBm. Each curve represents noisy S_{12} data having the thermal noise as the main degradation source. This figure does not contain all the 40 experimental runs, but it is sufficient to evidence the high amount of time required by the mentioned approaches. Evidently, a lower number of runs could be used, but resulting in degraded DAE-1 and DAE-2 performances.

4.2 Time gating

Time gating (TG) is a very common technique in the EMC field (63). It is essentially a time-domain window function, which is multiplied by the measured signal. If adequately designed, it allows the useful portion of the signal to pass without distortions and it rejects spurious elements. One of its applications is illustrated in Fig. 4.2. In this figure, a VNA is used to extract the S_{11} parameter (also known as the *return loss*) of a given DUT - a *load*, from the VNA perspective. The VNA internal source then sends

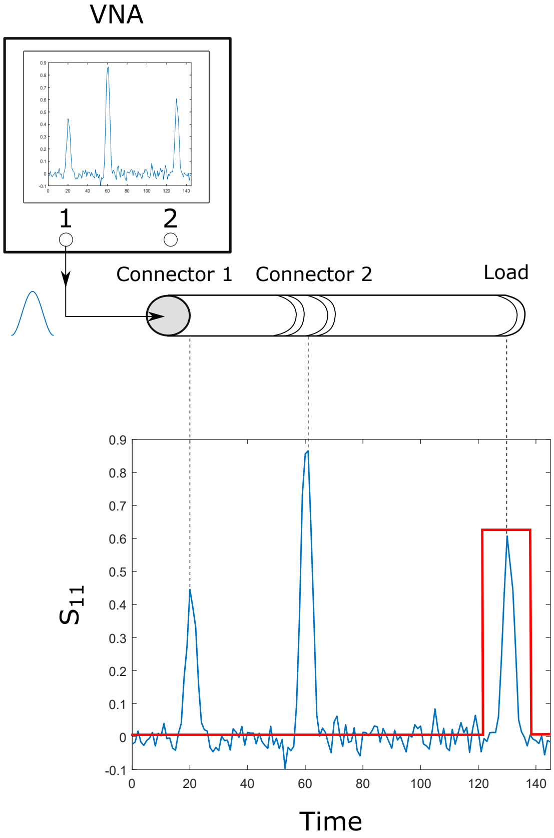

Figure 4.2 – Elimination of spurious reflections from a S_{11} measurement with TG. Adapted from (64).

a voltage pulse through the cables and reads its reflected version a certain time later. However, if there is any impedance mismatch between the VNA and cables and also between cables and connectors, other pulses may also be read. They result from partial or total destructive/constructive combinations between the incident pulse and its reflected versions. TG is then used to select only the one that comes from the load.

This type of feature can be found in most modern VNAs. Such an equipment usually allows manual adjustments of the window location, duration and shape (64). The same window functions usually adopted in the traditional frequency-domain filter design are applicable (65). Recent reports on its use by the EMC community can be found in (66; 67; 68; 69). In this work, we use TG to mainly mitigate multipath and thermal noise. The first phenomenon usually manifests itself in the form of strong secondary pulses, similarly to those illustrated in Fig. 4.2. They are partially deterministic, since they are delayed and attenuated versions of a known signal, and partially random, given the propagation channel characteristics and other stochastic events inherent to the transmission/reception processes. The thermal noise, on the other hand, is continuously present on the measurements and it is completely random.

One of the TG limitations is its inability to deal with spurious signals whose occurrence in time coincide with the useful part of a waveform. Therefore, it will certainly fail for the multipath scenarios described in Figs. 3.9 and 3.10. In this case, one can carefully define the antennas positioning in order to better control the instant in which the multipath pulses will occur. Still, space constraints can limit this approach. Finally, when it comes to thermal noise mitigation, TG cannot eliminate it during the useful signal transmission. Fortunately, the electromagnetic signatures of the AUTs used in this investigation are relatively short in time when compared to the total signal length. Therefore, most of the thermal noise energy can be eliminated. However, this can be a constraint for narrowband antennas, since their signatures tend to be larger.

Another TG constraint is its potentially poor performance in low signal-to-noise (SNR) environments. In order to demonstrate that, we artificially added a 2.4 GHz phasor, with variable amplitude and phase, to the original AUT1 S_{12} measurements and further evaluated the filter performance. These amplitude and phase variations can be noticed by a WiFi (intentional or non-intentional) receiver even in small time intervals given their mobility within certain spaces and also the intermittent nature of most IEEE 802.11 transmissions.

Figure 4.3a shows the TG responses for a signal that results from the complex sum of an AUT1 S_{12} measurement taken at Lab1 (gray curve) and an unitary phasor with variable phase. That means that we do not introduce artificial modification of the EMI amplitude; we only consider the phase impact. The filtered curves are smooth and the differences between them are negligible, which indicates that the state-of-the-art solution is suitable in this case. However, if we increase 5 or 10 times (see Figs. 4.3b and 4.3c) the amplitude of the narrow-band interference, not only are there significant differences between the curves but also none of them is satisfactory. The significant differences between the curves highlight that the TG performance depends upon the EMI phase, which is in turn an uncontrollable variable.

4.3 Adaptive filtering

4.3.1 General aspects

Adaptive filtering (AF) is a digital signal processing technique applied to many engineering problems, *e.g.* noise cancellation and system identification (35; 36). In these scenarios, the presence of random events during the measurements is common. It is though difficult to track these events, given their non-deterministic nature. In turn, such environmental conditions cannot be easily handled by the usual fixed-coefficient filters. This is the case of the two problems described in Chapter 2, where there is no (or little) control about the EMI, multipath and thermal noise sources in the antenna calibration problem; and no control at all about the jammer power in the IEMI problem. Some studies involving the AF within the EMC field have been lately published (9; 8; 70). In most of

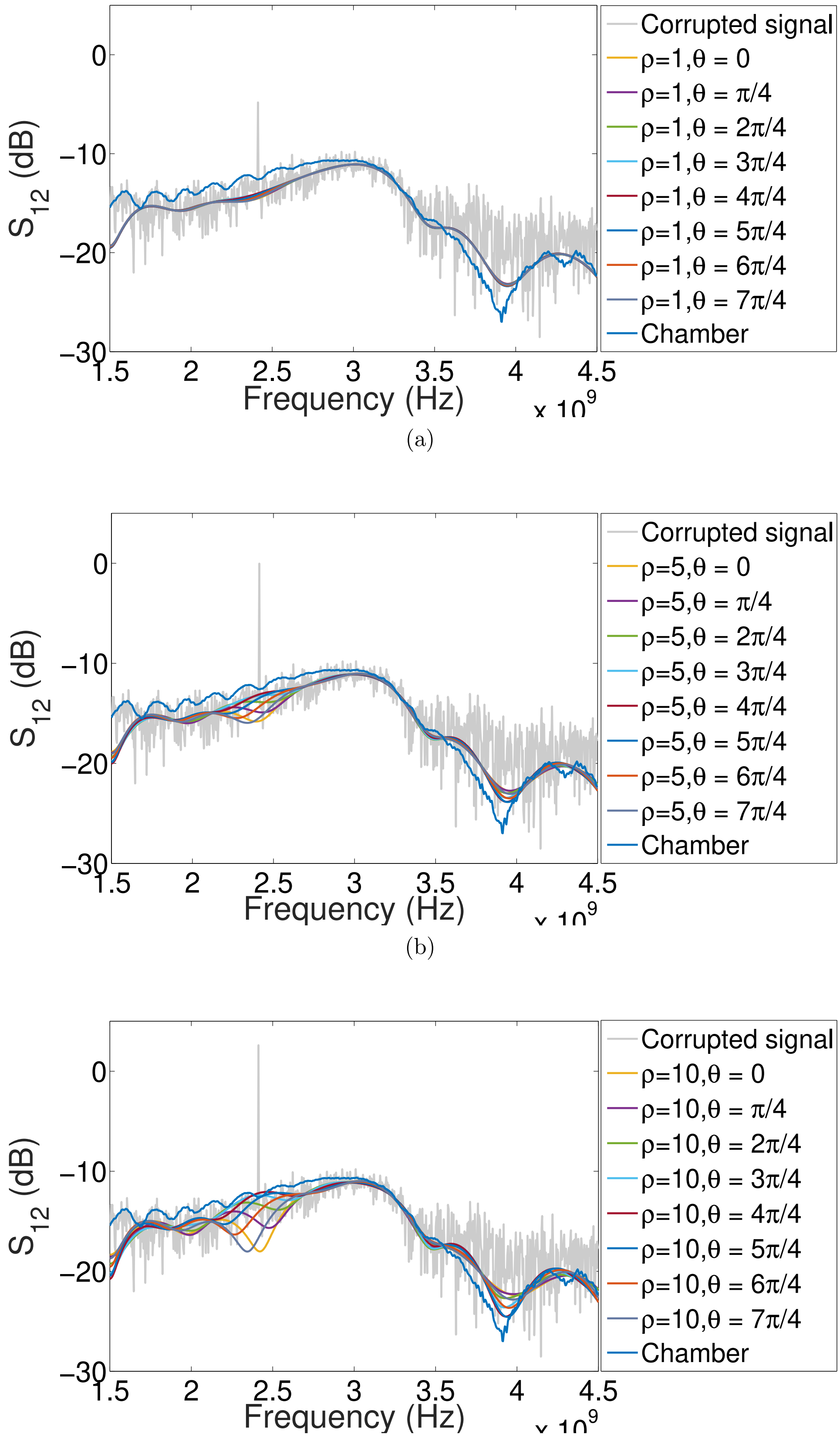

(a)

(b)

(c)

Figure 4.3 – Manually adjusted time gating applied to the noisy AUT1 S_{12} measurement added to a 2.4 GHz phasor with variable amplitude (ρ) and phase (θ).

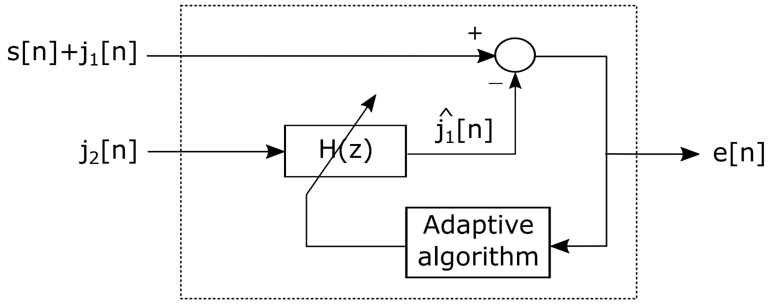

Figure 4.4 – ANC basic structure. It requires 2 inputs (the noisy measurement, $s[n]+j_1[n]$, and a noise floor sample, $j_2[n]$) and produces 1 output (the cleaned signal, $e[n]$). Thanks to an adaptive algorithm, the filter transfer function, $H(z)$, produces a noise estimate, $\widehat{j}_1[n]$, which is subtracted from the noisy input. The result is an estimate of the useful signal, $e[n] = s[n] + (j_1[n] - \widehat{j}_1[n])$.

these papers, AF is used to improve the quality of the radiated emissions test in open areas.

The classical AF structure for noise cancellation is called adaptive noise canceller (ANC). It is illustrated in Fig. 4.4 through a block diagram. In this figure, $s[n]$ is the unavailable useful signal (n being the discrete-time index), corrupted by $j_1[n]$. These components are not separately available. Instead, they are superimposed in a single waveform when the measurement is performed. The goal of the ANC filter is to separate these signals and recover $s[n]$. If the noise followed a deterministic pattern, we would simply measure it in a place where the influence of $s[n]$ is weak. Then, knowing the way it evolves with time, we could wait for a specific moment where its behavior is exactly the same of that registered in the signal measurement. In other words, we could access an exact noise replica, $j_2[n] = j_1[n]$, and fully reconstruct the useful signal by subtracting $j_2[n]$ from $s[n] + j_1[n]$. Unfortunately, this is an ideal condition which is rarely seen in practical measurements. In these cases, the noise evolves randomly over time and we have to estimate its actual contribution over a given measurement.

According to Fig. 4.4, the noise replica can be produced by $H(z)$ if we can access its source and get a sample, $j_2[n]$. From the resulting estimate, $\widehat{j}_1[n]$, an error signal is generated at the summing junction, $e[n] = s[n]+(j_1[n]-\widehat{j}_1[n])$. This information is used by an adaptive algorithm to update the $H(z)$ coefficients (or, analogously, the filter impulse response coefficients), aiming better noise estimates. This process continues recursively until convergence. In steady-state, the term $(j_1[n]-\widehat{j}_1[n])$ is minimized and $e[n]$ approaches $s[n]$ with a given residual discrepancy (35; 36).

4.3.2 Two important premises

A successful AF process presumes that (i) a measurement of $j_2[n]$ is available and (ii) the cross-correlation between $j_1[n]$ and $j_2[n]$ is high. Unfortunately, these two premises do not hold simultaneously true for the two problems investigated here. Consequently, some constraints can be imposed, as explained in the following paragraphs.

In the antenna calibration problem, $s[n] + j_1[n]$ is a S_{12} measurement in a non-ideal OATS and $j_2[n]$ is the noise floor, measured by substituting the auxiliary antennas from Fig. 3.1 by 50 Ω loads. By doing so, the AUT will not receive radiated energy from the auxiliary antenna but only from external EMI sources. As a critical consequence, although $j_1[n]$ might encompass EMI, multipath and thermal noise, $j_2[n]$ does not cover the multipath effects. This is due to the fact that there is no mutipath without the transmitting antenna. Furthermore, since the thermal noise is completely random, its contribution to $j_1[n]$ and to $j_2[n]$ are totally uncorrelated with each other. These observations indicate that the premise (ii) can be compromised in the antenna calibration problem. Consequently, the ANC filter performance can be partially degraded.

On the other hand, we cannot measure $j_2[n]$ in the IEMI problem. This is because the only way of collecting measurements in a practical situation it through the roof antenna of a train in movement. This antenna is in turn designed to be a GSM-R receiver and therefore it will always have a link with some base-station. In summary, a jamming signal sample is not separately available and premise (i) does not hold true in the IEMI problem.

In this dissertation, we present two signal processing tools to address the above problems. In one of the proposed approaches – to be detailed in Chapter 5 – the constraints of the ANC filter to handle multipath and random noise are compensated with an additional filtering stage based on TG. Furthermore, the problem of measuring the $j_2[n]$ signal is solved with an AF configuration known as adaptive line enhancer.

4.3.3 The NLMS adaptive algorithm and its parameter dependency

In this work, we use the normalized least mean squares algorithm to update the filter impulse response according to the following process (35):

$$\mathbf{h}[n] = \mathbf{h}[n-1] - \mu \widehat{\nabla} \mathbb{E}\{e^2[n]\}, \tag{4.2}$$

where n is the discrete time index; $\mathbf{h}$ is the L-size filter impulse response vector (also known as its *weights*) with L being the filter *order* (or *length*); $\mu = \mu_0/(\epsilon + \|\mathbf{u_n}\|^2)$ is called *step-size*, where μ_0 is a constant defined within the $0 < \mu_0 < 1$ interval, ϵ is a small positive constant (usually $<< 1$) called *regularization parameter* and $\mathbf{u_n}$ is called the *regressor vector*[2]; $\mathbb{E}\{.\}$ is the expectation operator; e is the *error* signal; $\mathbb{E}\{e^2[n]\}$ is the mean squared error (MSE) and $\widehat{\nabla}\mathbb{E}\{e^2[n]\}$ is an estimate of the associated gradient

---

[2] The regressor vector contains the current and past values of the filter input signal ($j_2[n]$, according to our notation) in a total of L samples, where L is the filter order or length.

function. This is a gradient-based optimization algorithm which aims to find the impulse response vector that minimizes the MSE and therefore ensures that $e[n] \to s[n]$. In practical situations, all signals are random and the gradient true value is not available because of the limited information about their statistical properties. In this case, one can obtain a gradient estimate by means of the instantaneous cross-correlation between $\mathbf{u_n}$ and $e[n]$, given by $\widehat{\nabla}\mathbb{E}\{e^2[n]\} = \mathbf{u_n}e[n]$ (35).

The convergence of the process described by Eq. 4.2 strongly depends on the filter order (L) and step-size (μ) values. These parameters define the process convergence speed and accuracy. In other words, they define the number of required iterations and also how similar the ANC output signal and the useful part of the corrupted measurement are.

In order to show how sensitive the AF can be to the choice of parameters, we consider a pair of S_{12} and noise floor measurements, taken at Lab1 using AUT1 along the 2-3 GHz frequency range. We then use these signals to feed a set of different and independent ANC filters whose parameters are defined by several (μ, L) coordinates within the intervals $0 \leq L \leq 100$, $0 \leq \mu_0 \leq 0.1$. Each filtered gain curve coming from the k^{th} AF, $\mathbf{G}_k$, is compared to a reference chamber curve, $\mathbf{G}_{ref}$, obtained at Cha1.

Based on these two gain curves, we define the following function, which is inversely proportional to the filter performance

$$f = (\mathbf{G}_k - \mathbf{G_{ref}})(\mathbf{G}_k - \mathbf{G_{ref}})^H|_{2<f<3GHz} + 0.1(\mathbf{G}_k - \mathbf{G_{ref}})(\mathbf{G}_k - \mathbf{G_{ref}})^H|_{2.4GHz} \tag{4.3}$$

where the index k denotes the k^{th} candidate solution; $(.)^H$ is the Hermitian operator (*i.e.* the conjugate transpose); $(.)|_{2<f<3GHz}$ means evaluation over the $2 < f < 3$ GHz frequency band and $(.)|_{2.4GHz}$ means evaluation only at 2.4GHz. Equation 4.3 was designed to faithfully represent the inverse of the filter performance. If we analyse its two terms, $(\mathbf{G}_k - \mathbf{G_{ref}})(\mathbf{G}_k - \mathbf{G_{ref}})^H|_{2<f<3GHz}$ and $0.1(\mathbf{G}_k - \mathbf{G_{ref}})(\mathbf{G}_k - \mathbf{G_{ref}})^H|_{2.4GHz}$, we realize that they represent the squared difference between a filtered curve, $\mathbf{G}_k$, and that obtained in the anechoic chamber, $\mathbf{G}_{ref}$. Since the gain is frequency dependent, it is represented by a $\Pi \times 1$ vector, where Π is the number of frequency samples. Therefore, Eq. 4.3 is the summation of two terms of $(\Pi \times 1) \times (1 \times \Pi) = (\Pi \times \Pi)$ dimension each. The resulting matrix maps the surface illustrated in Fig. 4.5 – to be described soon.

The presence of a separate term in Eq. 4.3 for the 2.4 GHz frequency is justified by the importance of this spectral component in our experiments. This is due to the presence of a WiFi router in the vicinity of the antenna calibration test setup. Hence, Eq. 4.3 emphasizes the filters that faithfully reconstruct the gain curve shape at the EMI frequency. According to this equation, the 2.4 GHz term is weighted by a 0.1 constant. This value was defined in such a way as to emphasize the signal reconstitution near the

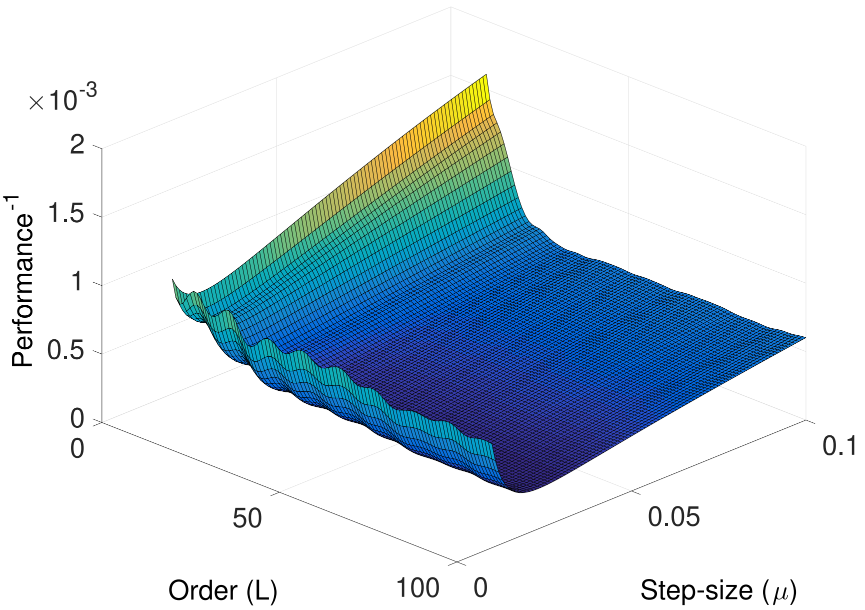

Figure 4.5 – Filter performance as a function of its parameters. Low values: good performance; high values: poor performance. All (μ, L) configurations were evaluated with the same number of iterations so some of them – specially those with very low step-sizes – may not have converged.

EMI frequency but, at the same time, ensuring a good filtering performance over the entire 2-3 GHz range.

Figure 4.5 is a plot of Eq. 4.3 over the (μ, L) plane. It demonstrates the filter sensitivity to the parameters' selection. As an example, if we move from $(0.014, 33)$ to $(0.099, 10)$ in the (μ, L) plane, the function described in Eq. 4.3 increases about 4 times. Such a sensitivity to the parameters choice makes the AF implementation a difficult task in EMC labs. This is because EMC engineers and technicians do not necessarily have a solid signal processing background/experience. Therefore, a filtering performance degradation can be observed as a consequence of an unfortunate parameter selection.

An important observation concerning Fig. 4.5 refers to the number of NLMS iterations used to generate the three-dimensional plot. Each point in this surface results from the iterative process defined by Eq. 4.2. Since we used the same number of iterations for all the (μ, L) combinations, it is possible that in some cases the NLMS filters have not converged to their optimum solutions. Based on this, we believe that the sharp increase observed in the function values near $\mu = 0.01$ (which seems to be independent of L) is due to the fact that these AFs have not yet converged when we stopped the processes.

In Chapter 5, we present a solution for this problem based on the particle swarm optimization technique. By doing so, we expect to automatically generate (μ, L) parameters that ensure the best AF performance.

4.3.4 Multipath and thermal noise filtering constraints

To show the limitation of the ANC structure in Fig. 4.4 to mitigate wave reflection effects in the antenna calibration problem, we make an analogy with audio engineering. We do this because AF is a classical solution for echo problems in voice communications. With this example, we try to demonstrate the differences between the audio engineering and antenna calibration issues.

In voice communications, there is an undesirable situation which occurs when a speaker hears his own voice a certain time later. These echoes result from the reflection of electric or sound waves. The first case is usually noted in telephony and is due to impedance mismatches or other imperfections present in the line. (2) attributes this problem to a device called *hybrid transformer*. On the other hand, the sound propagation in closed places such as auditoriums can generate a reflection pattern. This can in turn result in an undesirable acoustic coupling between microphone and loudspeaker. There are many situations where this phenomenon can be noted, *e.g.* hands-free telephony, voice over internet protocol (VoIP) calls, auditorium speeches *etc* (35).

AF is a classical solution for the mentioned problems, also called the network (telephony) and acoustic echo cancellation problems (2). Nevertheless, the ANC configuration used in the current research (see Fig. 4.4) is not the AF solution usually adopted in audio engineering. In such case, the *system identification* configuration, illustrated in Fig. 4.6, is preferred. In this figure, $H_2(z)$ is the *actual* transfer function of the channel where the voice signal propagates. In other words, it models the physical phenomena responsible for the echoes. Therefore, $H_2(z)$ represents an auditorium in the sound propagation case, the hybrid transformer in telephony or any other voice channel. On the other hand, $H_1(z)$ is an *artificial* transfer function that mimics $H_2(z)$. Consequently, the output of the $H_1(z)$ block is an echo estimate.

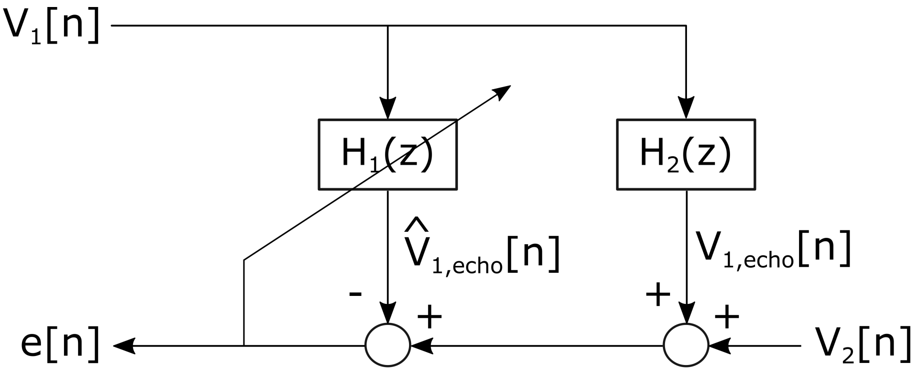

Figure 4.6 – AF configuration used for network and acoustic echo cancellation, based on (2). $v_1[n]$ and $v_2[n]$ are useful voice sources (1 and 2 identify the participants of a talk). $v_{1,echo}[n]$ and $\widehat{v}_{1,echo}[n]$ represent an echo and its estimate. $H_1(z)$ and $H_2(z)$ are the filter and an unknown system's transfer function, the latter being the responsible for the echoes. Finally, $e[n]$ is a reconstruction of $v_2[n]$.

In the block diagram illustrated in Fig. 4.6, we attribute the subscripts 1 and 2 to the participants of a conversation. In some situations, it is possible that speaker 2 does not exist (*e.g.* in an auditorium where a speech is being held). Besides, one can note in Fig. 4.6 that an echo, $v_{1,echo}[n]$, is generated by $H_2(z)$ from a useful voice signal, $v_1[n]$. The echo is in turn summed to the speaker 2's voice, $v_2[n]$. If there is no AF in the line, speaker 1 would hear not only speaker 2's voice but also his own voice delayed and attenuated.

The main goal in this case is to adapt the filter coefficients, $H_1(z)$, so that it can mimic the system's transfer function, $H_2(z)$. When this happens, the $H_1(z)$ output is an echo estimate, $\widehat{v}_{1,echo}[n]$, and the resulting error signal, $e[n] = v_2[n] + (v_{1,echo}[n] - \widehat{v}_{1,echo}[n])$, presents mainly useful voice content (or almost no signal if speaker 2 does not exist). In this case, the error signal can be transmitted back to speaker 1's telephone (who will clearly listen to speaker 2's voice) or to a loudspeaker (who will transmit the speaker's voice to the audience without echo).

Nevertheless, there are a few differences between the network/acoustic echo and antenna calibration problems. In audio engineering, $H_2(z)$ is a combination of the microphone's and speaker's transfer functions (analogously to the antenna's electromagnetic signature) with that of the channel. But since one is not interested in modeling neither the microphone nor the speakers behaviors, this is not a problem. In our investigation, however, we aim to characterize the antenna – separately from the channel.

The second difference concerns the path taken by multipath since its source until its final destination. In the audio engineering problem, the same node that generates the useful signal also receives the multipath contribution – see in Fig. 4.6 that $v_{1,echo}[n]$ returns to the same source that generated $v_1[n]$. However, this does not happen in the antenna calibration problem. In this case, the multipath always reaches the receiving antenna and we neglect the reflected waves that return to the transmitting antenna.

Based on the above-mentioned differences, we believe the structure illustrated in Fig. 4.6 would have to be modified in order to solve the multipath problem we face. So, we assume that AF can present limitations while trying to eliminate such spurious contribution. To compensate that, we use TG as it will be explained in the next chapter.

Multipath cancelling can be challenging in other engineering applications as well. A number of recent studies on this topic can be found. As an example, we can mention the study described in (71). The authors propose a few AF techniques to deal with the position estimation errors caused by multipath in global positioning system (GPS) systems. In particular, they deal with a mobile receiver and with non-gaussian noise sources present in the communication channel.

Finally, we discuss the inability of the ANC filter from Fig. 4.4 to solve thermal noise. If we consider the premises described in Section 4.3.2, then the conclusion for such question is straightforward. Thermal noise is essentially random - see Section 3.2.2.3. Therefore, $j_1[n]$ and $j_2[n]$ will always be uncorrelated with each other. Consequently, the noise estimate produced by the filter, $\widehat{j}_1[n]$, will never be faithful.

4.4 Summary of the candidate techniques limitations

In this section, we briefly described three techniques which are potential candidates to solve the antenna calibration and IEMI problems. We also discussed some possible limitations that they can present in certain situations, which are summarized in Table 4.1. Nevertheless, these limitations were verified under specific conditions. Therefore, it is possible that such constraints do not occur in other scenarios. As an example, although not suitable to mitigate multipath in the antenna calibration problem, the AF is used to eliminate acoustic echo in audio engineering.

Table 4.1 – State-of-the-art approaches and their constraints for the antenna calibration and IEMI problems.

Technique	Limitation
Time gating	Performance can be degraded in low SNR environments
DAE	Time consuming
Adaptive filtering	Limitations to cancel multipath and thermal noise
Adaptive filtering	High parameter dependency
Adaptive filtering	It requires an isolated noise measurement

Chapter 5

Proposed methodologies

In this chapter, we detail the main contributions of the present research: the DAE-1, ASP-1 and ASP-2 techniques. The first two are applied to the antenna calibration problem, while the last one refers to the IEMI case study. They are presented here based on the assumptions that all signals have been previously collected. Finally, we define metrics that allow us to evaluate the performance of the proposed techniques.

5.1 Antenna calibration problem

5.1.1 DAE-1

The first mitigation technique that we propose for the antenna calibration problem is called DAE-1. With this approach, we take two main premises into consideration. The first one is that the EMI and multipath phenomena can present space and/or time symmetries. Unfortunately, we cannot say the same for the thermal noise, since it is completely random. The second premise is that the classical mean estimator, $\overline{\Theta} = (1/N)\sum_{n=1}^{N}\Theta_i$, is unbiased and consistent, as already discussed in Section 4.1. Based on this, we propose an experimental planning that allows us to obtain an average S_{12} *versus* frequency curve from a measurement campaign with a certain number of experimental runs. With this, we expect that the average curve will present a higher correlation with the chamber measurements than each individual noisy waveform.

Another set of premises is also considered, as follows:

- the wave propagation between the two antennas in Figs. 3.1a and 3.1b can be described by the two-ray model – details about this model can be found in (72);
- the total number of experimental runs, N, shall be high enough to ensure that the S_{12} estimator variance is low – according to (57), Ch. 3, the *estimated standard error* of Gaussian variables is inversely proportional to the square root of N.

The two-ray propagation model is based on optical physics and therefore it describes the wave propagation with rays. More specifically, it only considers two rays reaching a receiver antenna: one of them, called line-of-sight, is a direct link between transmitter and receiver, while the second one is a reflected version. The reflection in this case occurs at the metallic floor. This model has been used with a reasonable accuracy to predict the received signal level in certain mobile systems (72).

On the other hand, an optimal number of experimental runs can be obtained from a trade-off between accuracy and test duration. One way of doing this is by storing the peak values of successive S_{12} measurements. These values are linked to the antenna central frequency and, by means of the Friis equation, can be transformed into the peak gain. Each time a new peak gain is stored, a sample average can be calculated. From this moment on, one can define when to stop the process based on the estimate variance, which shall be less than a previously established threshold.

Furthermore, the development of the DAE-1 methodology is based on the following observations:

- the effects of signal reflections on the walls and EMI over the line-of-sight component can be minimized if we rotate the test setup, keeping the antenna heights and the distance between them fixed;
- the effects of reflections on the floor over the line-of-sight component can be minimized if we vertically shift the antennas while keeping the distance between them fixed;
- the distance between the antennas is a trade-off between the multipath effects over the gain estimates and the far-field premise (necessary for the gain calculation via Friis equation): small distances minimizes the multipath effects but tend to violate the mentioned premise and vice-versa.

These are not premises but only expectations we have based on previous experiences with EM measurements.

The mitigation of the signal reflections on the walls is illustrated in Fig. 5.1. This figure shows the antenna pair in three different positions, all with the same height and separation distance. It also shows metallic walls, floor and object, the last one in a random location in the lab. This approach is based on the assumption that the time when a reflected signal coming from the walls or nearby objects arrives at the receiving antenna can be controlled in a certain way by manipulating the antenna locations. For some antenna arrangements, the propagation time of certain multipath components will be so long that this effect will be negligible. Our idea is to rotate the test setup and, for each new position, record S_{12} measurements. Some of these arrangements will lead to strong

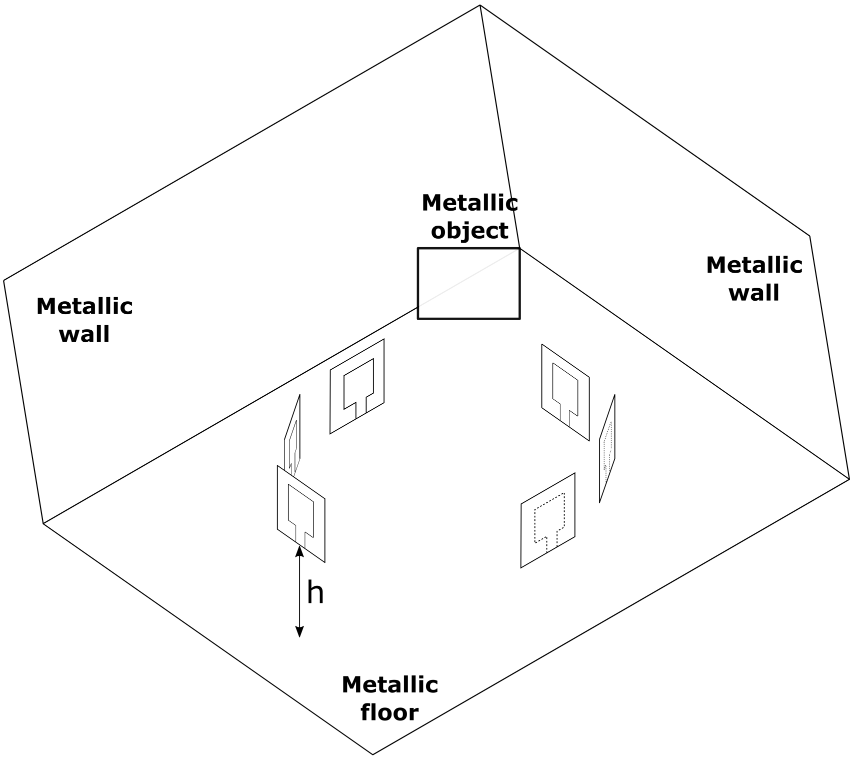

Figure 5.1 – Illustration of the multipath cancelling methodology based on rotations over the test setup, valid for reflections on the walls and objects nearby. The rotations allows one to control the phase of the reflected signals at the receiver. After a series of measurements, we expect that the average multipath contribution will vanish.

multipath effects while others may result in less intense effects. Therefore, we expect that, on average, the multipath components will be minimized.

After the minimization of the wall reflection effects, we deal now with the floor influence. Figure 5.2 illustrates the proposed approach. It is possible to identify in this figure two different heights from the metallic floor, h_A and h_B. It is also clear that the separation distance, d, is kept constant. In the following lines, we show that convenient height choices can generate, on average, a 180 degrees shift between the multipath signals.

Let's initially consider the phase difference, $\Delta\phi$, between the line-of-sight signal and its reflected version at the receiver (72)

$$\Delta\phi = \frac{2\pi\Delta l}{\lambda} \tag{5.1}$$

with λ and Δl being the wavelength and the paths difference expressed in length units, respectively. If we consider that the line-of-sight phase at the receiver is the same for both heights (once the horizontal alignment is the same for h_A and h_B), we can derive the following relations from Eq. 5.1

$$\phi_{MP_A} - \phi_{VD} = \frac{2\pi \Delta l_A}{\lambda} \tag{5.2}$$

$$\phi_{MP_B} - \phi_{VD} = \frac{2\pi \Delta l_B}{\lambda}. \tag{5.3}$$

In Eqs. 5.2 and 5.3, (ϕ_{MP_A}, Δl_A) and (ϕ_{MP_B}, Δl_B) are the multipath phases and length differences to the line-of-sight components for h_A and h_B, respectively. It is known that Δl is a function of the antennas heights and distances (72), as follows

$$\Delta l = \sqrt{(h_1 + h_2)^2 + d^2} - \sqrt{(h_1 - h_2)^2 + d^2} = \sqrt{(2h)^2 + d^2} - d \tag{5.4}$$

with $h = h_A$ or h_B. If we subtract 5.3 from 5.2 and after then substitute Eq. 5.4 in the resulting expression, we get

$$\phi_{MP_A} - \phi_{MP_B} = \frac{2\pi}{\lambda} \left[\sqrt{(2h_A)^2 + d^2} - \sqrt{(2h_B)^2 + d^2} \right]. \tag{5.5}$$

Finally, by imposing the condition $\phi_{MP_A} - \phi_{MP_B} = \pi$ on Eq. 5.5, in an attempt to ensure the multipath cancelling, we get

$$\sqrt{(2h_A)^2 + d^2} - \sqrt{(2h_B)^2 + d^2} = \frac{\lambda}{2}. \tag{5.6}$$

Any pair of coordinates (h_A, h_B) that obeys Eq. 5.6 is therefore suitable for our purposes.

Finally, the separation distance design methodology is illustrated in Fig. 5.3. From this illustration, one can note that the multipath component arrives late at the receiver for a small distance d_x. In this case, if the transmitted signal is a time-domain pulse, the receiver will note two versions of this pulse arriving there in different instants and with no overlapping. Therefore, the further gain estimates will not be affected. Nevertheless, the probability of an undesirable mutual coupling between the antennas increases since they are close to the near field region. Opposite behaviors can be noted if the separation distance increases to d_y. For our purposes, the optimal solution is the minimum distance that assures the far field premise, which is necessary for the gain calculation via Friis equation, Eq. 2.14. Therefore, the main goal becomes to estimate the boundary between the near and far fields regions for a given AUT.

This calculation can be performed analytically, numerically or empirically. Some analytical expressions can be found in the antenna literature (37), but their validity can be restricted. For a more accurate calculation that takes the AUT particularities (geometry, materials etc) into account, electromagnetic simulations can be an option.

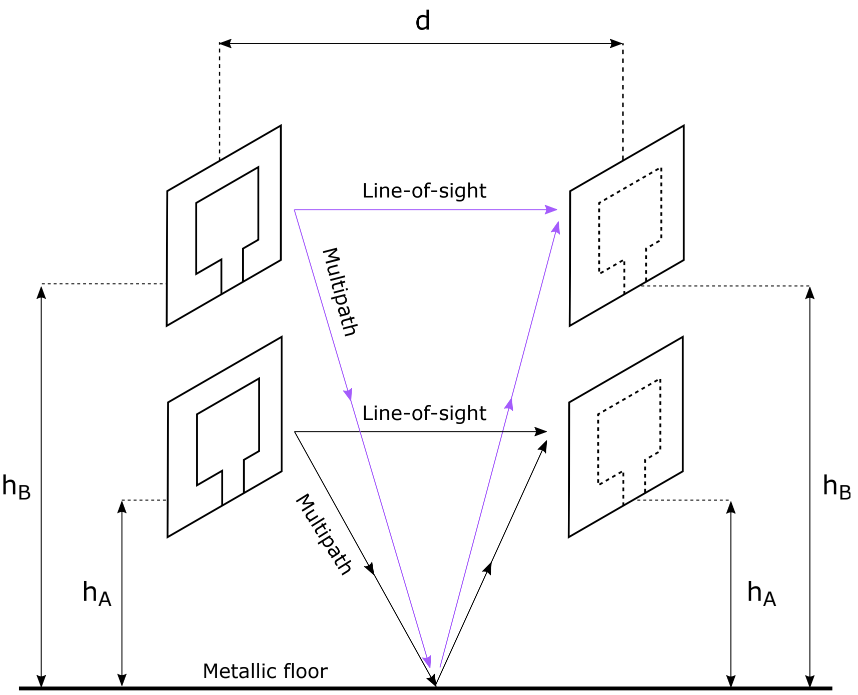

Figure 5.2 – Illustration of the multipath cancelling methodology based on vertical shifts, valid for reflections on the floor. These shifts allow one to control the phase of the reflected signals at the receiver. After a series of measurements, we expect that the average multipath contribution will vanish.

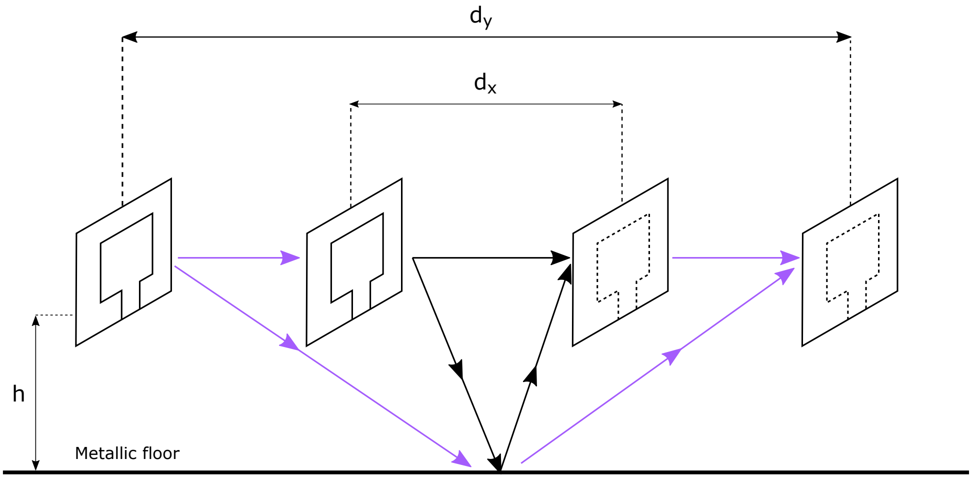

Figure 5.3 – Illustration of the trade-off involved in the separation distance design. If it is short (d_x), the multipath component arrives much later than the line-of-sight at the receiver and consequently the time-domain pulse distortion is minimized. However, the probability of falling into the near field region is increased. The opposite effects are verified if we increase the distance to d_y.

Since commercial software are usually capable of generating S-Parameters from geometric models, it is possible to obtain S_{12} *versus* frequency curves for each distance. With this information, one can evaluate Eq. 2.14, which provides the gain estimate via Friis equation. Simultaneously, it is possible to configure the software to provide the antenna input and output power levels, allowing the gain calculation via Eq. 2.12. The difference between these two estimates is a measure of the far field proximity. This is because when the difference starts to vanish, it means that the gain estimate via Friis equation provides the same results as the theoretical definition, ensuring thus the far field condition. Some preliminary results of this methodology were published by this author in (47). Nevertheless, these results presume that an antenna computational model with its geometry and materials properties is available. This is usually the case during the design phase but not when the product is acquired in the market. In order not to limit the use of the proposed methodology, we adopt here a more empirical procedure. Hence, we simply monitor the S_{12} *versus* frequency curves provided by the VNA while we move one antenna away from the other one. If this curve does not change significantly, we consider that the distance ensures far field.

5.1.2 Summary of the DAE-1 technique

The DAE-1 technique can be summarized as follows.

- **Step 1**: define the distance between the antenna pair, d, according to the far field *versus* multipath trade-off illustrated in Fig. 5.3. If the complexity of the antenna geometry is high, one can consider the use of electromagnetic simulations to more precisely identify the boundaries between the near and far field regions.
- **Step 2**: define two heights, h_A and h_B, using Eq. 5.6 and the wavelength, λ, that corresponds to the antenna central frequency.
- **Step 3**: define a rotation angle. The smaller the angle is, the more you explore the spatial distributions of EMI and multipath and therefore the higher are the probabilities of minimizing such contributions. Nevertheless, a fine spatial resolution increases the total test time. Furthermore, the physical dimensions of the test site can be a constraint, limiting thus the set of possible rotation angles.
- **Step 4**: define the total number of experimental runs, N. In general, the higher this number is, the more precise are the S_{12} estimates. However, a high N can significantly increase the total test time.
- **Step 5**: apply d, h_A, h_B, the rotation angle and N to the arrangements illustrated in Figs. 5.1 and 5.2 to obtain a S_{12} estimate.
- **Step 6**: use Eq. 2.14 to calculate the antenna gain using the S_{12} estimate.

5.1.3 ASP-1

The ASP-1 technique can be summarized through the block diagram shown in Fig. 5.4. In this block representation, one can identify four sub-structures: (i) adaptive filter, (ii) time gating, (iii) PSO and (iv) window design. In order to facilitate the further descriptions, from now on we will consider (i) and (ii) as the *main algorithms* while (iii) and (iv) will be the *auxiliary algorithms*. The first set is responsible for the filtering of a given noisy signal, while the second one provides the AF and TG blocks with optimal parameters.

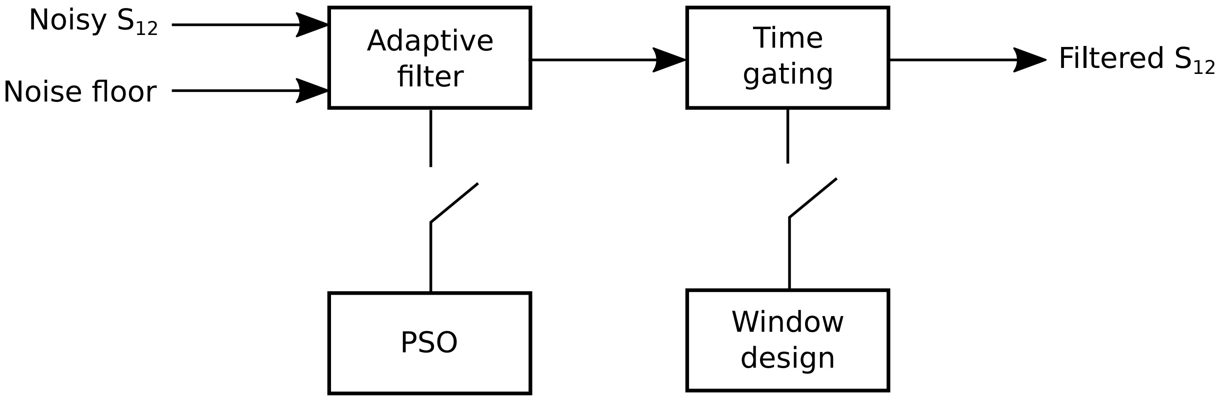

Figure 5.4 – Switch-based illustration of the ASP-1 mechanism. Above, the main algorithms: a series connection of an adaptive filter and time gating. Below, the auxiliary algorithms as the ones that generate optimal filters parameters.

Before detailing the mentioned algorithms, we demonstrate the way the structure illustrated in Fig. 5.4 works. This structure operates in two distinct modes: training and test. These different operating modes require in turn two sets of measurement data. The main algorithms are used in both stages while the auxiliary algorithms are only used in the training phase.

According to Fig. 5.4, the interaction between the main and auxiliary algorithms can be seen as a normally open switch. To start the process, we close the switches and we then use the training signals to feed the structure. During this stage, we are not necessarily interested in the filtered signal but in the parameters generated by the PSO and window design blocks. These parameters correspond to optimal (μ, L) AF parameters as well as the shape and time interval of a time-domain window used in the TG stage. All these parameters will be useful in the next stage of this process.

Now, the switches return to their initial open state. This means no communication between the main and auxiliary algorithms. The parameters generated by the PSO and window design blocks in the previous stage are then used to configure the AF and TG filters. Finally, the test signals are used to feed the structure whose input contains the filtered waveform that we look for. This process is illustrated in Fig. 5.5.

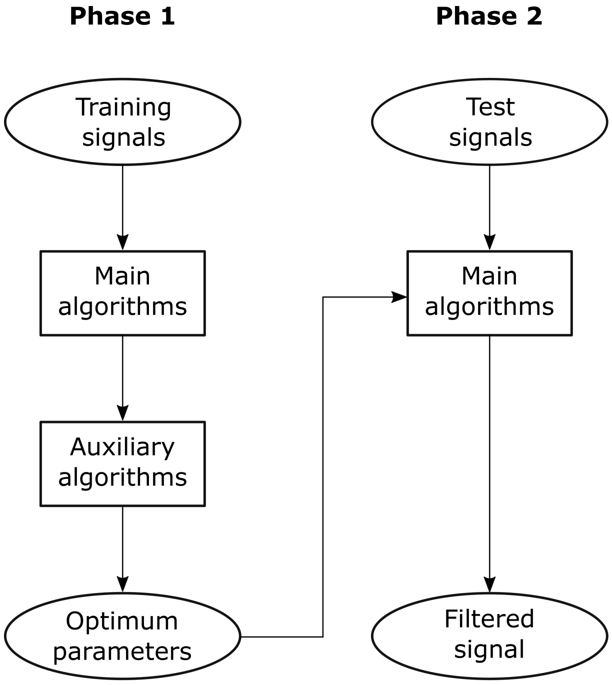

Figure 5.5 – Two processes involved in the application of the ASP-1 algorithm: training (Phase 1) and testing (Phase 2). The first stage generates optimum parameters for the AF and TG filters. The second-stage output is the filtered signal.

In the following sub-sections, we detail Stages 1 and 2. The first one refers to the AF-PSO set, while the second one encompasses the TG and window design blocks. Stage 1 is responsible for minimizing EMI, while Stage 2 shall reduce the multipath and thermal noise effects. This is based on the AF and TG limitations for the antenna calibration problem discussed in Section 4.4.

5.1.3.1 Stage 1

As already discussed in Section 4.3, the AF is sensitive to the parameters choice. Such a choice is in turn usually based on empirical knowledge. Therefore, if the final user of our tool has no or little experience with the signal processing field, a significant filter performance degradation can happen. We then assume a worst-case scenario, where the final user has no clue about a suitable choice for (μ, L). In the current investigation, this pair of coordinates represents a combination of a NLMS filter step-size and length.

Based on this worst-case scenario, we consider that population-based optimization techniques tend to be more efficient than gradient-based ones. Since there is no clue about the optimum solution location within the (μ, L) plane, all regions of the search space are equally probable to contain it. Therefore, we might evaluate a great amount of candidate solutions per iteration.

In a recent publication, Sheng (9) proposes an AF parameter tuning approach based on the particle swarm optimization (PSO). They developed a signal processing tool that improves the reliability of open space measurements in the context of an EMC test called *radiated emissions*. In fact, the PSO technique has been applied to AF problems in a variety of ways (73; 74; 75). During the current investigation, we consider the AF tuning described by Sheng *et al* but we propose an important modification, to be further detailed.

The PSO is a nature-inspired evolutionary optimization algorithm. Its mechanism is based on the social behavior of animals such as birds and fish in their search for food (76; 77). This sort of dynamics is guided by the individual and group empirical knowledge within a swarm. Based on the way these animals define a path towards the food source, the PSO is conceived to gradually converge to an optimum solution.

In this work, we define the (μ, L) plane as the PSO search space. To start the process, we first define some boundaries in order to ensure that the NLMS algorithm (which is a gradient-based optimization algorithm) will converge[1]. Then, we create a set of candidate solutions (each of them is a *particle*) with random positions in the (μ, L) plane, forming the first *swarm*. Then, we apply the PSO movement equations (described in (76; 77)) which change their positions and create the second swarm. This process continues in an iterative way until convergence is reached. Each iteration is also known as a *generation*.

An important aspect of our PSO-based analyses is the strategy to define which particles shall move more than the others when a new generation is being created. It is intuitive that the particles which are closer to the optimum solution shall have their velocities decreased and vice-versa. But how to define if a particle is close enough to the global optimum if we do not know the global optimum? The answer is: by making inferences through a *fitness function*. This function is usually proportional to the distance from the global optimum, meaning that we usually want to minimize it.

In terms of AF tuning problems, the fitness shall be a certain function of the filter output, also known as the error signal, $e[n]$. (9), for example, proposes the mean squared error. Since the MSE is a measure of a signal energy, the solution proposed by these authors prioritize low-energy particles. This is a good approach when one can ensure that the filter only extracts undesirable contributions from a noisy signal, while keeping its useful part. In this case, the most suitable filter is the one that reduces more the energy levels of the resulting signal. However, during this investigation, we found a flaw on this methodology. To check that, we ran a MSE-based PSO-AF routine fed by a set of noisy S_{12} measurements. From the optimal solutions provided by such an algorithm, we realized that not only the noise was partially eliminated but also the useful signals in most cases.

---

[1] To define these boundaries, we use these known step-size limits: $\lambda > 0$ and $\lambda < 1/(\sigma_u^2 \times L)$, with σ_u^2 being the noise floor variance (power) and L the filter length. On the other hand, the limits for L are defined in a more empirical way. To do so, we apply a fast Fourier transform (FFT) to the weights vector and we analyse the resulting filter transfer function. Based on a previous knowledge about the useful signal shape, we conclude if a certain L range is suitable or not.

This led us to the formulation of a different approach.

In this work, we propose the following fitness function

$$f = \rho(e[n], u[n]) \tag{5.7}$$

where $u[n]$ is the noise floor measurement and $\rho(.,.)$ is the Pearson correlation coefficient, defined as

$$\rho(X, Y) = cov(X, Y)/(\rho_X \rho_Y) \tag{5.8}$$

for two random variables X and Y from their covariance, $cov(X, Y)$, and standard deviations, ρ_X and ρ_Y (56). To estimate $\rho(X, Y)$, we run the NLMS algorithm and wait for convergence. Then, we store the $e[n]$ and $u[n]$ signals as available at the last iteration. Finally, we extract the covariance and standard deviations from the signals samples in the time domain.

Our idea is to indirectly minimize $e[n]$ (and not directly, as proposed by (9)), by means of its correlation with the noise floor. By doing so, we expect to create a search mechanism that minimizes exclusively the noise influence without compromising the useful signal.

5.1.3.2 Stage 2

In the second stage, TG is used to minimize multipath and thermal noise, considering that the EMI was previously attenuated by the adaptive filter. The novelty here is the presence of an auxiliary routine for automatically setting the location and duration of the time domain window. It can be seen as an alternative to the traditional manual adjustment usually available in VNAs. To do so, it first extracts the signal envelope. After that, the routine identifies the peak value, from which it calculates four critical points, corresponding to 5% and 40% of amplitude decaying. These specific samples of the envelope function define: (i) the beginning and (ii) the end of the window rise time, as well as the beginning (iii) and (iv) the end of its fall time.

From (i), (ii), (iii) and (iv), we create a shape that approximately fits to the time-domain responses of AUT1, AUT2 and AUT3. To do so, we apply the rising portion of a Blackman function between (i) and (ii). Between (ii) and (iii), we use the unitary portion of the rectangular window and, finally, between (iii) and (iv), we apply the falling portion of the Hamming window. For a given input signal, we define (i) and (iv) as the time instants correspondent to 5% of the peak value and (ii) and (iii) as 40%.

The use of more than one mathematical function, combined with two reference values (5% and 40% of amplitude decaying), result in a hybrid window. By doing so, we attempt to mimic the most recurrent rise and fall times observed in the antenna signatures analysed so far. Evidently, this design methodology do not fit perfectly to all antenna responses, since each of them has a particular behavior, as already discussed in Section 3.2.2. Nevertheless, this seems to be a good compromise based on the average behavior of AUT1, AUT2 and AUT3. Therefore, this window design approach has the potential to cover different types of antennas. Figure 5.6 illustrates an automatically-generated window applied to AUT3, after the first stage (AF).

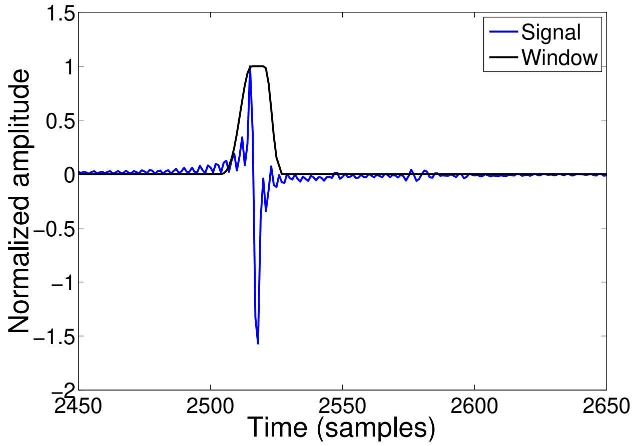

Figure 5.6 – Automatic TG window applied to the AUT3 S_{12} signal in the time domain, after the first stage (AF).

5.1.4 Metrics for performance evaluation

In order to evaluate the DAE-1 and ASP-1 performances, we first organize the measurement data coming from the experiments described in Section 2.3.2. The signals measured at Lab1 and Lab2 are processed by the two mentioned techniques. Then, their filtered versions are compared with the chamber measurements, obtained at Cha1 and Cha2. Finally, a two-stage benchmark analysis is carried out having other state-of-the-art techniques as comparison metrics.

In a first moment, we compare the retrieved AUT1 gain curves obtained using the DAE-1 and ASP-1 techniques with that obtained using the methodology proposed by Froes in (22), called here DAE-2. We analyse the ability of these techniques to improve the correlation of a noisy gain curve with that obtained in an anechoic environment.

In a second approach, we no longer consider the DAE-1 technique. Instead, we apply ASP-1 to the noisy AUT1, AUT2 and AUT3 gain curves. However, the PSO algorithm is configured in two different ways. First, we set its fitness function as proposed by (9). Then, we change it by using the proposed fitness function defined by Eq. 5.7. Finally, we proceed with the chamber curves comparisons.

To configure the PSO algorithm, we first set the initial velocities of all particles with zeros. Then, we set the PSO parameters as follows:

- acceleration parameters = 2;
- swarm size = 50;
- sub-swarms size = 5;
- minimum fitness = 1×10^{-8};
- maximum number of generations = 100;
- decreasing inertial weight = $0.9 - (0.4/100) * g[n]$;
- increasing inertial weight = $0.5 + (0.4/100) * g[n]$,

with $g[n]$ being the index of the n^{th} generation ($1 \leq n \leq 100$) and $0.01 \leq \mu \leq 0.1$, $10 \leq L \leq 50$ the limits of the search space.

Among the above-mentioned parameters, it is important to highlight the inertial weight. This parameter comes from a direct analogy with mechanics. Therefore, it controls the impact of the imposed velocity change over a given particle. This impact is reduced when the inertial weight is high and vice-versa. (77) define a number of different strategies to control the intertial weights along the generations. In our investigation, we define two linear models, with decreasing and increasing profiles. The first one allows a good exploitation of the search space, avoiding premature convergences to local minima but requires more iterations. The second one allows faster convergence rates but with higher probability of falling into a local minimum. Besides this, we use an approach based on sub-swarms, as described by (77), in order to increase diversity during the search for the optimum solution. We do this in order to avoid the mentioned premature convergences to local minimum.

Finally, it is important to stress that the proposed PSO benchmark is based on average behaviors of the two fitness functions considered here. This is needed because the PSO velocity equations contain random terms (76; 77). In other words, the PSO is a stochastic optimization technique and therefore the optimal solutions might change a bit if we run it more than once (even if we keep the input data constant). Based on this, we run it 10 times with the MSE fitness and 10 times with the proposed function.

5.1.5 Summary of the ASP-1 technique

The ASP-1 technique can be summarized through the pseudocode below. It can be used as a guide for computational implementations. However, it does not specify values for the PSO parameters – see lines 2 and 3. By doing so, we allow the programmer to define its own search strategy within the (μ, L) plane. Nevertheless, one can simply use the

Algorithm 1 ASP-1

Input: two pairs of S_{12} and noise floor measurements – one for training and one for tests
Output: antenna gain estimate

```
 1: Apply an inverse Fourier transform to the measured signals
 2: Define the PSO convergence parameters: the minimum fitness, $f^*$, and the maximum
    number of iterations, Counter$_{max}$
 3: Define the PSO movement parameters
 4: Create the first PSO swarm with $M$ random $(\mu, L)$ combinations
 5: $Counter \leftarrow 0$
 6: $Counter \leftarrow Counter + 1$
 7: if Counter>1 then
 8:     Generate a new swarm using the PSO movement equations configured with the
        parameters defined in line 3
 9: for $iteration = 1, 2, \dots M$ do
10:     Run the NLMS iterative process from Eq. 4.2 using the training signals and get $e[n]$
11:     Apply $e[n]$ to Eq. 5.7 and obtain the fitness value
12: Store the best particle of the swarm, $(\mu^{pbest}, L^{pbest})$, its fitness, $f^{pbest}$, and the resulting
    error signal, $e^{pbest}[n]$
13: if $abs\{f^{pbest}\} < abs\{f^*\}$ || Counter == Counter$_{max}$ then
14:     Calculate the envelope function of $e^{pbest}[n]$
15:     Identify the envelope peak
16:     Store four time indexes, $n$, that correspond to 95% and 60% of amplitude decaying:
        $(t_1, t_4)$ and $(t_2, t_3)$, respectively.
17:     $L_{rise} \leftarrow t_2 - t_1$
18:     $L_{fall} \leftarrow t_4 - t_3$
19:     Create a Blackman and a Hamming windows
20:     Store the first $L_{rise}$ samples of the Blackman function and delete the others
21:     Store the last $L_{fall}$ samples of the Blackman function and delete the others
22:     Create a window function and initialize it with ones
23:     Fill the $L_{rise}$ first samples with the Blackman function
24:     Fill the $L_{fall}$ last samples with the Hamming function
25:     Store the resulting window function
26:     Load the test data
27:     Run the NLMS iterative process from Eq. 4.2 using the test data and get $e[n]$
28:     Multiply $e[n]$ by the resulting window function from line 25
29:     Store the resulting signal in $\widehat{S_{12}}$
30:     Apply $\widehat{S_{12}}$ to Eq. 2.14 and obtain the antenna gain estimate
31:     End of the process
32: else
33:     Return to line 6
```

parameters which were previosly defined in Section 5.1.4, follow the various suggestions found in the literature (76; 77) or even in online forums.

Furthermore, the Algorithm 1 does not contain the PSO movement equations – *i.e.* those used to generate the swarms (with the exception of the first one, which is random). Nevertheless, one can easily find these equations in any PSO basic reference (76; 77).

5.2 IEMI problem

5.2.1 ASP-2

5.2.1.1 General aspects

As already discussed in Section 3.3.2, we generate GSM-R and jamming signals samples with a virtual test setup. Furthermore, we use the virtual environment to apply the ASP-2 routine and evaluate its performance in terms of BER reduction.

During this investigation, we calculate the BER between the transmitted and received digital data under three circumstances: (i) without jamming, (ii) with jamming but without the filter and (iii) with jamming and filter. By doing so, we can evaluate both the jamming effects and the filters' performances under different SJR scenarios (see the switching scheme illustrated in Fig. 3.14).

The basic elements of the ASP-2 structure are the AF and data reuse (DR) techniques. DR is usually used to accelerate the convergence of the AF. However, we highlight that the DR approach we use is not exactly the same ones reported on the literature.

In (78), the authors define two basic ways of implementing DR. The first approach is based on a sub-iteration scheme where the AF iterative process, Eq. 4.2, is modified. In this case, a second index is associated to the filter impulse response vector, $\mathbf{h}[n]$, which becomes $\mathbf{h}_k[n]$. The new index k ranges from 1 to K, where K is the number of times the input signals, $\{u_n, s[n] + j_1[n]\}$, are reused. The u_n signal is called the *regressor vector*. It consists on the current and L past values of the $j_2[n]$ signal, *i.e.* $u_n = \{j_2[n], j_2[n-1], \ldots, j_2[n-L-1]\}$ (L being the filter order or length). The iterative process then becomes

$$\mathbf{h}_k[n] = \mathbf{h}_{k-1}[n-1] - \mu\widehat{\nabla}\mathbb{E}\{e_{k-1}[n]^2\}, \tag{5.9}$$

where $\widehat{\nabla}\mathbb{E}\{e_{k-1}[n]^2\} = u_n e_{k-1}[n]$ is the gradient estimator and $e_{k-1}[n] = (s[n] + j_1[n]) - u_n\mathbf{h}_{k-1}[n-1]$ is the error signal. The first and last values of this sub-iteration process,

$\mathbf{h}_0[n]$ and $\mathbf{h}_K[n]$, are related to the main iteration process from Eq. 4.2 through

$$\mathbf{h}_0[n] = \mathbf{h}[n-1] \tag{5.10}$$

$$\mathbf{h}[n] = \mathbf{h}_K[n-1]. \tag{5.11}$$

In the second approach (78), on the other hand, one stores the current and past versions of the regressor vector, u_n, creating thus a $K \times L$ *regressor matrix*, $U_n = \{u_n^T, u_{n-1}^T, \ldots, u_{n-K+1}^T\}$ where $(.)^T$ means transposition and a $K \times 1$ measurements vector, $d_n = \{d[n], d[n-1], \ldots, d[n-K+1]\}$ where $d[n] \equiv s[n] + j_1[n]$. The iterative process then becomes

$$\mathbf{h}[n] = \mathbf{h}[n-1] - \mu U_n^H e[n], \tag{5.12}$$

where $(.)^H$ means conjugate transpose and $e[n] = d_n - U_n\mathbf{h}[n-1]$.

In this work, however, we adopt a simpler procedure. First, we create K identical replicates of both $s[n] + j_1[n]$ and $j_2[n]$ signals. Then, we create two new signals. One of them consists on $s[n] + j_1[n]$ followed by its K replicates, all concatenated in series over the time domain. The second one is created using the same procedure but using the $j_2[n]$ signal instead of $s[n] + j_1[n]$. In terms of number of samples, we increase K times the initial amount. Then we run the iterative process from Eq. 4.2 having these modified signals as inputs.

We justify this methodology based on the fact that the iterative process from Eq. 4.2 may, in some situations, stop before the filter coefficients have converged to their optimum values. In other words: depending on the available number of the signals samples, it is possible that the filter learning process is stopped in its transient period. So, by enlarging these signals, we expect to ensure that the learning process will have reached steady-state when the process is stopped.

5.2.1.2 The adaptive line enhancer as a candidate tool

According to the exposition made in Chapter 4, the ANC filter performance is sensitive to some characteristics of the $j_2[n]$ signal. First, it must be highly correlated to $j_1[n]$. At the same time, it must be free from $s[n]$ contributions. Also, a more fundamental question may arise: is $j_2[n]$ available for measurements? When it comes to a real-time IEMI filtering process within a railway environment, the answer is no. It is not possible to obtain an isolated measurement of the jamming signal, since it is always superimposed to the GSM-R communications. Therefore, it is necessary to search for signal processing tools that do not require this measurement to be done.

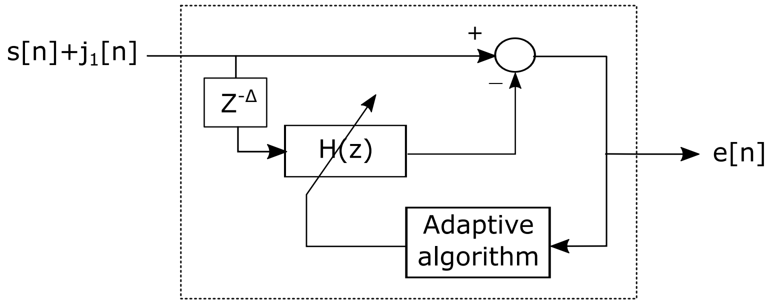

Figure 5.7 – ALE basic structure. In opposition to the ANC filter, this structure only requires 1 input (the noisy measurement, $s[n] + j_1[n]$). Thanks to a decorrelation block, $z^{-\Delta}$, it is possible to generate a noise sample at the $H(z)$ input and thus mimic the ANC operation.

Given the above mentioned set of requirements, we consider the adaptive line enhancer (ALE) as a candidate tool. Its basic structure – to be later on detailed – is illustrated in Fig. 5.7. Since the ALE principles were first published in the mid-1970s (62), a number of reports on its use emerged. Recent examples include automotive (79), biomedical (80) and audio (81) engineering, among many others.

By comparing the block diagrams in Figs. 4.4 and 5.7, it is possible to identify that the difference between the ANC and ALE configurations resides on the number of inputs. While the ANC filter requires two inputs (the noisy signal, $s[n] + j_1[n]$, and a noise floor sample, $j_2[n]$), its ALE version only requires the noisy signal as input. This is possible thanks to the addition of a delay structure, $z^{-\Delta}$, between the input and the $H(z)$ block. The delay block contains Δ, a critical parameter which is also known as the *decorrelation parameter*.

A key aspect regarding the ALE filter performance is then the design of the Δ parameter. To understand the role played by this parameter, let us consider the $z^{-\Delta}$ block in Fig. 5.7. Its input signal is $s[n]+j_1[n]$. Let us keep the same notation from Section 4.3.1, according to which $s[n]$ and $j_1[n]$ are the useful and spurious portions of the measured signal, respectively. Now, let us consider that $s^{\Delta}[n] + j_1^{\Delta}[n]$ is the output signal of the $z^{-\Delta}$ block. The difference between $s[n] + j_1[n]$ and $s^{\Delta}[n] + j_1^{\Delta}[n]$ is a time delay of Δ samples. Then, if Δ is chosen in such a way as to produce a 360° lag (or any integer multiple) between $j_1[n]$ and $j_1^{\Delta}[n]$, the output of the summation block in Fig. 5.7 becomes $e[n] = s[n] + j_1[n] - j_1^{\Delta}[n] \approx s[n]$. In this scenario, the filter transfer function, $H(z)$, tends to select only $j_1[n]$ and to reject $s[n]$[2]. So, the error signal becomes a good estimator for $s[n]$ if Δ is well designed – *i.e.* $\widehat{s}[n] = e[n]$ in this case. We call this the **Configuration A**.

---

[2] To show that, let us recall Eq. 4.2, where $\widehat{\nabla}\mathbb{E}\{e^2[n]\} = \mathbf{u_n}e[n]$. In the mentioned scenario, $e[n] = s[n]$ and $\mathbf{u_n}$ is the regressor vector associated with the output signal of the delay block, $s^{\Delta}[n] + j_1^{\Delta}[n]$. Since there is no correlation between the GSM-R and jamming signals, *i.e.* between $s[n]$ and $j_1[n]$, the magnitude of the resulting gradient vector is essentially a function of $s[n]$. Therefore, the only solution to minimize the MSE is to reduce the power of $s[n]$.

However, the ALE filter is designed to do the opposite in most cases, *i.e.* Δ is chosen in such a way as to produce a 360° lag (or any integer multiple) between $s[n]$ and $s^{\Delta}[n]$ and therefore the filter transfer function, $H(z)$, tends to select only $s[n]$ and to reject $j_1[n]$. So, the error signal becomes $e[n] = s[n] + j_1[n] - s^{\Delta}[n] \approx j_1[n]$. Therefore, the filtered signal cannot be taken at the summation block output anymore – in opposition to what we did in the antenna calibration problem, where the ANC configuration was used. Instead, we read the output of the $H(z)$ block, *i.e.* $\widehat{s}[n] = s^{\Delta}[n]$. We call this the **Configuration B**.

These two configurations are summarized in Table 5.1. It is clear in this table that the ALE filter separates the useful signal, $s[n]$, from the noise contribution, $j_1[n]$, producing a pair of estimates, $\widehat{s}[n]$ and $\widehat{j_1}[n]$. For the purposes of this investigation, we only need $\widehat{s}[n]$. According to Table 5.1, this waveform equals the error signal, $e[n]$, in Configuration A. On the other hand, the filtered signal, $\widehat{s}[n]$, is taken at the output of the $H(z)$ block in Configuration B.

Table 5.1 – Two possible configurations of the ALE filter. The filtered waveform, $\widehat{s}[n]$, is the error signal in Configuration A while the same waveform is taken at the output of the $H(z)$ block in Configuration B.

Configuration	$H(z)$ output	Error signal
A	$\widehat{j_1}[n]$	$\widehat{s}[n]$
B	$\widehat{s}[n]$	$\widehat{j_1}[n]$

The most common way of using the ALE filter is based on the Configuration B. In the next sub-section, we show that, in this case, one may want to eliminate white background noise from a sine wave of unknown frequency. Nevertheless, we obtained better results using Configuration A when trying to eliminate jamming contributions in simulated GSM-R transmissions. Therefore, we adopt Configuration A in our analyses involving the IEMI case study.

5.2.1.3 Choosing Δ based on the autocorrelation function

In the last sub-section, we defined the $z^{-\Delta}$ block as the one that imposes a 360° shift to the $s[n]$ signal. Now, we show that this property is associated with an important characteristic of a measured signal: its autocorrelation function (ACF).

The ACF of a discrete-time signal, $x[n]$, can be defined as (82)

$$ACF[lags] = \frac{\sum(x[n] - \overline{x})(x[n + lags] - \overline{x})}{\sigma_x^2} \tag{5.13}$$

where $\sigma_x^2 = \sqrt{\sum(x[n] - \overline{x})^2 \sum(x[n + k] - \overline{x})^2}$ is the signal variance, $\overline{x}$ is its mean value and *lags* represents a null, positive or negative shift. In this work, we consider zero-mean signals. So, Eq. 5.13 reduces to

$$ACF[lags] = \frac{\sum(x[n]x[n + lags])}{\sigma_x^2}. \tag{5.14}$$

Equation 5.14 reveals a mathematical operation that consists of a series of inner products of a signal with itself, divided by the signal variance. By analysing the numerator in Eq. 5.14, one can identify a sliding inner product. While one version of the signal remains "still", the other one "slides" back and forth according to the lag. Every time the signal aligns with itself, an increase on the autocorrelation function is noted. This event will happen for all Δ values whose corresponding phase lags are integer multiples of 360°. Therefore, if there is any periodic component present on a signal, then a series of peaks will be noted on its autocorrelation function. If no periodicity is present, then this will happen only once – when there is no lag between the signal and a copy of itself.

In its classical formulation, the ALE filter is used to identify sine waves with unknown frequencies in white background noise (62)[3]. In this formulation, the $H(z)$ block in Fig. 5.7 converges to a band-pass shape. Consequently, it selects the sinusoidal component, $s[n]$, of the measured signal while removing the white noise contributions, $j_1[n]$. For this scheme to work, it is necessary that $s[n]$ is aligned with its delayed version, $s^{\Delta}[n]$. Therefore, we must search for the location of peaks on the autocorrelation function of the measured signal. To better explain that, we separately analyse the sine wave and white noise autocorrelation functions.

Figure 5.8a contains two traces: the sine wave and white noise autocorrelation functions in black and gray, respectively. As expected, the white noise autocorrelation function has a single peak, which happens when there is no lag. On the other hand, the sine wave autocorrelation function is periodic – the linear decaying is due to the finite number of signal samples; this would not happen for a theoretical sine wave, which has an infinite number of samples. Another view of this graph is available in Fig. 5.8b. This figure restricts the lag domain to the vicinity of its central point.

In order to obtain a delayed version of the sine wave, $s^{\Delta}[n]$, that is 360° out of phase with $s[n]$, we just need to search for the positive peaks of the black trace in Fig. 5.8b. The minimal lag that ensures this condition and, at the same time, prevents any undesirable synchronism between $j_1[n]$ and $j_1^{\Delta}[n]$ is the unitary lag, *i.e.* $\Delta = 1$. In Fig. 5.8b, we use markers to show that such a delay can impose a significant decay over the

---

[3] The first mathematical models that describe the ALE filter behavior are based on ideal sine waves, which have infinite length in time and therefore present infinitesimal bandwidth. Practical signals, on the other hand, have finite length in time and therefore they have finite bandwidth. Further publications showed that the ALE filter can also work with such signals, but with a performance degradation (83). For example, Tsalaile (80) discusses the performance limits of ALE filters when dealing with certain biological signals.

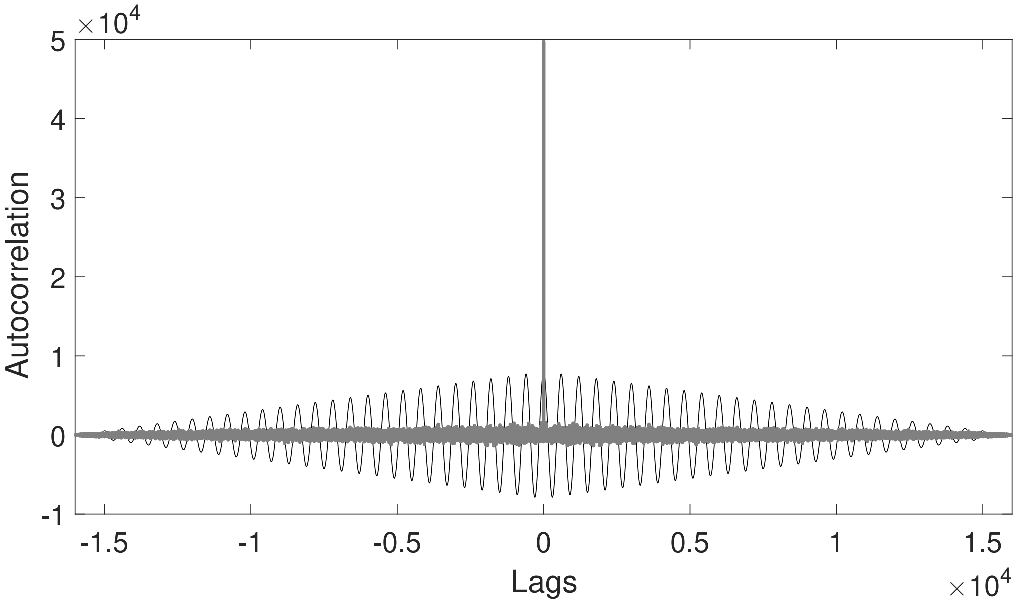

(a)

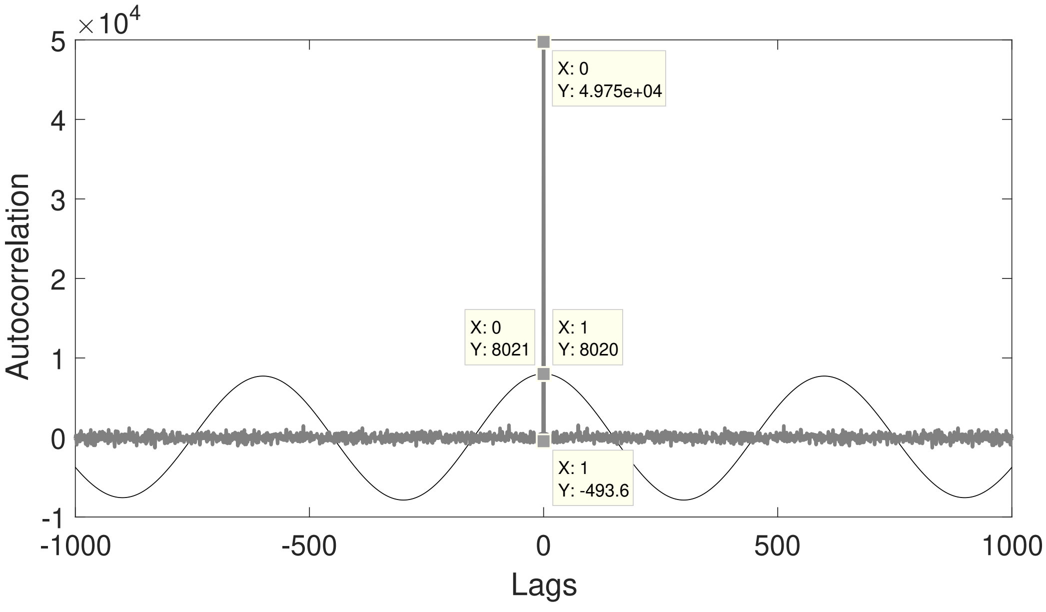

(b)

Figure 5.8 – Typical autocorrelation behaviors of white noise and sinusoidal signals, evidencing the discrepancy between the corresponding decaying times. Gray: white noise. Black: sine wave. (a) Entire lag domain. (b) Zoomed view.

white noise autocorrelation function (it changes from 4.975×10^4 when lags=0 to -493.6 when lags=1) while keeping the sine wave autocorrelation function essentially unchanged.

Now, we discuss the differences between the exposed scenario and the IEMI problem under investigation. Before proceeding, however, we define the following notation: $s[n]$ now represents the useful GSM-R signal while $j_1[n]$ represents the undesirable jamming contributions. Then, we create a simplified version of the GSM-R signal in MATLAB. It consists of digitally modulated random binary sequences based on the GMSK scheme (the same one used in actual GSM-R transmissions).

Figure 5.9a shows the GSM-R and the jamming signal autocorrelation functions. Since the GSM-R signal is based on a random bit sequence, its autocorrelation function has a relatively fast decaying, when compared to that of the jamming signal. However, although the latter presents a much slower decaying, it presents a periodic behavior. In Fig. 5.9b, it is possible to see the behavior of these functions in the neighborhood of lags=0. In this figure, we see that the GSM-R autocorrelation function presents high values within the $\pm 10^4$ lags range while the jamming signal autocorrelation function approaches zero. This represents a wide zone where the GSM-R signal is correlated with itself while the jamming signal is completely uncorrelated with itself – except for the neighborhood of lags=0, where the jamming signal autocorrelation values are high.

5.2.2 Summary of the ASP-2 technique

The ASP-2 technique can be summarized through the pseudocode below.

Algorithm 2 ASP-2

```
Input: a corrupted GSM-R signal in the time domain
Output: a filtered GSM-R signal in the time domain
1: Calculate the ACF using Eq. 5.14
2: Find its second peak, starting from lags=0, and store the corresponding lag
3: Store the lag in $\Delta$ and define $z^{-\Delta}$
4: Convolve the input signal with $z^{-\Delta}$
5: Run the NLMS iterative process from Eq. 4.2 using the input signal and the one
   obtained in line 4
6: Extract the error signal, $e[n]$
```

5.2.3 Performance analysis

In this work, we use the bit error rate, BER, as the main metric to evaluate the performance of the ASP-2 technique. The BER is a straightforward concept. In a digital communication system, there is a constant information exchange between equipment. Due to EMI, multipath and many other events, information can be partially lost. Evidently, wireless systems are designed to operate within a certain data loss margin. Nevertheless, if this effect is very intense, then the communication can be disrupted. In order to quantify this phenomenon, one can calculate the BER (31)

$$BER = (\text{number of incorrect bits})/(\text{total number of bits}). \tag{5.15}$$

To evaluate Eq. 5.15, one shall compare two finite-length binary sequences: the transmitted and received ones. Every time a 1 bit is wrongly interpreted as a 0 (and

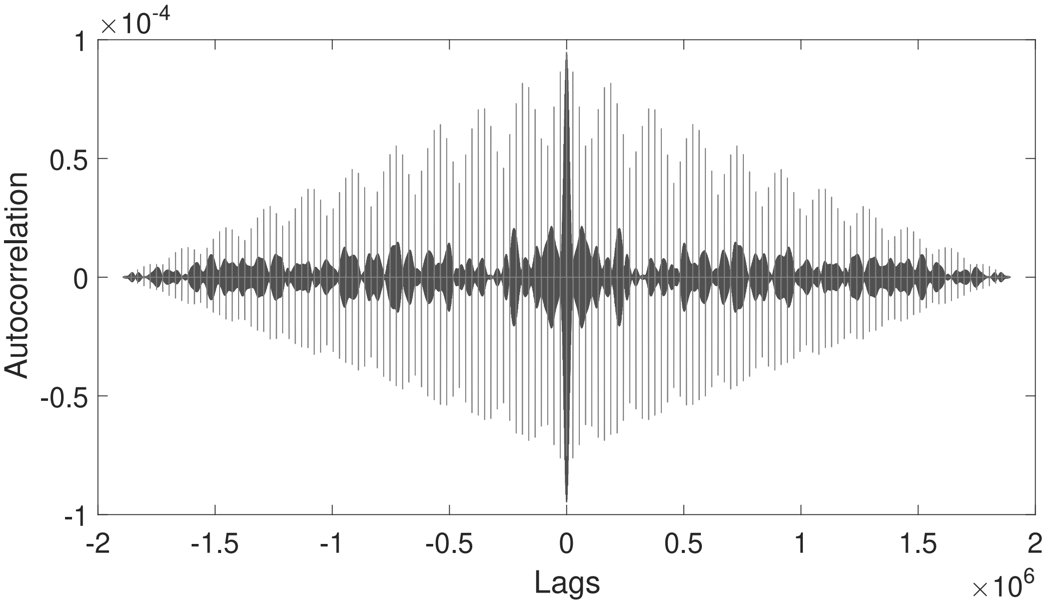

(a)

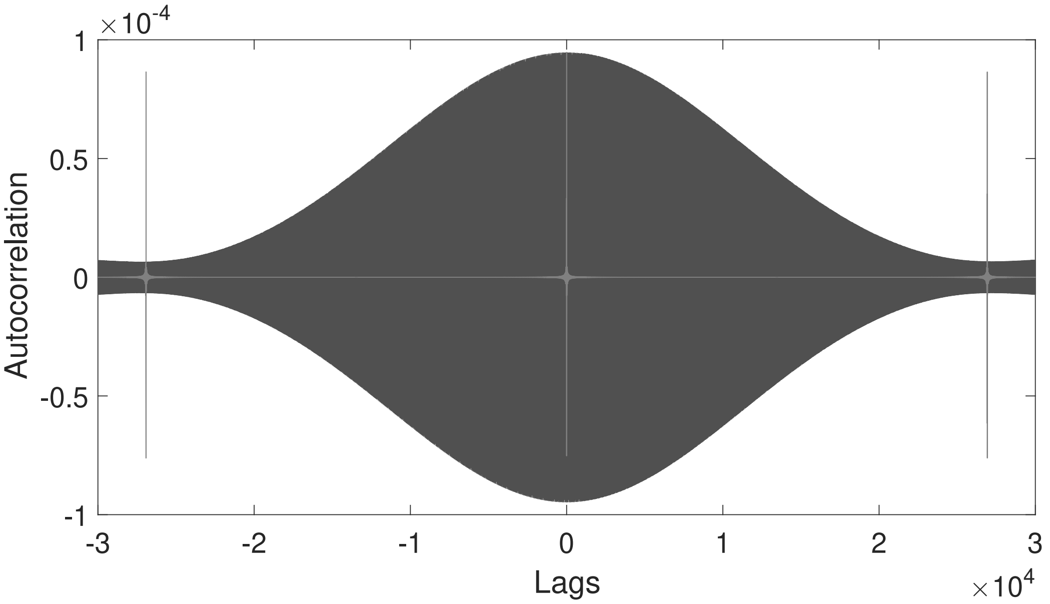

(b)

Figure 5.9 – Autocorrelation functions corresponding to the GSM-R and jamming signals (dark and light gray, respectively). The GSM-R signal results from a modulation process applied to a random bit sequence. (a) Entire lags domain. (b) Zoomed view focusing on the neighborhood of lags=0.

vice-versa), the BER is increased. If there is no data loss (an ideal channel), then the BER is zero. If all information is lost, then BER = 1. In a practical scenario, $0 < BER < 1$. Evidently, we can express the BER with percentage values by simply multiplying Eq. 5.15 by 100.

In this work, we are particularly interested in the AF ability to reduce the BER rates of a GSM-R system under IEMI. To do so, we evaluate Eq. 5.15 twice. First, we compare the reference bit sequence of the noiseless $s[n]$ signal with that obtained by demodulating its corrupted version, $s^{\Delta}[n] + j_1^{\Delta}[n]$. We call the resulting BER the BER_1. Then, in a second moment, we compare the same reference bit sequence with that of the filtered signal, $\widehat{s}[n]$.

5.3 Final considerations

In this chapter, we presented three new interference mitigation techniques: DAE-1, ASP-1 and ASP-2. With DAE-1, we propose special test setup arrangements, followed by replicated measurements. Among the proposed procedures, we highlight the design of optimal antennas heights. An analytic expression, Eq. 5.6, relating the antennas heights, h_A and h_B, with the distance between them, d and the wavelength, λ, was obtained. With this expression, we can carefully choose the antennas heights aiming to cancel multipath. It was obtained based on the two-ray propagation model.

The ASP-1 technique, on the other hand, requires neither replicated measurements nor test setup re-arrangements. Instead, it requires only four measurements: two sets of S_{12} and noise floor measurements, one for training and another one for filtering. Besides the filtering stages, we propose two auxiliary routines to automatically tune the filters with optimal parameters. Here, we highlight Eq. 5.7 as a new fitness function for the AF tuning approach proposed by (9).

Finally, we presented the ASP-2 technique in an attempt to solve the IEMI problem in GSM-R networks. It is based on the ALE filter. Therefore, it does not require a jamming signal sample during its operation. In this context, an important step is the definition of the decorrelation parameter. In this chapter, we showed how this parameter can be chosen based on the signals autocorrelation functions.

Chapter 6

Results

In this chapter, we show all the computational and experimental results obtained through the proposed methodologies. We start by showing the antenna gain retrieving process through DAE-1 and ASP-1. During this stage, we use a directive patch antenna (AUT1), an omnidirectional patch antenna (AUT2) and a directive horn antenna (AUT3). Tests are carried out in two ideal (Cha1 and Cha2) and two non-ideal (Lab1 and Lab2) test places. Results are mainly discussed via spectral analysis, but we also show a numerical correlation analysis. Later on, we explore the ASP-2 technique applied to the IEMI problem. In this context, we explore the filters performances based on computational simulations. Spectral analyses are then carried out, followed by the demodulation of both original, corrupted and filtered GSM-R signals. The demodulation allow us to demonstrate that the ASP-2 technique can reduce the BER levels of a GSM-R link under a jamming attack.

6.1 DAE-1 and ASP-1

Before discussing the results, we describe a few particularities of the test conditions. These special conditions were defined in an attempt to emphasize some phenomena and control the SNR. These actions allowed us to better evaluate the filters robustness and working ranges.

Concerning the VNA power level, we set it to -50 dBm in the experiments involving AUT1 and AUT2. Such a low power level allowed us to explore thermal noise effects. On the other hand, the power was increased up to -30 dBm when we were dealing with AUT3. Regarding the EMI, the test setups were brought to the vicinity of WiFi routers. In addition, we added extra levels of interference in some cases, increasing the original power up to 10 times. This is the same procedure that we used to evidence the TG flaws, as already discussed in Section 4.2. Now, we use it to evaluate the robustness of the ASP-1 technique. Finally, it is worthwhile to mention that the different directivities of the antennas under test (see Table 3.2) allowed us to evaluate the methodology under different multipath levels, as already discussed in Section 3.2.1, last paragraph.

Figure 6.1 shows a comparison between certain AUT1 gain curves within the 1.5-4.5 GHz band containing EMI (with no artificial increase in its original power). The violet and light gray plots result from ideal and non-ideal measurements (Cha1 and Lab1, respectively). The lab measurement presents an oscillatory behavior along the whole frequency range, which we attribute to the VNA thermal noise. In addition, the light gray curve evidences a narrow-band EMI near 2.4 GHz coming from the WiFi router located in the vicinity of the test setup.

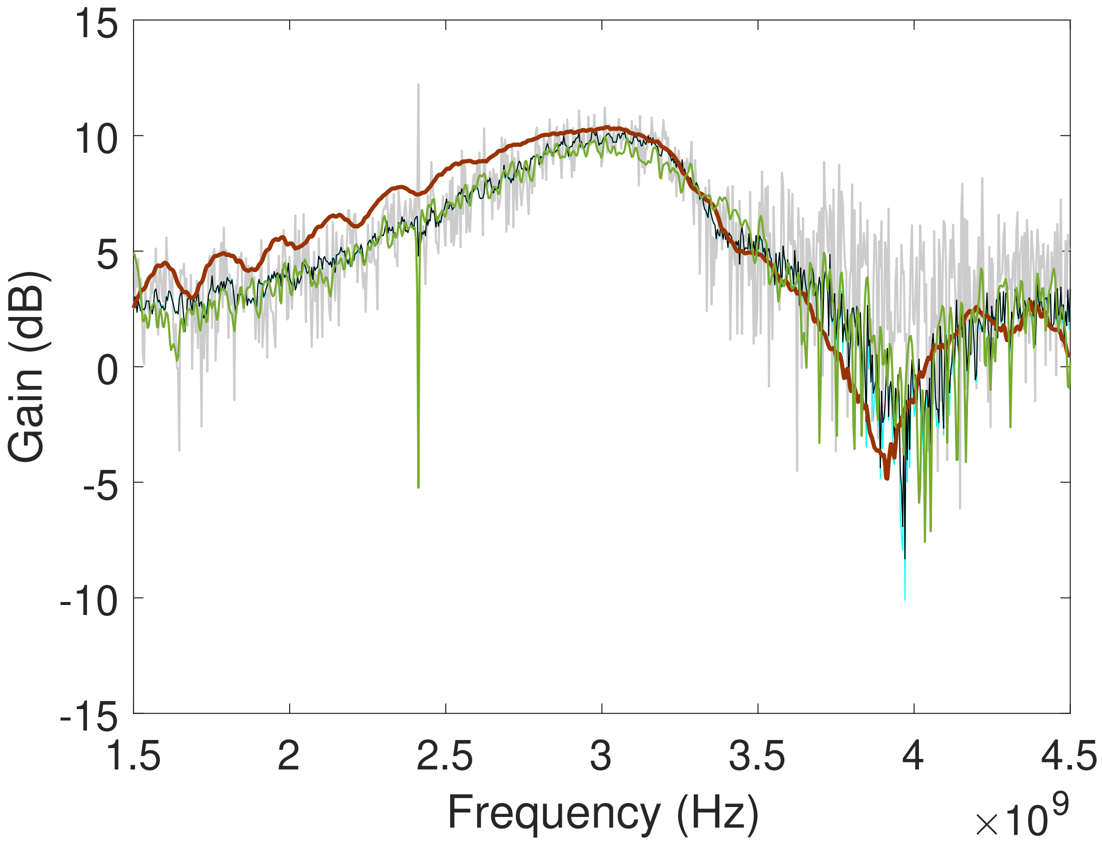

Figure 6.1 – AUT1 retrieved gain curves using the DAE-1 (light blue curve 🟦), DAE-2 (black curve ⬛) and ASP-1 (green curve 🟩) techniques. The light gray curve ⬜ represents the original gain curve, obtained in Lab1. The violet graph 🟪 represents the reference curve, obtained in Cha1.

The other curves from Fig. 6.1 reveal the performances of both the proposed and the state-of-the-art techniques. These behaviors are illustrated by the light blue, black and green curves, which represent DAE-1, DAE-2 and ASP-1. All approaches lead to a minimization of both the EMI and thermal noise. However, ASP-1 resulted in both useful signal and noise reductions in the EMI sub-band. Some possible causes include the measurement scheme that we adopted and the characteristics of the time-domain window used in the TG stage. The first one refers to the two test setups used to acquire S_{12} measurements: (i) the AUT/auxiliary antenna set (used to measure $s[n] + j_1[n]$) and (ii) the AUT/50Ω load set (used to measure $j_2[n]$). Since it can take a few minutes to change from one test setup to another one and the WiFi interference can change its characteristics according to the current traffic conditions (see Section 3.2.2.2), it is possible that $j_2[n]$ and $j_1[n]$ have different power levels. Consequently, if the power of the noise floor measurement, $j_2[n]$, is much higher than that of the actual noise present in the S_{12} signal, $j_1[n]$, then an excessive amount of power can be removed by the filter. The second possible cause is related to the time-domain window length. Since the window design algorithm is based on a trade-off involving different antenna responses (see the discussion in Section 5.1.3.2), it is possible that the window does not perfectly fit to the AUT1 response. So, if the window length is shorter than the antenna response, then the ASP-1 algorithm will remove more energy from the signal than it should.

Another important aspect of these graphs is a loss of performance around 4 GHz. We attribute this to the strong negative peaks shown in Fig. 4.1, which are completely random and therefore cannot be easily eliminated through AF or DAE-1/DAE-2.

The same analysis was carried out for AUT2, with results shown in Fig. 6.2. This graph reveals a similar performance for all techniques. However, the ASP-1 performance degradation was less intense. In the previous case, the gain deviation from the chamber measurement was about 10 dB around the interfering frequencies (see Fig. 6.1 in the vicinity of 2.4 GHz). Now, this deviation is around 5 dB.

The similarity between the filtered/non-filtered gain curves and the reference (chamber) graph can be calculated with the Pearson correlation coefficient. Table 6.1 summarizes the analyses conducted so far by means of correlation levels. In order to compute the performance gains of all methods, we calculate the differences between the values in the first line of Table 6.1 and the remaining ones (*e.g.* the DAE-1 performance gain is $0.9336 - 0.6689 = 0.2647$ for AUT1 or, equivalently, 26.47%).

The performance gain is evident for all the approaches, reaching approximately 27% (AUT1) and 30% (AUT2) with the DAE-based methods. These approaches had better performances when compared to ASP-1. Still, the signal processing approach increased in approximately 21% (AUT1) and 25% (AUT2) the correlation between the lab and chamber curves.

Table 6.1 – Correlation between the filtered/non-filtered and chamber gain curves.

AUT1		AUT2	
Approach	Correlation with Cha1 curve	Approach	Correlation with Cha1 curve
No filter	0.6689	No filter	0.6340
DAE-1	0.9336	DAE-1	0.9333
DAE-2	0.9350	DAE-2	0.9370
ASP-1	0.8731	ASP-1	0.8809

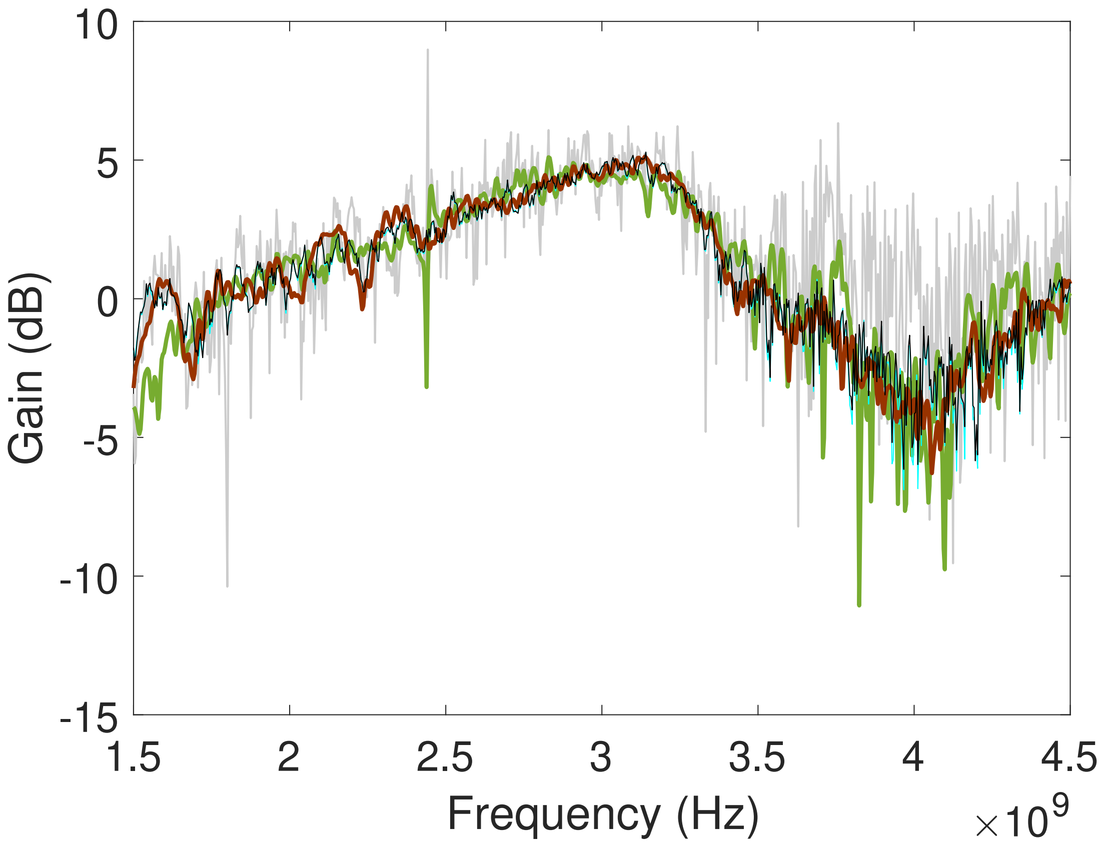

Figure 6.2 – AUT2 retrieved gain curves using the DAE-1 (light blue curve 🟦), DAE-2 (black curve ⬛) and ASP-1 (green curve 🟩) techniques. The light gray curve ⬜ represents the original gain curve, obtained in Lab1. The violet graph 🟪 represents the reference curve, obtained in Cha1.

After increasing 10 times the WiFi noise level, we evaluated the ASP-1 performance under two different configurations. The first one uses the PSO with the MSE fitness, while the second one employs the proposed fitness function given by Eq. 5.7. Table 6.2 summarizes the resulting optimal (μ, L) parameters for AUT1, AUT2 and AUT3. The filtering results obtained from the 6 configurations of Table 6.2 are shown in Figs. 6.3-6.5 through gain curves. These figures contain the reference chamber measurement, the noisy signal and the outputs from each stage of the ASP-1 structure.

Table 6.2 – (μ, L) parameters obtained through PSO with different fitness functions.

Antenna	MSE fitness	Proposed fitness
AUT1	(0.1,49)	(0.0456,27)
AUT2	(0.1,50)	(0.01,48)
AUT3	(0.1,47)	(0.0151,13)

Figure 6.3 presents the filtering results concerning the directive AUT1 antenna. A comparison between Figs. 6.3a and 6.3b reveals that the proposed fitness leads to a less smooth gain reconstitution than that obtained with the MSE function. However, it results

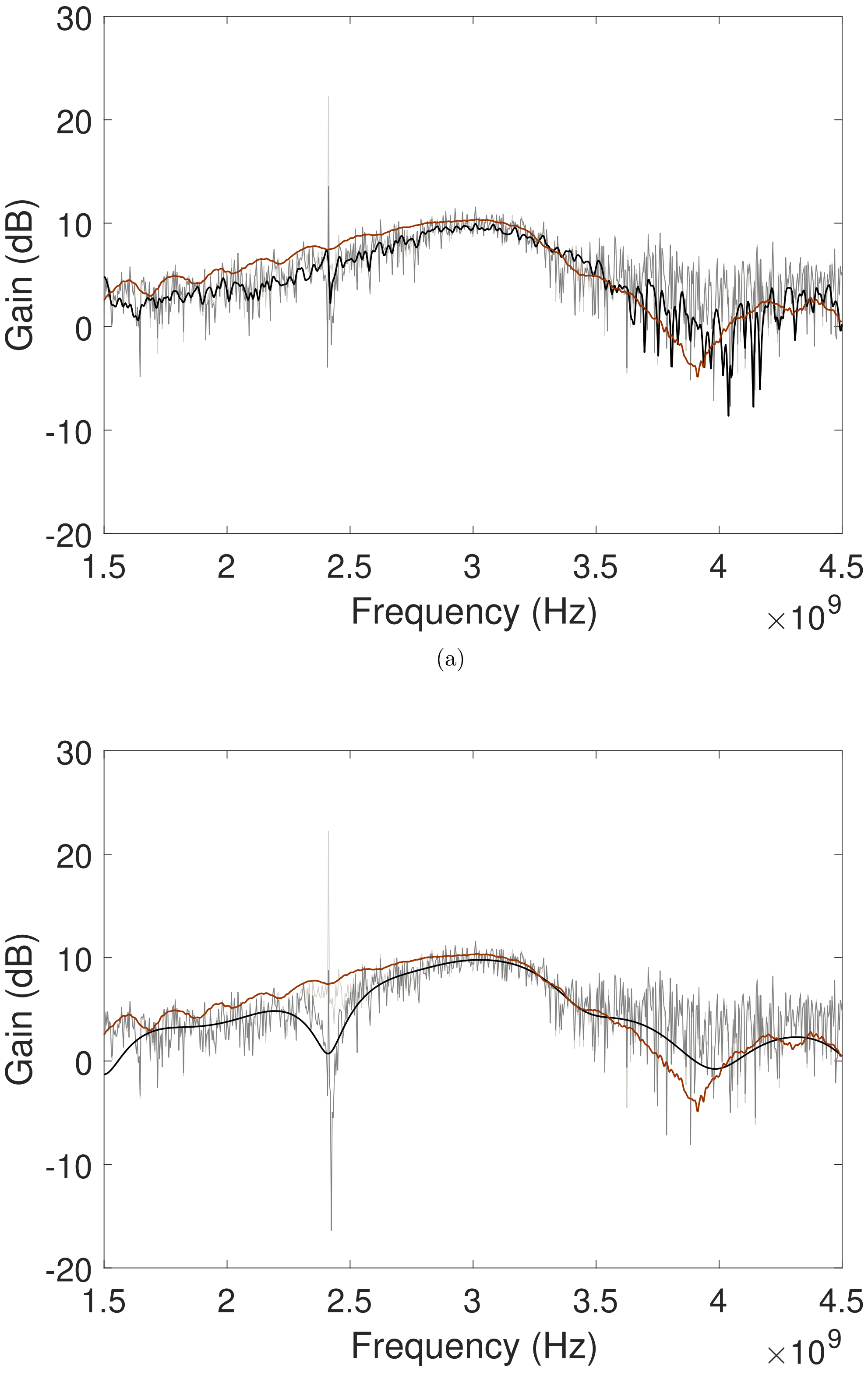

(a)

(b)

Figure 6.3 – AUT1 gain curves revealing the performance of the ASP-1 technique. Light gray ■: noisy signal measured in Lab1. Dark gray ■: AF output. Black ■: TG output. Violet ■: reference curve obtained in Cha1. (a) PSO with the proposed fitness. AF parameters: $(\mu, L) = (0.0456, 27)$. (b) PSO with the MSE fitness. AF parameters: $(\mu, L) = (0.1, 49)$.

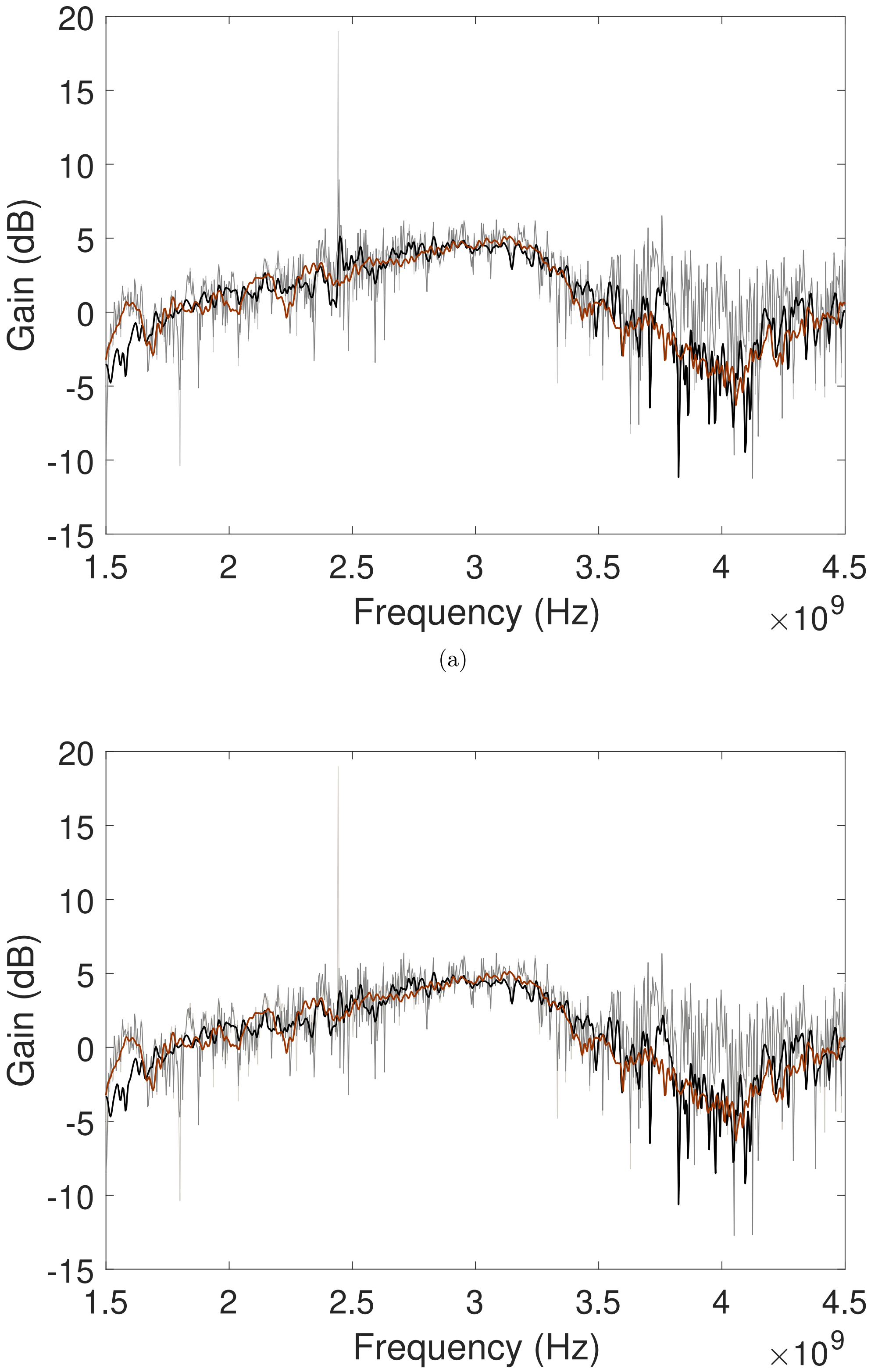

(a)

(b)

Figure 6.4 – AUT2 gain curves revealing the performance of the ASP-1 technique. Light gray ■: noisy signal measured in Lab1. Dark gray ■: AF output. Black ■: TG output. Violet ■: reference curve obtained in Cha1. (a) PSO with the proposed fitness. AF parameters: $(\mu, L) = (0.01, 48)$. (b) PSO with the MSE fitness. AF parameters: $(\mu, L) = (0.1, 50)$.

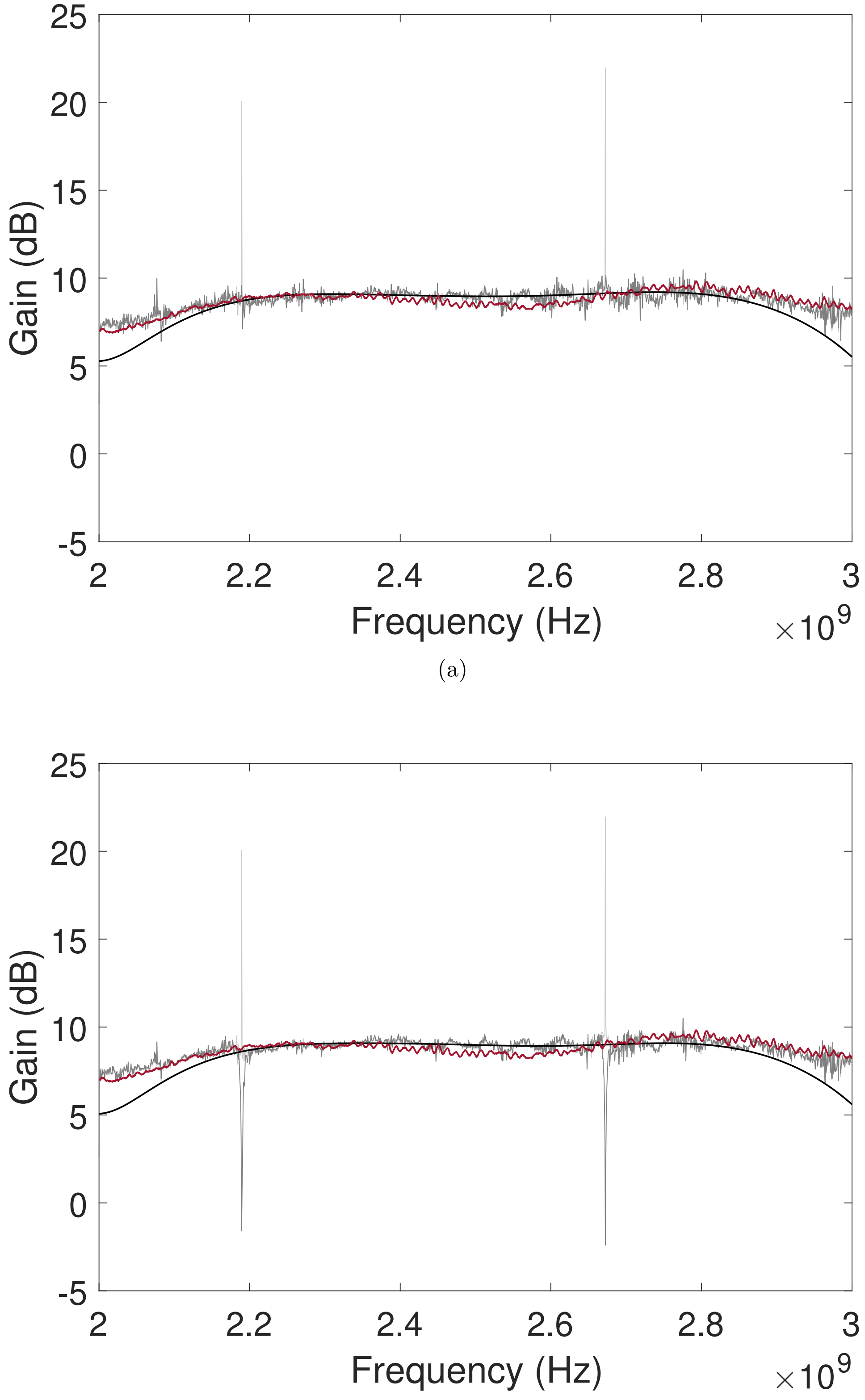

(a)

(b)

Figure 6.5 – AUT3 gain curves revealing the performance of the ASP-1 technique. Light gray ■: noisy signal measured in Lab1. Dark gray ■: AF output. Black ■: TG output. Violet ■: reference curve obtained in Cha1. (a) PSO with the proposed fitness. AF parameters: $(\mu, L) = (0.0151, 13)$. (b) PSO with the MSE fitness. AF parameters: $(\mu, L) = (0.1, 47)$.

in a greater reduction of the EMI and a smaller distortion in the frequencies around 2.4 GHz.

In turn, Fig. 6.4 shows good performances of both approaches when applied to the omnidirectional AUT2 antenna. Finally, the dark gray traces in Fig. 6.5 reveal a considerably better performance of the proposed fitness function at the AF output (first stage of the ASP-1 structure) for the directive AUT3 antenna. Nevertheless, the overall performances (black curves) are almost identical. In this case, the poor design of the AF generated by means of the MSE fitness was compensated by an efficient automatic design of the TG window. Consequently the overall performances achieved the same good level.

In order to verify the consistency of the (μ, L) parameters shown in Table 6.2, we ran the PSO routine 10 times per fitness function. Indeed, given the non-deterministic nature of the PSO, variations in the parameter values are expected. Table 6.3 shows these parameters, as well as the corresponding Pearson correlation coefficients between the filtered and reference anechoic chamber curves. The dispersion levels are higher for the proposed fitness function, but the correlation levels are, on average, higher than those obtained with the classical approach (0.8600 against 0.8142). Nevertheless, considerable increases in the correlation levels were noticed in both cases, reaching approximately 15% (MSE fitness) and 20% (proposed fitness).

Table 6.3 – (μ, L) parameters obtained after 10 PSO simulations with both MSE and proposed fitness functions and the corresponding correlation between filtered and chamber curves. The correlation between non-filtered and chamber curves is also shown. Filtering technique: ASP-1. Antenna: AUT1.

MSE fitness			Proposed fitness			Inertial weight	No filter
μ	L	Correlation	μ	L	Correlation	—	—
0.10000	50	0.8518	0.04153	22	0.8746	Decreasing	—
0.10000	46	0.7941	0.05630	13	0.8477	Decreasing	—
0.10000	46	0.7941	0.04561	27	0.8703	Decreasing	—
0.10000	44	0.8020	0.04561	27	0.8703	Decreasing	—
0.10000	42	0.8213	0.03056	15	0.8412	Decreasing	—
0.10000	49	0.8518	0.03479	14	0.8385	Increasing	—
0.10000	48	0.7876	0.04220	22	0.8746	Increasing	—
0.09890	46	0.7953	0.04220	22	0.8746	Increasing	—
0.10000	50	0.8518	0.07354	11	0.8541	Increasing	—
0.09970	47	0.7921	0.07095	11	0.8540	Increasing	—
Average correlation		0.8142	—	—	0.8600	—	0.6611

The same analyses were applied to AUT2 and AUT3, with results summarized in Tables 6.4 and 6.5. These tables reveal that the impact of the PSO fitness function over the filtering quality can change with the antenna type. Table 6.4 shows that the MSE fitness presents a 3% better performance than the proposed function. On the other hand,

Table 6.4 shows very similar performances, with a very small difference of 0.5%. In all cases, significant increases in the correlation levels were noticed, reaching approximately 25% (MSE fitness) and 22% (proposed fitness) for AUT2 and approximately 20% (MSE and proposed fitness) for AUT3.

Table 6.4 – (μ, L) parameters obtained after 10 PSO simulations with both MSE and proposed fitness functions and the corresponding correlation between filtered and chamber curves. The correlation between non-filtered and chamber curves is also shown. Filtering technique: ASP-1. Antenna: AUT2.

MSE fitness			Proposed fitness			Inertial weight	No filter
μ	L	Correlation	μ	L	Correlation	—	—
0.10000	48	0.8692	0.08785	47	0.8693	Decreasing	—
0.10000	48	0.8692	0.07693	16	0.8391	Decreasing	—
0.08317	44	0.8703	0.08801	16	0.8401	Decreasing	—
0.10000	40	0.8710	0.07443	16	0.8389	Decreasing	—
0.09575	50	0.8794	0.01266	22	0.8484	Decreasing	—
0.10000	49	0.8696	0.09638	16	0.8406	Increasing	—
0.10000	50	0.8794	0.05300	17	0.8478	Increasing	—
0.08217	48	0.8690	0.05845	17	0.8478	Increasing	—
0.09612	49	0.8788	0.08589	17	0.8478	Increasing	—
0.09549	49	0.8788	0.08520	16	0.8399	Increasing	—
Average correlation		0.8735	—	—	0.8460	—	0.6224

Table 6.5 – (μ, L) parameters obtained after 10 PSO simulations with both MSE and proposed fitness functions and the corresponding correlation between filtered and chamber curves. The correlation between non-filtered and chamber curves is also shown. Filtering technique: ASP-1. Antenna: AUT3.

MSE fitness			Proposed fitness			Inertial weight	No filter
μ	L	Correlation	μ	L	Correlation	—	—
0.10000	39	0.7802	0.02715	13	0.7738	Decreasing	—
0.09320	40	0.7812	0.05517	50	0.7777	Decreasing	—
0.07891	47	0.7800	0.02741	12	0.7734	Decreasing	—
0.09884	40	0.7817	0.01048	30	0.7724	Decreasing	—
0.09711	49	0.7821	0.02528	48	0.7742	Decreasing	—
0.09182	47	0.7812	0.02103	49	0.7741	Increasing	—
0.10000	47	0.7820	0.01210	21	0.7697	Increasing	—
0.10000	35	0.7800	0.07839	49	0.7803	Increasing	—
0.10000	40	0.7818	0.10000	50	0.7820	Increasing	—
0.10000	39	0.7802	0.02560	12	0.7733	Increasing	—
Average correlation		0.7810	—	—	0.7751	—	0.5826

6.2 ASP-2

The evaluation of the ASP-2 technique is based on the previously discussed GSM-R and jamming signals models. During this stage, we weight the corresponding time sequences in order to control the signals power and therefore the SJR. Another important aspect of our methodology refers to the number of times we run the computational routines. Since our GSM-R model is based on random bit sequences, the filtered signals waveforms can change from one execution to another. To handle these variations, we run 10 times our codes to get an average (SJR,BER) pair. Then, we change the mentioned weights and, again, we run 10 times the codes to get another (SJR,BER) pair, and so on. In all cases, the ALE filter was configured with the following parameters: $(\mu, L, \Delta) = (0.001, 20, 2.692 \times 10^4)$. This particular Δ value corresponds to the second peak of the jamming signal autocorrelation function. Besides, we used the DR technique with the number of signal replicas being equal to 1. This means that the resulting signal contains the original waveform and one replica, one after another in the time domain.

When synthesizing the noisy communication signals, we followed a two-step process. First, we separately generated its narrowband GSM-R component and then the broadband jamming contribution, as illustrated in Fig. 6.6 in a SJR = -0.85 dB scenario. Then, we summed the two real-valued vectors.

To proceed with our analyses, we introduce a band-pass filter that represents the operating frequency band of a typical GSM-R receiver. In practice, it represents both the gain profile of narrowband GSM-R antennas and the selectivity of band-pass filters

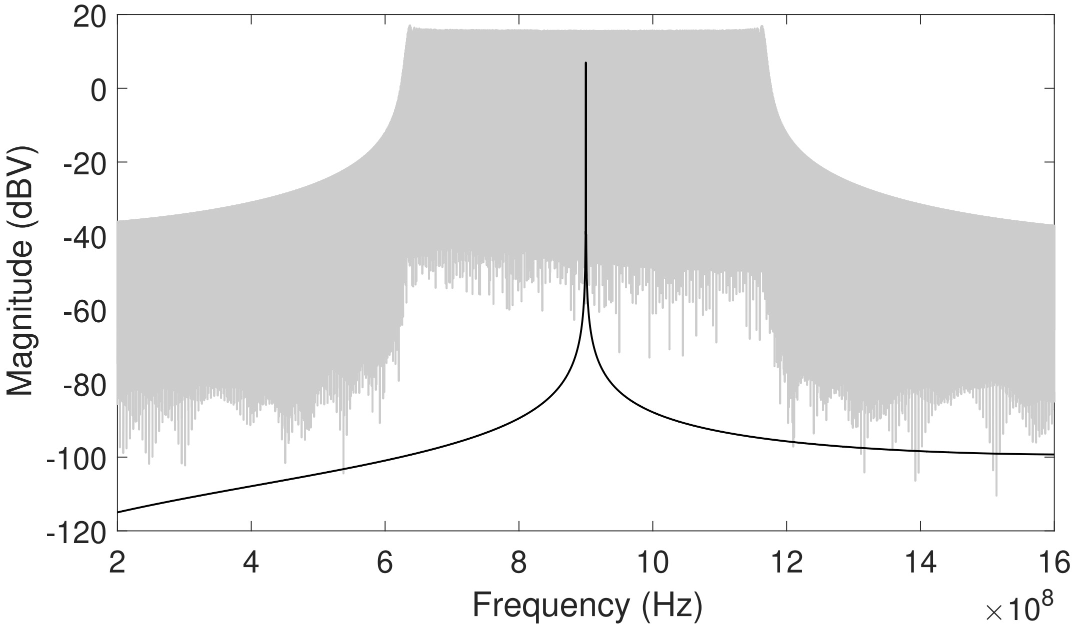

Figure 6.6 – Magnitude response of the narrowband GSM-R and broadband jamming signals in a SJR = -0.85 dB scenario.

present in GSM-R receivers. As a result, the out-of-band jamming power is eliminated. Then, we apply the ASP-2 algorithm. The results are exposed in Figs. 6.7 and 6.8, in terms of magnitude and phase responses, respectively.

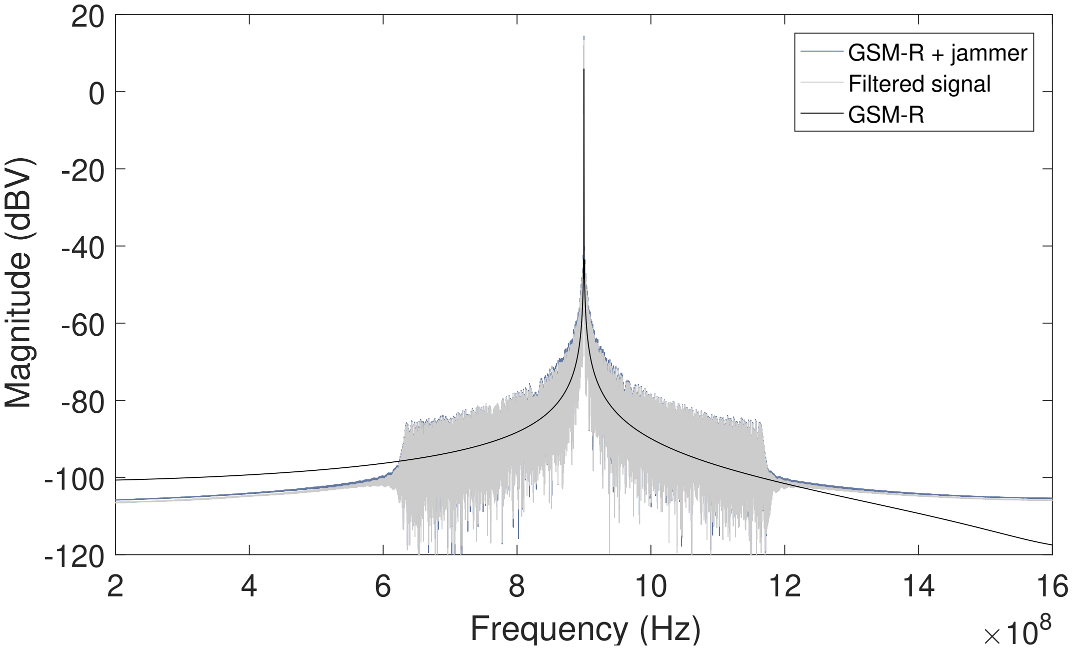

(a)

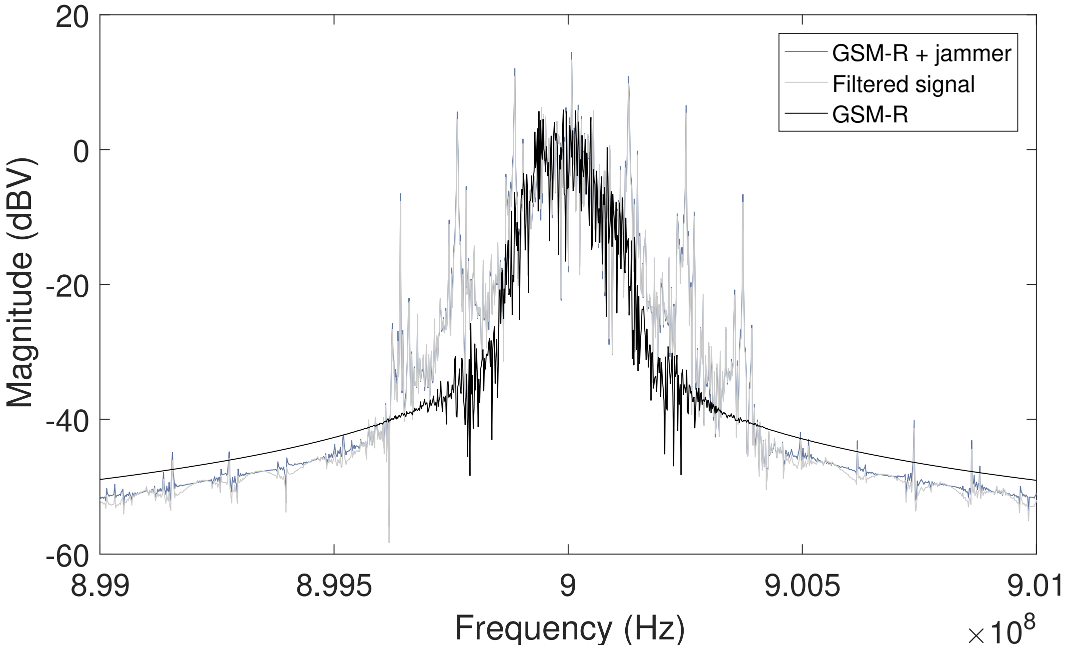

(b)

Figure 6.7 – Magnitude response of the noisy and noiseless GSM-R signals and the filtered version. Parameters of the ALE filter: $(\mu, L, \Delta) = (0.001, 20, 2.692 \times 10^4)$. The DR technique was used with 1 signal replica.

In Figs. 6.7, the band-pass filter effect is clear. If we compare the jamming signal curves in Figs. 6.6 and 6.7, we observe a 100 dB attenuation in the 600 MHz – 899.5

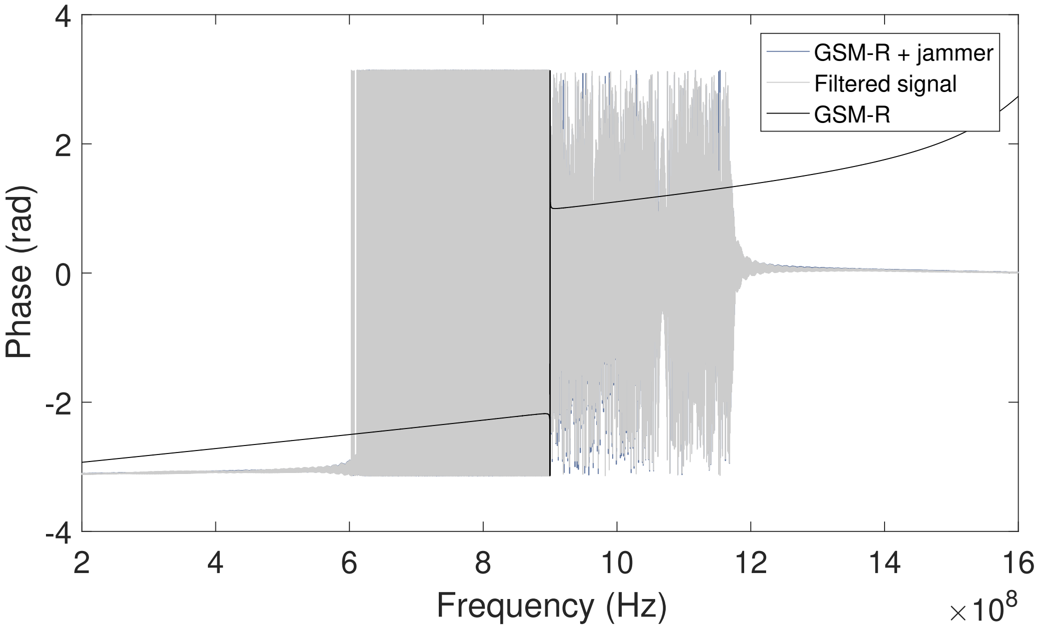

Figure 6.8 – Phase response of the noisy and noiseless GSM-R signals and the filtered version. Parameters of the ALE filter: $(\mu, L, \Delta) = (0.001, 20, 2.692 \times 10^4)$. The DR technique was used with 1 signal replica.

MHz and 900.5 MHz – 1.2 GHz bands. In practical terms, this attenuation represents the effects of narrowband GSM-R antennas and/or the selectivity of band-pass filters present in GSM-R receivers. In Figs. 6.7 and 6.8, we also see the jamming effect. It tends to distort both the GSM-R magnitude shape and phase behavior. These figures also show the filtering effects. A first visual inspection on these graphs reveals a negligible signal recovery. Nevertheless, a comparison involving the transmitted, received and filtered bit sequences reveal significant BER reductions, as detailed in the next paragraphs.

Figure 6.9 shows three binary sequences, obtained by demodulating both transmitted (top) and received GSM-R signals (center and bottom) in a SJR = -1.06 dB scenario. The difference between the center and bottom plots is that the ASP-2 algorithm is turned off in the center plot and on in the bottom plot. To identify the corrupted bits, we used dashed boxes and markers. In particular, we highlight two time samples with markers: time index = 42 and time index = 98. The first one indicates that the filter correctly recovered a corrupted bit, while the second one indicates that the filter did not work properly. Nevertheless, a visual inspection based on the number and sizes of dashed boxes reveals that the number of corrupted bits decreased (and so the BER) with the use of the ASP-2 technique.

The BER calculation was then averaged after 10 simulations for this particular level of SJR. Later on, we repeated this procedure for other SJR values, as illustrated in Fig. 6.10. This graph reveals BER reductions over the $-2.77dB \leq SJR < 1.16dB$ range. These reductions reached the maximum value of 10 % when $SJR = -2.77dB$.

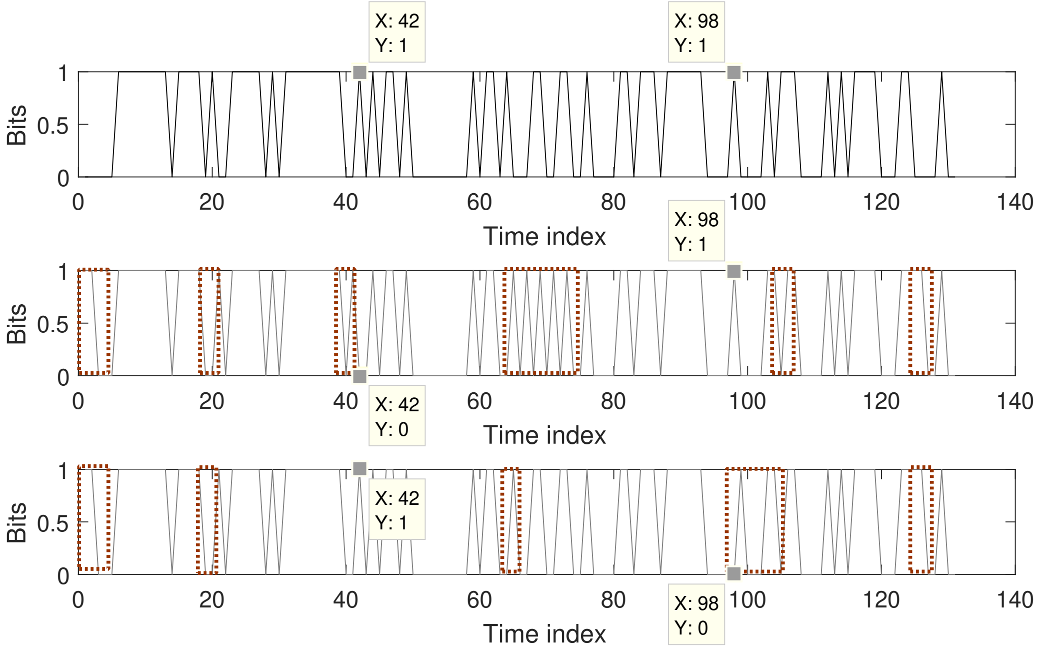

Figure 6.9 – Example of the BER reduction obtained with the ASP-2 technique, in a SJR = -1.06 dB scenario. Top: noiseless reference bit sequence. Middle: received sequence with ASP-2 turned off (BER = 12.21 %). Bottom: received sequence with ASP-2 turned on (BER = 9.16 %). The black dashed rectangles highlight the corrupted bits.

In Fig. 6.10, we also highlight a critical BER which equals the 12.5 % level. According to measurement results reported in (32), the GSM-R communication between the train and the base-station can be lost if the BER exceeds this limit. Using this information, we identify two critical points in Fig. 6.10 where the BER = 12.5 % condition is verified. The first one is obtained through the 'no filter' curve, corresponding to SJR ≈ -0.84. The second one can be obtained in the same way, but using the 'with filter' curve. In this case, SJR = -1.95 dB. This result indicates that the ASP-2 algorithm changed the GSM-R system SJR threshold from SJR ≈ -0.84 dB to SJR = -1.95 dB. In other words, a SJR gain (defined here as the difference between the two critical SJR levels) of 1.11 dB was observed, increasing thus the operational range of the GSM-R communication link. Consequently, the proposed technique increased the system robustness against a frequency-modulated jamming attack in our simulations.

6.3 Final considerations

In this chapter, we showed experimental and computational results concerning the proposed interference mitigation techniques. First, we explored DAE-1 and ASP-1 when applied to the antenna calibration problem. A benchmark analysis involving the state-of-the-art DAE-2 technique and chamber results indicates that all the approaches

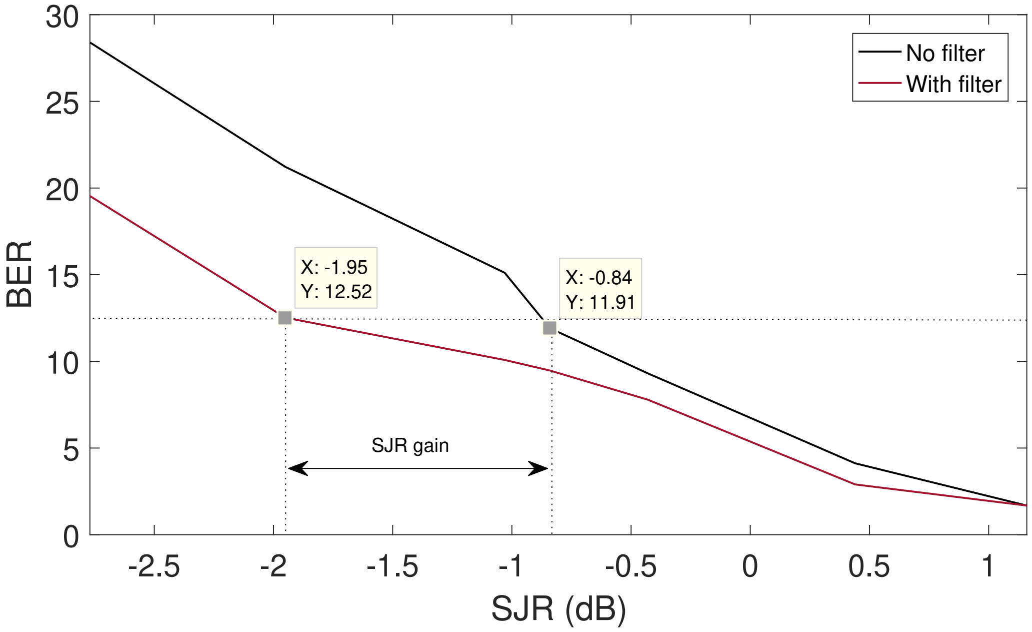

Figure 6.10 – Quality of the GSM-R communication with and without the ASP-2 algorithm. This graph highlights a critical situation where the BER = 12.5 %. It also indicates that the ASP-2 algorithm changed the GSM-R system SJR threshold from SJR ≈ -0.84 dB to SJR = -1.95 dB.

provide noise attenuation within the antennas operating bands. Nevertheless, we noticed that, in some cases, the AF may not only eliminate noise but also the useful S_{12} portion.

In a second moment, we discussed the effects of the new fitness function proposed for the PSO algorithm. Graphical analyses based on AUT1, AUT2 and AUT3 indicated that the proposed fitness can provide equal or better results than those provided by the MSE function. This observation was endorsed after running 20 times the PSO algorithm (10 times with the proposed fitness and 10 times with the MSE function). By defining the correlation of the resulting filtered gain curves with the chamber measurements as a metric, we compared the performances. In average, our approach provided a performance gain of approximately 4.5% when compared to the state-of-the-art.

Finally, we analysed the ASP-2 technique when applied to the IEMI problem. Simulation results show that the ALE filter can provide BER reductions within the $-2.77dB \leq SJR < 1.16dB$ range. These reductions can reach up to approximately 10 % when the SJR = -2.77 dB. They suggest an increase of the GSM-R system robustness face to frequency-modulated jamming attacks. This is due to the fact that the threshold SJR level (above which the GSM-R communication can be lost) changed from ≈ -0.84 dB to SJR = -1.95 dB.

Chapter 7

Conclusions

This chapter is divided into two sections. In the first moment, we summarize all the findings and novelties of this work. Then, we show and detail some ideas for future works. All these ideas emerged throughout this research but could not be developed either because of limited time or simply because they were out of the scope of this research. Nevertheless, we believe that they can be useful for future developments in this field of research.

7.1 Summary of the main contributions

The most immediate contribution of this work is the shortening of the bridge between the signal processing and electromagnetic compatibility fields. We tried to show that most signal processing tools are not ready to be applied to EMC problems in their classical configurations. In this sense, we proposed a series of modifications over these classical tools in order to make them suitable for the proposed case studies. Furthermore, we proposed auxiliary mechanisms to facilitate their use by EMC professionals.

We show the main contributions of this dissertation in two separated categories. The first one refers to what we call *findings*, while the second category is referred to as *novelties*. Findings are analyses that evidence some phenomena which, to the best of our knowledge, were not discussed before by the EMC community. On the other hand, the novelties are the proposals made in this dissertation which were validated by experimental, computational and/or statistical methods.

1. Findings

1.1 Time gating can fail in low SNR environments

We showed that, in low SNR environments, the TG performance can significantly vary for the same EMI. This variation is in turn related to an uncontrollable variable: the phase of the interfering sgnal.

1.2 The error signal of ALE filters can serve as accurate filtering solutions depending on the signals characteristics and on the choice of the Δ *parameter*

In its original formulation, the ALE filter is used to identify sine waves with unknown frequencies embedded in white background noise. In these cases, the filtered sine wave is taken at the output of the $H(z)$ block (see Fig. 5.7). Nevertheless, we obtained better results by alternatively reading the output of the summation block, *i.e.* by considering that $e[n]$ is the filtered GSM-R signal.

2. Novelties

2.1 Three interference mitigation techniques: DAE-1, ASP-1 and ASP-2

The DAE-1 and ASP-1 techniques were validated after an extensive process involving experimental measurements in four different test sites (Lab1, Lab2, Cha1, Cha2), three different antennas (AUT1, AUT2, AUT3), graphical and statistical analyses. On the other hand, the ASP-2 validation was affected by hardware problems. Nevertheless, simulation results reveal a potential to solve the IEMI problem.

2.2 A new fitness function for the PSO algorithm

The automatic adjustment of the AF parameters via PSO was first proposed in (9). Nevertheless, we verified that the fitness function used by these authors can eventually lead to non-satisfactory results. To solve this issue, we propose a new fitness function, Eq. 5.7. After running the PSO-AF routine several times with each candidate function, we observe a gain of approximately 4.5% of the proposed fitness over the MSE function.

2.3 A new window design routine for TG

Using the TG technique involves defining the window function, length and position. Such a feature is usually present in commercial VNAs but these adjustments are usually manual. This can take a certain time and reduce the filtering process accuracy. We propose an automatic window design routine, configured after a time-domain analysis of typical antennas responses. For these analyses, we considered three different antennas, aiming to not restrict the applications of this technique.

7.2 Future work

The ideas for future work are organized in topics, as follows.

1. Improving the antenna calibration filtering results

1.1 New methodologies to measure the noise floor

The methodology used in this work to measure the noise floor for further ASP-1 processing has flaws. We used two different test setups: (i) a pair of antennas and (ii) one antenna and a 50 Ω load. The first one was used to measure S_{12}, while the second one was used to measure the noise floor. This inevitably creates a time interval between the measurements, which can cause an impact over the filters' performances.

The first thing to note is that, although the EMI source (*e.g.* a WiFi router) remains still at its position in relation to the test setup in both measurements, the phase of the interfering signal as "seen" by the receiving antenna can change. The second observation concerns the intermittent nature of the EMI source. If the interfering signal has its frequency and/or power constantly changed, this can reduce the cross-correlation between $j_1[n]$ and $j_2[n]$, as already discussed in Section 6.1.

These observations evidence the need for a more efficient methodology to measure the noise floor. We believe this can improve the results obtained with ASP-1.

1.2 Use of the adaptive filter to cancel multipath and random noise floor

The ASP-1 technique uses 4 sub-structures to filter the signals: (i) AF, (ii) PSO, (iii) TG and (iv) window design algorithm. We believe we can eliminate (iii) and (iv) - and therefore simplify the structure and perhaps get better results - if we are able to configure the adaptive filter to cancel not only EMI but also multipath and random noise floor.

The use of AF for acoustic echo canceling is known (36). Also, there is currently many researches in this field. From a signal processing perspective, we can say that both acoustic echo and multipath are similar phenomena. Both are attenuated and delayed versions of the main signal, each one in its own domain (acoustic or electromagnetic). So we believe it is possible to configure the AF-based echo canceling system to mitigate multipath and then improve the antenna calibration filtering results. A possible tool to be used in such an investigation is the reverbering chamber. This facility can be used to generate different (and controlled) reflection patterns.

Another contribution in this sense would be the noise floor canceling by the AF. We believe the noise floor present in VNA measurements is essentially random. Therefore, its autocorrelation tends to decay fast. If this premise holds true, then an ALE filter with a $\Delta = 1$ (or something close to this value) would be enough to create a shifted signal which is decorrelated from the noise floor. To confirm this hypodissertation, one can change the ANC configuration present in the ASP-1 strucutre by an ALE filter.

With these two structural changes, ALE-1 would reduce to an ALE filter tuned by the PSO algorithm. This would certainly simplify its implementation and possibly improve the filtering quality.

1.3 Minimizing the DAE-1 test duration and improving the benchmark analyses

The main drawback of the DAE-based approaches analysed in this work is the total test time. In general, the accuracy of these methods is proportional to N, the number of experimental runs. Nevertheless, we believe there is a certain value where saturation is observed. In other words, no matter how much you increase N, accuracy is no longer significantly impacted.

In order to minimize N and ensure optimal DAE-1 performances in terms of speed, we propose the use of techniques such as that proposed by (84). These authors propose a methodology that estimates optimal sample sizes required to compare multiple algorithms.

We believe an optimal N would not only be useful to optimize DAE-1 but also to improve the benchmark analysis accuracy. When comparing the proposed methods with the state-of-the art (*e.g.* proposed fitness *versus* MSE function, as summarized in Table 6.3), we used empirical Ns which we believed to be sufficient. Nevertheless, it is possible that we were under- or over-sampling the random processes. Therefore, it is of a great importance to adopt methodologies to optimize the sample sizes.

2. Use of DAE-1 and ASP-1 for compliance tests

The interference mitigation techniques proposed in this work were primarily designed for pre-compliance tests. Therefore, in the benchmark analyses, we compare their performances to the state-of-the-art and to reference values but we do not include normative compliance requirements for product or test site validation.

In future studies, one can evaluate if the DAE-1 and ASP-1 techniques are able to create "virtual" anechoic environments. It would mean that a non-compliant test site (*i.e.* a place where EMC or antenna calibration tests cannot be run - at least, for product validation) could turn into a compliant one with signal processing. Indeed, this sort of approach is "authorized" by the standards. See, for instance, the Annex K of the ANSI C63.5-2017 standard (3).

One way of doing this is to evaluate the criteria defined by the standards before and after applying the filters. Such a methodology has already been used - see *e.g.* (10; 9). As an example, one can take one of the criteria defined by the ANSI C63.5-2017 standard to certify if a given test place is suitable for antenna calibration tests, *e.g.* the item J.2.1.3 b). According to this item, one shall measure the *site attenuation* (which is based on the S_{12} parameter) under two circumstances: (i) with vertically polarized antennas and (ii) with horizontally polarized antennas. The difference between the site attenuation estimates shall be less than 1 dB. So if this difference is higher than 1 dB without the filter but is less than 1 dB with it, we can say the signal processing structure creates a "virtual" anechoic environment.

3. New set of SDR-based measurements

Given the already mentioned hardware problems, we could not use the SDR measurements to conclude about the filters' performances. Therefore, new methodologies to get reliable data from the SDR-based tests are necessary. Indeed, problems such as the CFO are not rare in SDR systems and questions on how to deal with them can be found in online forums. One possible explanation is the hardware quality, which is proportional to the low prices of devices such as the HackRF One.

One example of such methodologies would be sending an extra sine wave together with the GSM-R signal. The sinusoidal signal, tuned to the GSM-R carrier frequency, would be used to synchronize the received and transmitted signals. This could minimize the CFO. Another possibility is to add synchronization bytes to the transmitted binary sequence.

Although not related to the hardware issues, an interesting option to improve the SDR-based analyses would be randomize the transmitted binary sequence. In this work, we used known periodic sequences. Nevertheless, we believe that random sequences could provide more accurate BER estimates.

4. Real-time implementation of the ASP-2 technique

The IEMI problem described in this work requires real-time filtering. The jamming attack must be suppressed exactly when it occurs. Therefore, after solving the already mentioned SDR issues and validating the ASP-2 technique with a physical test setup, a real-time implementation of this method shall be considered.

Nevertheless, the transition between the offline to the online operating modes is not direct. Many important aspects shall be analyzed first. For example, according to the simulation results, the NLMS algorithm transient response is relatively low. So we either adapt the DR technique to the online mode or we choose another adaptive algorithm with a faster response. In the first scenario, we could gradually store the received signal samples in a buffer so they can be used in the real-time NLMS learning processes.

Another possible constraint is the AF parameter selection. According to the BER analyses results discussed in Chapter 6, the ALE filter performance can significantly vary with the SJR. In a scenario where this parameter can evolve in an unpredicTable way with time, different AF parameters can be required. The PSO algorithm present in the ASP-1 structure is totally incompatible with real-time applications. One solution is to previously estimate the optimal parameters for a certain SJR range. Then, the hardware can be programmed to switch from one set of parameters to another depending on the SJR conditions.

Despite the mentioned constraints, we believe a real-time implementation of the ASP-2 technique is possible. We also believe this is a promising mitigation technique for intentional or non-intentional EMI in the railway environment. Its easiness of implementation and re-configuration according to the needs is an attractive feature when compared to other EMC solutions.

8. Combination of filters

Some recent researches show that it is possible to combine adaptive filters in series, parallel or in both ways. The resulting structure contains a pool of filters (all fed by the same noisy input signal) and a supervisor. The latter constantly makes linear combinations of the individual filters output signals. Consequently, the overall filtering process takes into account the best performances of the pool. With this powerful methodology, it is possible to produce a hybrid performance which can overcome the individual ones in terms of speed and accuracy (78).

This approach can be used in future real-time applications of the ASP-2 technique. Its use is motivated by the fast and random changes in the jammer location inside the train. The resulting SJR level changes can demand a dynamic adjustment of the AF. Therefore, we could use a pool of candidate filters supervised in real-time to produce good BER reductions regardless of the SJR, avoiding AF performance degradation.

9. Other signal processing techniques

Besides AF, one can also try other methods to solve EMI problems. Signal detection theory and blind signal separation are some examples.

References

1 MOLOGNI, J. F. et al. Investigating gsm interference in automotive sound systems using state of the art electromagnetic simulation. In: *SAE Technical Paper*. SAE International, 2013. Disponível em: <https://doi.org/10.4271/2013-36-0198>.

2 PAUL, C. R. *Introduction to electromagnetic compatibility*. [S.l.]: John Wiley & Sons, 2006. v. 184.

3 ANSI. American national standard for electromagnetic compatibility–radiated emission measurements in electromagnetic interference (emi) control–calibration and qualification of antennas (9 khz to 40 ghz). *ANSI C63.5-2017 (Revision of ANSI C63.5-2005)*, p. 1–114, May 2017. ISSN null.

4 Deniau, V. Overview of the european project security of railways in europe against electromagnetic attacks (secret). *IEEE Electromagnetic Compatibility Magazine*, v. 3, n. 4, p. 80–85, 2014.

5 Rodriguez, V. Automotive component emc testing: Cispr 25, iso 11452–2 and equivalent standards. *IEEE Electromagnetic Compatibility Magazine*, v. 1, n. 1, p. 83–90, 2012.

6 Kummer, W. H.; Gillespie, E. S. Antenna measurements—1978. *Proceedings of the IEEE*, v. 66, n. 4, p. 483–507, 1978.

7 Frech, A.; Russer, P. Real-time ambient noise cancellation for emi measurements on open area test sites. In: *2012 Asia-Pacific Symposium on Electromagnetic Compatibility*. [S.l.: s.n.], 2012. p. 213–216.

8 Frech, A. et al. Ambient noise cancelation with a time-domain emi measurement system using adaptive filtering. In: *2008 Asia-Pacific Symposium on Electromagnetic Compatibility and 19th International Zurich Symposium on Electromagnetic Compatibility*. [S.l.: s.n.], 2008. p. 534–537.

9 Sheng, L.; Bangmin, W.; Lanyong, Z. Intelligent adaptive filtering algorithm for electromagnetic-radiation field testing. *IEEE Transactions on Electromagnetic Compatibility*, v. 59, n. 6, p. 1765–1780, Dec 2017.

10 AWAN, F. G.; KIRAN, A. Cancellation of interference for emission measurement in open area test site. *Measurement*, v. 111, p. 183 – 196, 2017. ISSN 0263-2241. Disponível em: <http://www.sciencedirect.com/science/article/pii/S0263224117304736>.

11 AWAN, F. G.; SHEIKH, N. M. Model for radiation emission emc measurement at oats: Issues and approaches. *Measurement*, v. 42, n. 7, p. 1045 – 1052, 2009. ISSN 0263-2241. Disponível em: <http://www.sciencedirect.com/science/article/pii/S0263224109000566>.

12 *Smart Antenna Systems*. 2020. <http://www.cs.binghamton.edu/~vinkolar/directional/smart_ant.pdf>. Access: 11/01/2020.

13 BAKR, O. M.; JOHNSON, M. *Impact of phase and amplitude errors on array performance*. 2009. <https://digitalassets.lib.berkeley.edu/techreports/ucb/text/EECS-2009-1.pdf>. Access: 11/01/2020.

14 BERTRAND, H.; GRENIER, D.; ROY, S. Experimental antenna array calibration with artificial neural networks. *Signal Processing*, v. 88, n. 5, p. 1152 – 1164, 2008. ISSN 0165-1684. Disponível em: <http://www.sciencedirect.com/science/article/pii/S0165168407003775>.

15 Abohamra, Y. A. et al. Direction of arrival algorithms for user identification in cellular networks. In: *2016 IEEE 7th Annual Information Technology, Electronics and Mobile Communication Conference (IEMCON)*. [S.l.: s.n.], 2016. p. 1–7.

16 HYEON, S.; YUN, Y.; CHOI, S. Novel automatic calibration technique for smart antenna systems. *Digital Signal Processing*, v. 19, n. 1, p. 14 – 21, 2009. ISSN 1051-2004. Disponível em: <http://www.sciencedirect.com/science/article/pii/S1051200407001522>.

17 CORDEAU, D.; PAILLOT, J.-M. In: *ECAI 2011 - International Conference – 4th Edition Electronics, Computers and Artificial Intelligence*. [S.l.: s.n.].

18 Sasakawa, D. et al. Antenna array calibration for living-body radar. *IEEE Antennas and Wireless Propagation Letters*, v. 15, p. 246–249, 2016.

19 Kim, S. Y.; Sung, J. B.; Torre, A. In-orbit antenna pattern extraction method for active phased-array sar antennas. *IEEE Antennas and Wireless Propagation Letters*, v. 15, p. 317–320, 2016.

20 Zhang, Y.; Mao, J. An overview of the development of antenna-in-package technology for highly integrated wireless devices. *Proceedings of the IEEE*, v. 107, n. 11, p. 2265–2280, 2019.

21 BRONCKERS, L. *Design and measurement techniques for next-generation integrated antennas*. Tese (Doutorado) — Technische Universiteit Eindhoven, set. 2019.

22 Fróes, S. M. et al. Antenna radiation pattern measurement in a nonanechoic chamber. *IEEE Antennas and Wireless Propagation Letters*, v. 18, n. 2, p. 383–386, Feb 2019.

23 KHANDUZI, R.; SANGAIAH, A. K. Tabu search based on exact approach for protecting hubs against jamming attacks. *Computers & Electrical Engineering*, v. 79, p. 106459, 2019. ISSN 0045-7906. Disponível em: <http://www.sciencedirect.com/science/article/pii/S0045790618333743>.

24 Lopez, I.; Aguado, M. Cyber security analysis of the european train control system. *IEEE Communications Magazine*, v. 53, n. 10, p. 110–116, 2015.

25 Pelechrinis, K.; Iliofotou, M.; Krishnamurthy, S. V. Denial of service attacks in wireless networks: The case of jammers. *IEEE Communications Surveys Tutorials*, v. 13, n. 2, p. 245–257, 2011.

26 Mansson, D. et al. Vulnerability of european rail traffic management system to radiated intentional emi. *IEEE Transactions on Electromagnetic Compatibility*, v. 50, n. 1, p. 101–109, 2008.

27 Villain, J. et al. Em monitoring and classification of iemi and protocol-based attacks on ieee 802.11n communication networks. *IEEE Transactions on Electromagnetic Compatibility*, v. 61, n. 6, p. 1771–1781, 2019.

28 Lyamin, N. et al. Real-time detection of denial-of-service attacks in ieee 802.11p vehicular networks. *IEEE Communications Letters*, v. 18, n. 1, p. 110–113, 2014.

29 Wu, Y. et al. Position manipulation attacks to balise-based train automatic stop control. *IEEE Transactions on Vehicular Technology*, v. 67, n. 6, p. 5287–5301, 2018.

30 Mili, S. et al. Recognition process of jamming signals superimposed on gsm-r radiocommunications. In: *2013 International Symposium on Electromagnetic Compatibility*. [S.l.: s.n.], 2013. p. 45–50.

31 MILI, S. et al. Jamming detection methods to protect railway radio communication. *International Journal of Engineering*, v. 4, 2015.

32 Heddebaut, M. et al. Mitigation techniques to reduce the vulnerability of railway signaling to radiated intentional emi emitted from a train. *IEEE Transactions on Electromagnetic Compatibility*, v. 59, n. 3, p. 845–852, 2017.

33 He, R. et al. High-speed railway communications: From gsm-r to lte-r. *IEEE Vehicular Technology Magazine*, v. 11, n. 3, p. 49–58, 2016.

34 JOSE, A. N. de S. et al. Proposal for a brazilian regulation of electromagnetic compatibility applied to automotive vehicles. In: *2016 IEEE International Symposium on Electromagnetic Compatibility (EMC)*. [S.l.: s.n.], 2016. p. 495–500. ISSN 2158-1118.

35 SAYED, A. *Adaptive Filters*. Wiley, 2011. (Wiley - IEEE). ISBN 9781118210840. Disponível em: <https://books.google.fr/books?id=VBaenqIVftUC>.

36 PAULO, S. D. et al. Adaptive filtering: algorithms and practical implementation. *The international series in Engineering and Computer Scienc*, Springer, p. 23–50, 2008.

37 BALANIS, C. A. Antenna theory, hoboken. *New Jersey: John Wiley & Sons, Inc*, v. 8, p. 21–31, 2005.

38 IEEE. Ieee standard test procedures for antennas. *ANSI/IEEE Std 149-1979*, 1979.

39 SNCF. *Carte Générale*. [S.l.], 2020. Disponível em: <https://en.oui.sncf/sites/default/files/images/carte_generale_en_0.jpg>.

40 BIER, H. Introducing gsm-r in a live railway system: Experiences and lessons learned at the german railways. In: *Conference On Railway Enginerring*. [S.l.: s.n.], 2004. p. 06.01–06.07.

41 SOURE, J. A. F. de. *Implementação do sistema GSM-R na rede ferroviária nacional: projeto-piloto*. Dissertação (Mestrado) — Instituto Superior de Engenharia de Coimbra, Coimbra, October 2013.

42 DEMOULIN, C.; Van Droogenbroeck, M. Principes de base du fonctionnement du réseau gsm. *Revue de l'AIM*, n. 4, p. 3–18, 2004. Disponível em: <http://www.telecom.ulg.ac.be/publi/publications/mvd/Demoulin2004Principes/index.html>.

43 Giri, D. V.; Tesche, F. M. Classification of intentional electromagnetic environments (ieme). *IEEE Transactions on Electromagnetic Compatibility*, v. 46, n. 3, p. 322–328, 2004.

44 Deniau, V. et al. Ieee 802.11n communications in the presence of frequency-sweeping interference signals. *IEEE Transactions on Electromagnetic Compatibility*, v. 59, n. 5, p. 1625–1633, 2017.

45 AFRICANO, M. et al. Ground-penetrating radar antenna design for homogeneous and low-loss dielectric multilayer media. *Journal of Microwaves, Optoelectronics and Electromagnetic Applications (JMOe)*, v. 19, n. 2, p. AoP 137–151, Apr. 2020. Disponível em: <http://www.jmoe.org/index.php/jmoe/article/view/810>.

46 SYSTEMS, I. A. *SAS-571 Double Ridge Guide Horn Antenna*. 2019. <https://www.ahsystems.com/datasheets/SAS-571_Horn_Antenna_Datasheet.pdf>. Access: 10/31/2019.

47 de São José, A. N. et al. Uncertainties minimization in open environment antenna gain estimations. In: *2017 IEEE 3rd Global Electromagnetic Compatibility Conference (GEMCCON)*. [S.l.: s.n.], 2017. p. 1–5.

48 SYSTEMS, I. A. *SAS-571 Double Ridge Guide Horn Antenna*. 2017. <http://ahsystems.ru/rupornye-antenny/sas-571-id72>. Access: 10/27/2020.

49 Fereira, A. S.; Barbin, S. E.; Kretly, L. C. Antenna signature: A qualitative analysis of planar antennas by electromagnetic scanning using tdr-time domain reflectometry. In: *2014 20th International Conference on Microwaves, Radar and Wireless Communications (MIKON)*. [S.l.: s.n.], 2014. p. 1–4.

50 MOLINA, L. et al. Identifying channel´ saturation in wi-fi networks via passive monitoring of ieee 802.11 beacon jitter. In: *Proceedings of the 15th ACM International Symposium on Mobility Management and Wireless Access*. [S.l.: s.n.], 2017. p. 63–70.

51 LATHI, B. P. *Modern Digital and Analog Communication Systems 3e Osece*. [S.l.]: Oxford University Press, Inc., 1998.

52 Marinov, O. Noise partition in s-parameter measurement. In: *2013 22nd International Conference on Noise and Fluctuations (ICNF)*. [S.l.: s.n.], 2013. p. 1–4.

53 SEYFRIED, D.; SCHUBERT, K.; SCHOEBEL, J. Investigations on the sensitivity of a stepped-frequency radar utilizing a vector network analyzer for ground penetrating radar. *Journal of Applied Geophysics*, v. 111, p. 234 – 241, 2014. ISSN 0926-9851. Disponível em: <http://www.sciencedirect.com/science/article/pii/S0926985114003103>.

54 Mubarak, F. A. et al. Noise behavior and implementation of interferometer-based broadband vna. *IEEE Transactions on Microwave Theory and Techniques*, v. 67, n. 1, p. 249–260, 2019.

55 TURLETTI, T. Gmsk in a nutshell. *Telemedia Networks and Systems Group LCS, MIT-TR*, 1996.

56 MONTGOMERY, D. C. *Design and analysis of experiments*. [S.l.]: John wiley & sons, 2017.

57 CAMPELO, F. *Lecture Notes on Design and Analysis of Experiments*. 2015. <https://github.com/fcampelo/Design-and-Analysis-of-Experiments>. Version 2.11, Chapters 1 and 3; Creative Commons BY-NC-SA 4.0.

58 Burnside, S. The application of design of experiments to rf systems. In: *2018 International Applied Computational Electromagnetics Society Symposium (ACES)*. [S.l.: s.n.], 2018. p. 1–2.

59 Chen, L.; Chen, C. Bumping ubm metal residue defect analysis and improvement using techniques of design of experiment (doe). In: *2017 IEEE 2nd Information Technology, Networking, Electronic and Automation Control Conference (ITNEC)*. [S.l.: s.n.], 2017. p. 1751–1755.

60 Phaengkieo, D.; Somlak, W.; Ruangsinchaiwanich, S. Transformer design by finite element method with doe algorithm. In: *2013 International Conference on Electrical Machines and Systems (ICEMS)*. [S.l.: s.n.], 2013. p. 2219–2224.

61 Silva Nunes Junior, M. A. et al. Design of experiments for sensitivity analysis of voltage sags variables. In: *2012 IEEE 15th International Conference on Harmonics and Quality of Power*. [S.l.: s.n.], 2012. p. 398–402.

62 Widrow, B. et al. Adaptive noise cancelling: Principles and applications. *Proceedings of the IEEE*, v. 63, n. 12, p. 1692–1716, 1975.

63 Dunsmore, J. Gating effects in time domain transforms. In: *2008 72nd ARFTG Microwave Measurement Symposium*. [S.l.: s.n.], 2008. p. 1–8.

64 KEYSIGHT. *Techniques for Time Domain Measurements - Using FieldFox handheld analyzers - Application Note*. 2018. <http://literature.cdn.keysight.com/litweb/pdf/5991-0420EN.pdf>. Access: 21-10-2018.

65 OPPENHEIM, A. V. *Discrete-time signal processing*. [S.l.]: Pearson Education India, 1999.

66 BARTIK, H. Antenna measurements using the mirror method with gating in a time domain. *RADIOENGINEERING-PRAGUE-*, CZECH TECHNICAL UNIVERSITY, v. 14, n. 4, p. 58, 2005.

67 REHMAN, A. et al. Development of a cost effective antenna radiation pattern measurement setup. In: *2016 16th Mediterranean Microwave Symposium (MMS)*. [S.l.: s.n.], 2016. p. 1–4. ISSN 2157-9830.

68 GONÇALVES, F. J. F. et al. Free-space materials characterization by reflection and transmission measurements using frequency-by-frequency and multi-frequency algorithms. *Electronics*, Multidisciplinary Digital Publishing Institute, v. 7, n. 10, p. 260, 2018.

69 ARCHAMBEAULT, B.; CONNOR, S.; DIEPENBROCK, J. Time domain gating of frequency domain s-parameter data to remove connector end effects for pcb and cable applications. In: IEEE. *Electromagnetic Compatibility, 2006. EMC 2006. 2006 IEEE International Symposium on*. [S.l.], 2006. v. 1, p. 199–202.

70 Lu, S. et al. A novel gsc beamformer using a combination of two adaptive filters for smart antenna array. *IEEE Antennas and Wireless Propagation Letters*, v. 11, p. 377–380, 2012.

71 Cheng, L. et al. Adaptive filter approach for gps multipath estimation under correntropy criterion in dynamic multipath environment. *IEEE Transactions on Signal Processing*, v. 67, n. 22, p. 5798–5810, 2019.

72 RAPPAPORT, T. S. *Comunicações sem fio: princípios e práticas*. [S.l.]: Pearson Prentice Hall, 2009.

73 Basu, K.; Nanda, S. An adaptive filtering technique with self-adaptive pso for estimation of non-stationary signals. In: *2016 International Conference on Communication and Signal Processing (ICCSP)*. [S.l.: s.n.], 2016. p. 1057–1061.

74 Rout, N. K.; Das, D. P.; Panda, G. Particle swarm optimization based active noise control algorithm without secondary path identification. *IEEE Transactions on Instrumentation and Measurement*, v. 61, n. 2, p. 554–563, Feb 2012.

75 Krusienski, D. J.; Jenkins, W. K. A modified particle swarm optimization algorithm for adaptive filtering. In: *2006 IEEE International Symposium on Circuits and Systems (ISCAS)*. [S.l.: s.n.], 2006. p. 4 pp.–140.

76 WANG, D.; TAN, D.; LIU, L. Particle swarm optimization algorithm: an overview. *Soft Computing*, Springer, v. 22, n. 2, p. 387–408, 2018.

77 MARINI, F.; WALCZAK, B. Particle swarm optimization (pso). a tutorial. *Chemometrics and Intelligent Laboratory Systems*, v. 149, p. 153 – 165, 2015. ISSN 0169-7439. Disponível em: <http://www.sciencedirect.com/science/article/pii/S0169743915002117>.

78 Chamon, L. F. O.; Ferro, H. F.; Lopes, C. G. A data reusage algorithm based on incremental combination of lms filters. In: *2012 Conference Record of the Forty Sixth Asilomar Conference on Signals, Systems and Computers (ASILOMAR)*. [S.l.: s.n.], 2012. p. 406–410.

79 Hasada, K.; Kawamura, A.; Iiguni, Y. Adaptive line enhancer-based beat noise suppression for fm radio in motor vehicle. In: *2019 International Symposium on Intelligent Signal Processing and Communication Systems (ISPACS)*. [S.l.: s.n.], 2019. p. 1–2.

80 THATO, T. *Digital signal processing algorithms and techniques for the enhancement of lung sound measurements*. Tese (Doutorado) — Loughborough University, 2008.

81 NAKANISHI, I. et al. Frequency domain de-correlation parameter in speech noise reduction system based on frequency domain adaptive line enhancer. In: IEEE. *The 2004 47th Midwest Symposium on Circuits and Systems, 2004. MWSCAS'04*. [S.l.], 2004. v. 2, p. II–II.

82 SHARMA, P.; MACHIWAL, D.; JHA, M. K. Chapter 10 - overview, current status, and future prospect of stochastic time series modeling in subsurface hydrology. In: VENKATRAMANAN, S.; PRASANNA, M. V.; CHUNG, S. Y. (Ed.). *GIS and Geostatistical Techniques for Groundwater Science*. Elsevier, 2019. p. 133 – 151. ISBN 978-0-12-815413-7. Disponível em: <http://www.sciencedirect.com/science/article/pii/B9780128154137000109>.

83 Anderson, C.; Satorius, E.; Zeidler, J. Adaptive enhancement of finite bandwidth signals in white gaussian noise. *IEEE Transactions on Acoustics, Speech, and Signal Processing*, v. 31, n. 1, p. 17–28, 1983.

84 CAMPELO, F.; WANNER, E. F. Sample size calculations for the experimental comparison of multiple algorithms on multiple problem instances. *Journal of Heuristics*, Springer, p. 1–33, 2020.

85 AGILENT. *Network Analyzer Basics*. 2020. <https://www.keysight.com/upload/cmc_upload/All/BTB_Network_2005-1.pdf>. Access: 04/13/2020.

86 POZAR, D. M. *Microwave engineering*. [S.l.]: John Wiley & Sons, 2009.

87 R&S. *RS ZV-Z135 Calibration Kit Specifications*. 2018. <https://scdn.rohde-schwarz.com/ur/pws/dl_downloads/dl_common_library/dl_brochures_and_datasheets/pdf_1/ZV-Z135_dat-sw_en_3606-6828-22_v0102.pdf>. Access: 22-08-2020.

88 GONÇALVES, F. J. F. Medição das propriedades constitutivas eletromagnéticas de materiais na faixa de 1 a 6 ghz pelo método do espaço livre. Universidade Federal de Minas Gerais, 2012.

89 JONES, G. Mobile menace: why sdr poses such a threat. *Network Security*, v. 2012, n. 6, p. 5 – 7, 2012. ISSN 1353-4858. Disponível em: <http://www.sciencedirect.com/science/article/pii/S1353485812700521>.

90 MARQUET, A.; MONTAVONT, N.; PAPADOPOULOS, G. Z. Towards an sdr implementation of lora: Reverse-engineering, demodulation strategies and assessment over rayleigh channel. *Computer Communications*, v. 153, p. 595 – 605, 2020. ISSN 0140-3664. Disponível em: <http://www.sciencedirect.com/science/article/pii/S0140366419314665>.

91 MATHWORKS. *xcorr*. [S.l.], 2020. Disponível em: <https://www.mathworks.com/help/matlab/ref/xcorr.html>.

92 MATHECKEN, P. J. *OFDM under Oscillator Phase Noise*. Tese (Doutorado) — Aalto University, 2016.

93 González, G. et al. Cyclostationary autocorrelation based cfo estimators. In: *2011 19th European Signal Processing Conference*. [S.l.: s.n.], 2011. p. 1623–1627.

94 Nyblom, T. et al. Time-varying carrier offset tracking in ofdm systems using particle filtering. In: *Proceedings of the Fourth IEEE International Symposium on Signal Processing and Information Technology, 2004*. [S.l.: s.n.], 2004. p. 217–220.

95 Mar, J.; Kuo, C.; Chou, S. Sdr structure based cfo estimation and compensation circuit for ofdm systems using reconfigurable cordic fpga modules. In: *2010 IEEE Asia Pacific Conference on Circuits and Systems*. [S.l.: s.n.], 2010. p. 352–355.

Appendix A

VNA and S-Parameters

A.1 VNA basics

The VNA is a 2-port equipment used to characterize a given device by means of power ratios. It has an extensive use in EMC labs. It allows one to characterize a given device as a black-box and therefore without requiring knowledge about its internal circuit. Figure A.1 shows a VNA simplified schematics with a generic device under test.

Based on this diagram, one can note that the VNA has an internal source that can feed both ports, but not simultaneously. Once a given port is linked to the source, the direct

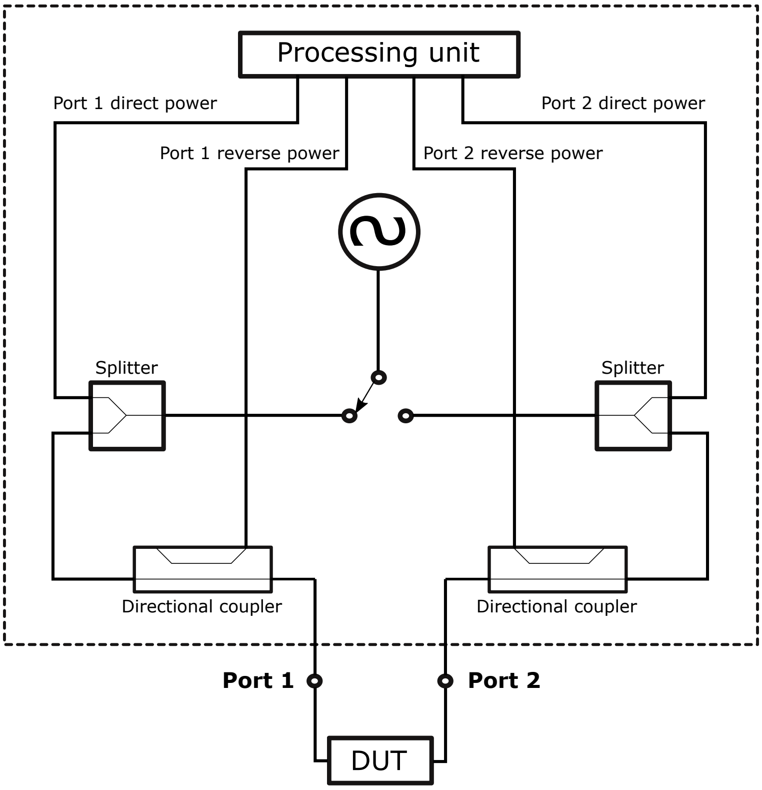

Figure A.1 – Simplified electrical schematics of a VNA. Based on (85).

power flow reaches the DUT by means of a splitter and a directional coupler. A sample of the direct power, whose levels are usually user-controlled, goes to a processing unit through the splitter. On the other hand, a reverse power sample is provided to the processing unit by the directional coupler. The reverse flow is caused by impedance mismatches between the VNA and the DUT. Once the processing unit receives information regarding the direct and reverse power flows from both ports, it calculates several microwave parameters. In this work, we deal with the Scattering Parameters, also known as the S-Parameters.

A.2 S-Parameters

The S-Parameters approach can be applied to N-ports networks, as the one illustrated in Fig. A.2. In this figure, the DUT is represented as a black-box system that interacts with the external devices by means of its N ports. In each port, there can be power flows in both directions, *i.e.* entering or leaving the DUT. Although power is constituted by voltage and current, most modern VNAs compute the S-Parameters via voltage waves flow. The notation adopted is then V_i^+ for the voltage waves that enter the DUT and V_i^- for the voltage waves that leave the DUT through the i^{th} port, $i = 1, 2, ..., N$. Based on this notation, it is possible to define the complex S-Matrix shown in Eq. A.1, as the one that relates the incident voltage waves with the reflected ones (86).

$$\begin{bmatrix} V_1^- \\ V_2^- \\ \vdots \\ V_N^- \end{bmatrix} = \begin{bmatrix} S_{11} & S_{12} & \dots & S_{1N} \\ S_{21} & S_{22} & \dots & S_{2N} \\ \vdots & \vdots & \ddots & \vdots \\ S_{N1} & S_{N2} & \dots & S_{NN} \end{bmatrix} \begin{bmatrix} V_1^+ \\ V_2^+ \\ \vdots \\ V_N^+ \end{bmatrix} \tag{A.1}$$

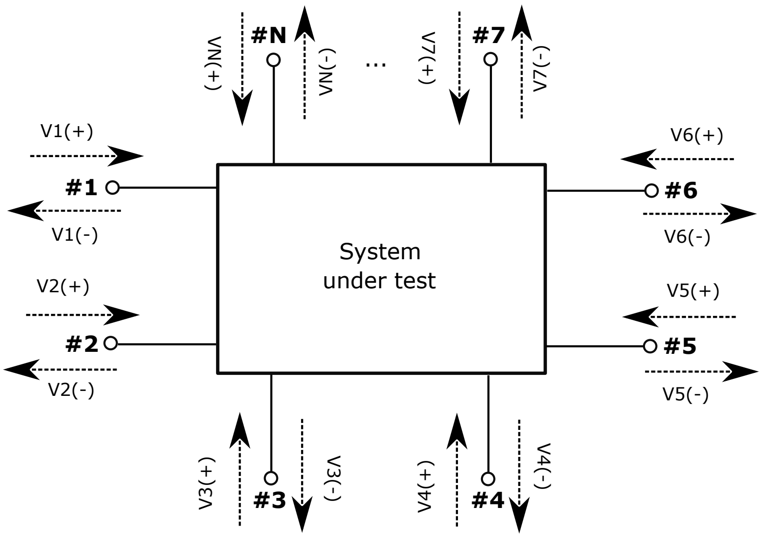

Figure A.2 – Generic microwave network. Based on (86).

Each element of the S-Matrix, S_{ij} ($i = 1, 2, ...N$, $j = 1, 2, ...N$), represents the interation between the i^{th} and the j^{th} ports. The evaluation of these elements can be made by supplying the j^{th} port with power (only this one) and measuring the signal received by the i^{th} port (with all the remaining ones 50Ω-terminated), as described by

$$S_{ij} = \left. \frac{V_i^-}{V_j^+} \right|_{V_k^+=0, k \neq j} . \tag{A.2}$$

Since the VNA has only 2 ports, the S-Matrix from Eq. A.1 is 2 × 2 in this study. More specifically, for the gain estimation in the antenna calibration problem, we only need the magnitude of the S_{12} parameter, also known in other contexts as the *insertion loss* of a device or system. In our investigation, this parameter measures the strength of a radiofrequency (RF) link between two antennas. Furthermore, by following the notation expressed by the Eq. A.2, we consider that the transmitting antenna is connected to the port 2 while the receiving one is attached to the port 1. Another important remark is that the S-Parameters are frequency-dependent complex numbers. Therefore, along this work we will measure and discuss frequency-domain S_{12} magnitude graphs defined along the antennas operating ranges.

A.3 Cable calibration

An important procedure that must be executed before any measurement is the cable calibration. In most cases, the DUT is connected to the VNA input ports with a pair of coaxial cables. These cables can in turn affect the measurements and hide important information about the DUT.

By following a calibration procedure, one takes the cable effects into consideration during a measurement campaign. Therefore, the VNA results will only be due to the DUT. Otherwise, the results would be affected by the attenuation, propagation delay and reflections introduced by the coaxial cables. Nevertheless, the cancellation of such effects is only possible if a calibration kit is available (it is usually sold together with the VNA).

Figure A.3 shows a typical VNA calibration kit. It contains the following terminals: short, open, thru and match. Each of them represents a certain standard impedance. The short and open cases are straightforward, representing very low and very high impedances, respectively. Thru means a direct connection between the VNA ports 1 and 2. Finally, the match termination is a 50Ω load. More precise specifications can be found on the calibration kit datasheet.

To start the calibration procedure, one shall access the corresponding software environment using the VNA graphical interface. After then, one can start calibrating each port, individually. To do so, one can connect the open, short or match terminal to

Figure A.3 – A typical VNA calibration kit. It contains five terminals: short, open, thru (two terminals) and match. Source: (87)

the VNA port 1 or 2. For each of these six connections, a set of four graphs is obtained. They represent the S_{11}, S_{12}, S_{21} and S_{22} parameters behaviors of the (VNA + cable) measurement system along the specified frequency range. Evidently, the S_{12}, S_{21} values will be negligible once there is no physical connection between the VNA ports. The S_{11} and S_{22} curves are stored so the DUT reflection measurements can be more accurate.

After then, it becomes necessary to establish a direct connection between the ports. To do so, one shall use the *thru* connection. In this case, the S_{12}, S_{21} curves are stored so the attenuations and propagation delays introduced by the cables can be taken into account in future DUT measurements.

Based on the microwave theory, one can check the consistency of all the calibration results, *e.g.* very low reflections are expected for the *load* condition. Some illustrative examples of the VNA calibration procedure can be found in (88).

Appendix B

SDR-based experiments

B.1 SDR basics

SDR is a concept that dates back to the 1970s, being initially developed by military and intelligence agencies (89). Nevertheless, its spread use has increased given the relatively low prices of computers and related devices. SDR systems are those capable of transmitting, receiving and processing radiofrequency signals mainly via software (in opposition to traditional systems, which are hardware-based in essence).

According to (90), SDR can be an interesting answer to *cognitive radio* systems needs. The cognitive radio concept is related to smart devices which are able to sense the environment, cooperate with each other and optimize the spectrum sharing and energy consumption. Since most of these tasks involve software, SDR systems become especially appropriate.

The SDR concept brings many advantages with it. For instance, the process of generating, capturing and dealing with high-frequency signals becomes cheaper, the hardware configuration and re-configuration becomes simpler (thus increasing flexibility for different applications) and it acquires mobility, becoming suitable for *in situ* experiments. Nevertheless, SDR systems can be used with bad purposes as well. According to (89), the easiness of use and accessible prices are particularly attractive features for hackers who want to attack communication systems.

B.2 Test setup

In order to analyse the performance of the ASP-2 algorithm in a more realistic scenario, we ran a few experiments using a software-defined radio (SDR) system. Figure B.1 illustrates the equipment used to emulate a GSM-R link under IEMI in Lab2: a computer equipped with an open-source software called GNU Radio, a set of transmission/reception units (model: HackRF One) and a jammer.

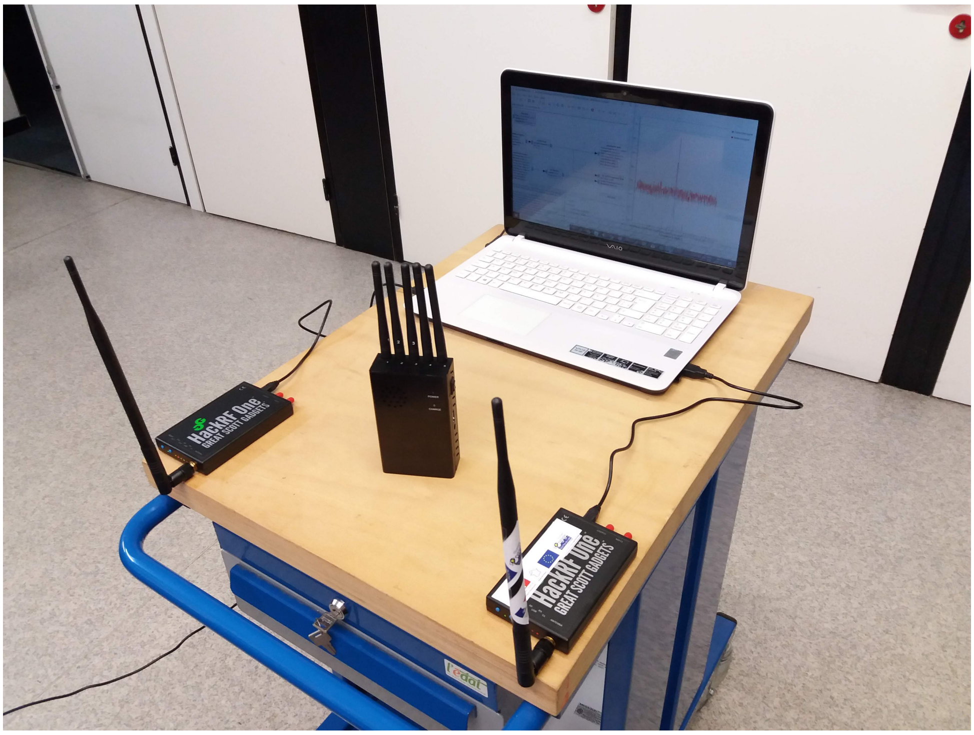

Figure B.1 – SDR-based test setup used to emulate a GSM-R communication link corrupted by IEMI. Equipment: a computer with a signal processing toolbox, a transmitting/receiving set and a jammer.

Unfortunately, we had problems with these measurements. This conclusion is based on the fact that the BER was near 50 % even with the jammer turned off. We attribute such issues to the available hardware. The main problem is related to a frequency asynchrony between the transmitter and receiver local oscillators, also known as carrier frequency offset (CFO). This and other hardware problems are described in Section B.3.

Here, we give the details concerning the test setup from Fig. B.1. The distance between the transmission and reception units is 40 cm. One the other hand, the jammer is placed in three different locations so we can reproduce distinct SJR conditions. The distances from the jammer to the other devices are 20 cm, 140 cm and 300 cm. For the last condition (300 cm), the jammer is put inside a gigahertz transverse electromagnetic (GTEM) cell. This is done with the main purpose of managing the SJR, once the jamming device used during this investigation offers no power control.

The configuration of GNU Radio for data acquisition is illustrated in Figure B.2. All these blocks are built-in structures with open-source Python or C++ codes. The *file source* block contains a binary file which is later on transformed in a complex time-domain signal after the *GMSK mod* block. For this investigation, we load the *file source* block with the following binary sequence: 11100. Then, we configure it to periodically supply the *GMSK mod* block with this sequence. The complex output of the modulation block

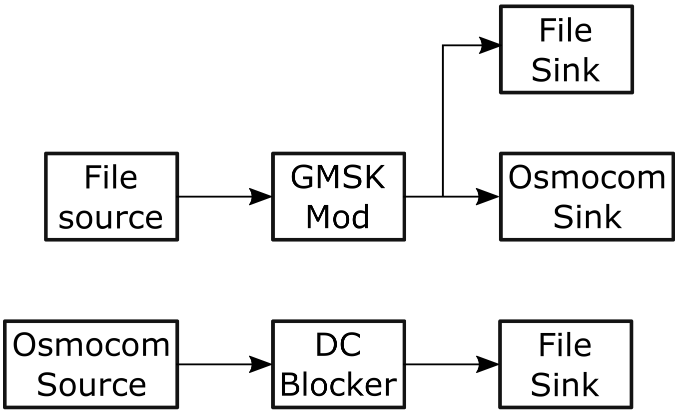

Figure B.2 – Block diagram illustrating the way GNU Radio was configured for data transmission and acquisition.

corresponds to the base-band in-phase and quadrature (IQ) components of a GMSK signal. After then, the complex base-band signal is up-converted to the modulation band by the *osmocom sink* block.

The *osmocom sink* and *osmocom source* blocks are used to establish communication with the transmitting and receiving hardware, respectively. They convert base-band in modulation-band signals and vice-versa. It means that, with the exception of *osmocom sink* and *osmocom source*, all the other blocks from Fig. B.2 operate in base-band. In our experiments, we consider the modulation band to be centered around 923 MHz with a bandwidth of approximately 200 kHz.

After the *osmocom source* block, we use a *DC blocker* to eliminate any vertical shift present in the time-domain representation of the received signal as a result of the modulation/demodulation processes. We also use *file sink* blocks to store time-domain samples of the complex base-band transmitted and received signals. These samples are used in a second GNU Radio file containing our signal processing Python code.

It is important to stress the role played by the bench tests in the validation of our methodology. During this stage, we noticed three phenomena that were not captured during the simulations: block processing effects, time-varying CFO and random noise floor. With the exception of the noise floor, each of them is separately detailed in the next sub-sections. We expect that the adaptive line enhancer, to be introduced in Chapter 4, can attenuate the random noise floor.

B.3 Issues

From now on, we describe the main problems we faced during the SDR-based experiments and our trials to mitigate them. Even though we could not use the measurements to analyze the ASP-2 technique, we believe that sharing our experience can help

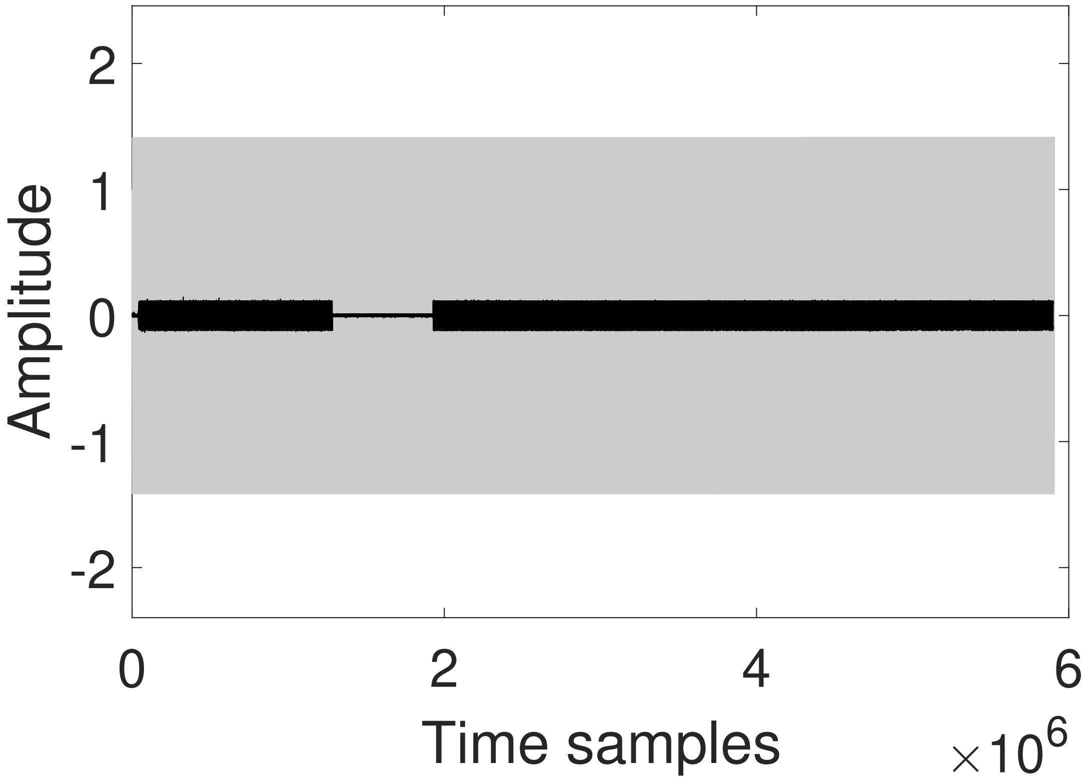

Figure B.3 – Raw data provided by the *file sink* block from Fig. B.2. The gray and black curves represent the transmitted and received signals, respectively. The two intervals with null amplitude values in the black curve are attributed to block processing delays.

other researchers interested in the SDR technology.

B.3.1 Block processing effects

GNU Radio is a block processing-based software. It means that each block (for example, those from Fig. B.2) has a buffer with a user-defined size. Each block uses a buffer to temporarily store one signal segment at a time and process it before sending information to the next structure. Therefore, each block introduces a delay.

In order to better understand how this software property can affect our measurements, we first take the raw data provided by the *file sink* blocks from Fig. B.2, as illustrated in Fig. B.3. This figure shows the transmitted and received signals. It reveals two distinct time intervals with null amplitude values, both attributed to block processing delays. The first one is better seen in Fig. B.4a.

Another consequence of the GNU Radio block processing scheme is illustrated in Fig. B.4b. The transmitted signal has more samples than the received one. Since this software offers no control over the data acquisition duration (it is not possible to precisely

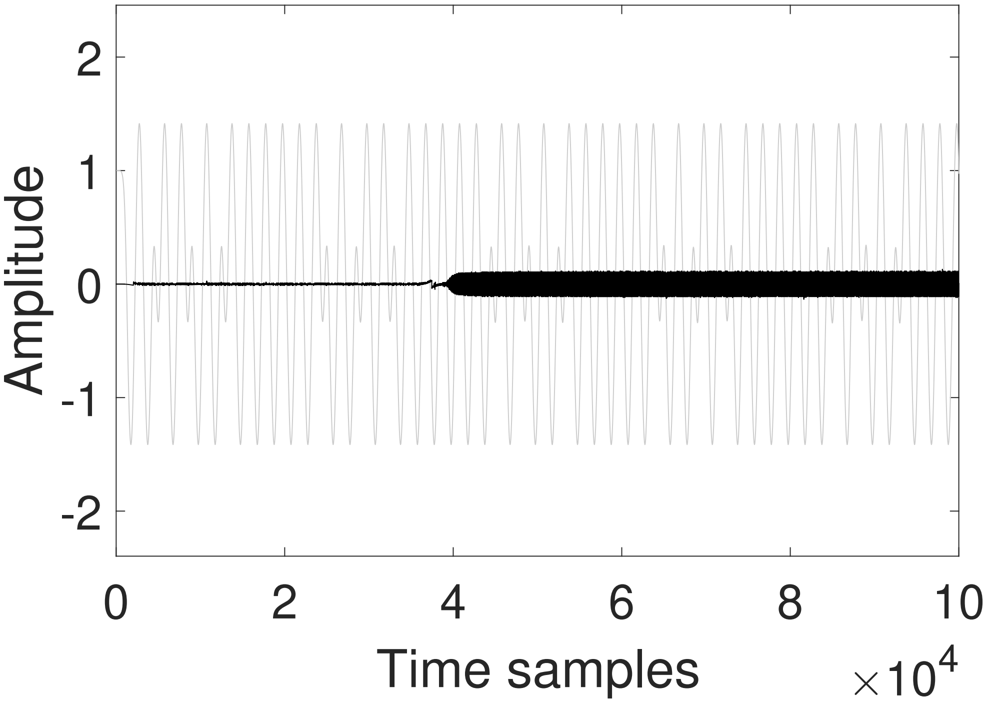

(a)

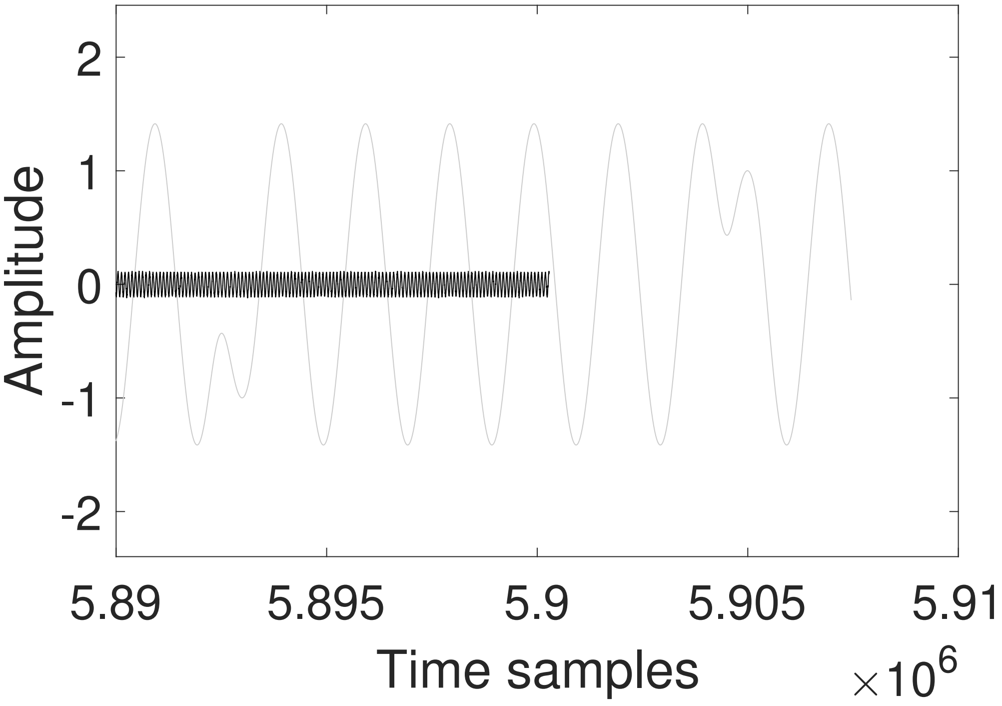

(b)

Figure B.4 – Zoomed views of Fig. B.3, highlighting the transmitted and received (a) initial and (b) final signal segments. In particular, (b) shows that, at the end of the data acquisition process, more samples of the transmitted signals than of the received one were registered. The gray and black curves represent the transmitted and received signals, respectively.

set the initial and final time instants), this process has to be manually ended. When this happens, the *file sink* block located at the transmitter side in Fig. B.2 already registered some signal samples that did not arrive yet at the receiver *file sink*.

To minimize these block processing effects, we propose an approach which is based on the following cross-correlation estimator (91)

$$\hat{R}_{xy}(m) = \sum_{n=0}^{N-m-1} x_{n+m} y_n^* \tag{B.1}$$

where x and y are random processes samples, * means complex conjugation, $-\infty < n < \infty$ is the discrete-time index, N is the sample size and $m \geq 0$ is the lag between x and y (with even symmetry assumption). This is a statistical function that reveals the similarity level between two signals by means of their internal product. An interesting aspect of this function is that it can identify "hidden" patterns shared by these two signals but not easily detectable through visual inspections. To do so, one signal remains "still" (y in Eq. B.1) where the other one (x in Eq. B.1) "slides" back and forth. Every time a similarity is detected, a cross-correlation peak can be noted.

As a last remark on Eq. B.1, we highlight that a good estimate of the corresponding true value, *i.e.* $\mathbb{E}(\hat{R}_{xy}(m))$, is only available when N is large and a great amount of realizations is possible. Nevertheless, we do not need a faithful representation of the random processes behavior but only the shift between a particular pair of transmitted and received signals. Therefore, we only evaluate Eq. B.1 once for a given pair of signals.

In this work, we use Eq. B.1 to identify the lags between the transmitted and received signals caused by the block processing scheme. With this information, we can shift one of them and re-align the sequences. The first step is to select one segment from each signal from Fig. B.3 and eliminate the other samples. Some observations might be done at this point. The first is that these segments must have the same length. And the second is that the size of these segments must be sufficient for the further analyses. During this investigation, we select segments with 10^6 samples, which we judge to be enough for the further BER calculations. Finally, we apply the proposed CFO mitigation technique (to be detailed in the next sub-section) to the selected signals segments.

Then, we calculate the cross-correlation function and plot it according to the lags. Such a domain represents phase delays and advances (positive and negative lags, respectively). So if we apply a maximization operator to the resulting cross-correlation vector, we can identify its peak value and the corresponding index (*i.e.* lag) as well. This is the information needed to re-align the signals. This process is illustrated in Fig. B.5, where we show both a complete and a zoomed view of the cross-correlation between the signals from Fig B.3, after the pre-conditioning procedures exposed in the previous paragraph. In

Fig. B.5b, it is possible to identify a lag of 100 samples between them.

B.3.2 Carrier frequency offset

The previously reported block processing phenomenon is just a part of a bigger set of undesirable effects coming from our measurement system. The signals shown in Figs. B.3 and B.4 reveal another important issue. The received signal clearly presents much higher frequency content than the transmitted one. Furthermore, if we increased more the zoom on the received signal, we would realize that most of the GMSK phase transitions were lost. We attribute these problems to the CFO phenomenon.

The CFO is a synchrony issue which is usually noticed during the signal reception process. It generally happens when the transmitter and receiver local oscillators are not exactly tuned to the carrier frequency. In these cases, they are not only out of sync with the carrier but also one with another. Besides, this offset can vary randomly over time. As a result, the signal reconstitution at the receiver can be severely compromised.

Reports on the CFO effects over communication systems can be found on the literature. As an example, one can cite the orthogonal frequency division multiplexing (OFDM) systems, where the CFO can affect the sub-carriers spacing (92; 93). The CFO tracking and cancellation can become even more challenging when it is time-varying, *e.g.* in some fast mobile receivers that experience Doppler effect (94). In this work, we are mainly concerned about the time-varying CFO effects over SDR systems (95). Indeed, this sort of issue is common in SDR devices and questions on how to deal with it are frequently found in users forums.

Most state-of-the-art CFO canceling techniques are designed for real-time systems, where the receiver has to quickly predict the CFO (which comes from a random process) before canceling it (93; 95; 94). In these cases, the prediction stage usually requires complex mathematical manipulations over the received signal or specific circuitry. Since we deal with offline signal processing, we do not need to predict but only recover the random CFO oscillations. Therefore, we propose a computationally simple approach aiming to analyze the filters performances regardless of the CFO. Our approach is based on the short-time Fourier transform (STFT).

The proposed CFO mitigation technique is based on the frequency *versus* time grid provided by the STFT. Two grids are obtained: one for the transmitted signal and another one for the received waveform. The first stage consists on identifying the instantaneous offset between these signals. To do so, we apply the cross-correlation methodology (described in the previous sub-section) within every time-domain window. The output of this stage is an offset *versus* time curve, as illustrated in Fig. B.6. In this figure, time is expressed in terms of window index. This important parameter will be soon detailed. Both curves

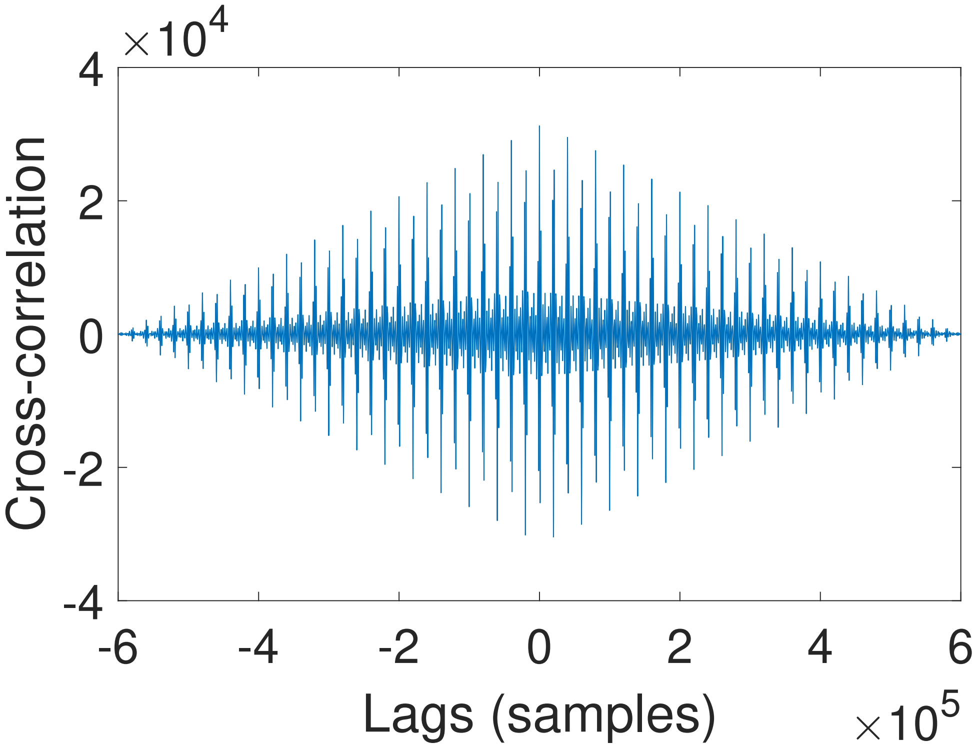

(a)

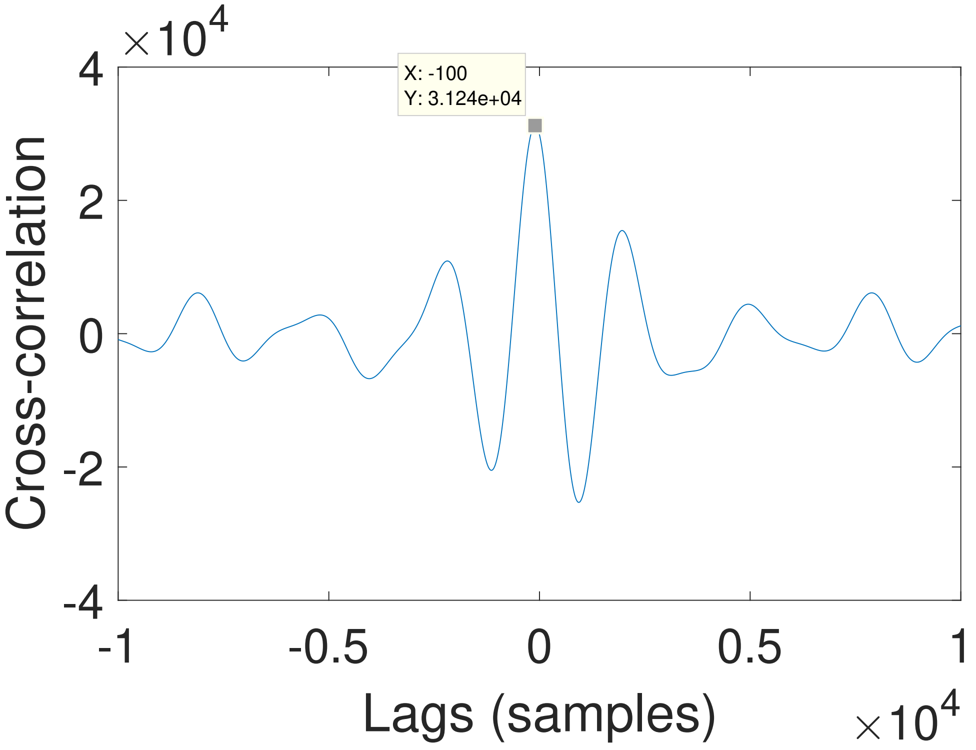

(b)

Figure B.5 – Cross-correlation between a given pair of transmitted and received signals. (a) Entire lags domain. (b) Zoomed view close to lags=0, evidencing a shift of 100 samples between the signals.

from Fig. B.6 reveal offset oscillations around 11.5 kHz. Such an information is used in the second stage, which consists on the CFO cancellation.

In our first CFO cancelling trial, we embedded the offset curve into cosine and sine waves. This creates frequency-modulated local oscillators, which are used in a GMSK demodulation process (in addition to the already existent one) that aims to bring the shifted signals back to 0 Hz. Nevertheless, the results were not satisfactory. We attribute this unsatisfactory performance to the fast changes observed in some offset curves (see, for example, the offset transitions in Fig. B.6). This sort of behavior resulted in discontinuities on the local oscillator waveforms, turning them into non-sinusoidal signals. We then decided to assume a controlled error in the CFO cancellation process in order to create harmonic local oscillators. To achieve that, we developed an automatic procedure that identifies the most recurrent offset value present in a signal sample.

The most recurrent offset estimation is based on histograms. This sort of statistical representation is taken from the offset *versus* time curves obtained in the previous stage. It allows us to identify which offset frequency is more recurrent between a given pair of transmitted and received waveforms. Figure B.7 shows the histograms obtained from the offset curves illustrated in Fig. B.6. They reveal that the most recurrent offset between this particular pair of transmitted and received signals is approximately 11.52 kHz. The histograms from Figs. B.7a and B.7b have some differences, which are related to the STFT window size. Nevertheless, the most recurrent offset estimates are very similar.

An important aspect of the histograms from Figs. B.7a and B.7b is that they are very refined in terms of frequency resolution. This means that each bar is associated with a very small range of values (these ranges are also known as *bins*). We do this because we are interested in single offset values, so we need to refine the first raw histogram.

From the histogram, we create local harmonic oscillators tuned to the most recurrent frequency and then we apply the GMSK demodulation. As a drawback, we do not compensate the received signal for all the offsets but, on the other hand, we ensure perfectly sinusoidal local oscillators.

Finally, it is important to highlight the role played by the STFT window size design in our methodology. In general, this parameter defines a trade-off between time and frequency-domain resolutions. An optimum length can usually be defined when we previously know the signal behavior. In our investigation, the offset dynamics is random so the window design becomes challenging. As a consequence, the optimal length can differ from one signal sample to another.

To address this issue and automate the offset identification and mitigation processes, we create a script that evaluates 101 possible windows for each pair of transmitted and received signals. Their sizes range from 20000 to 30000 samples with a step of 100.

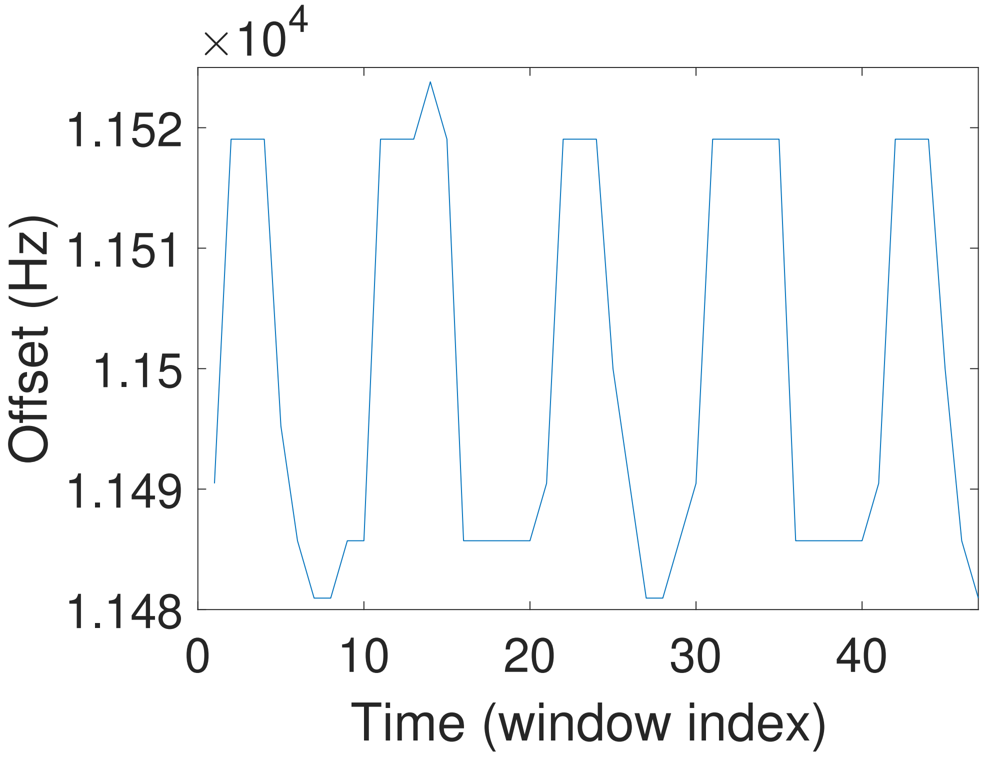

(a)

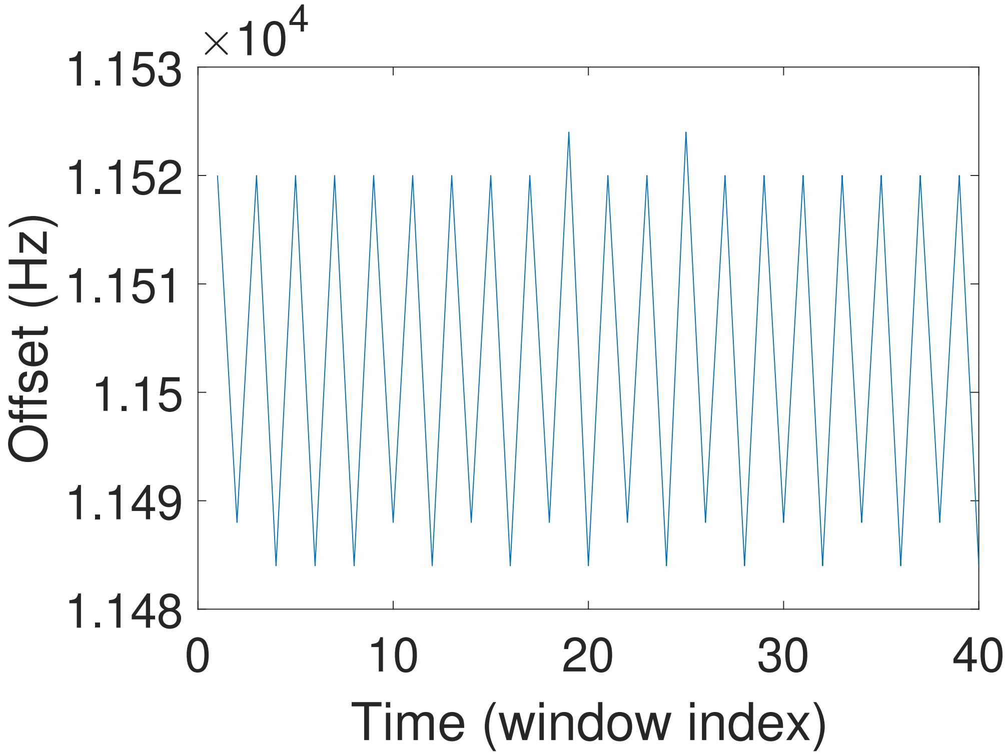

(b)

Figure B.6 – Instantaneous offset between a given pair of transmitted and received signals obtained with a STFT. (a) Window size = 21×10^3 samples. (b) Window size = 25×10^3 samples.

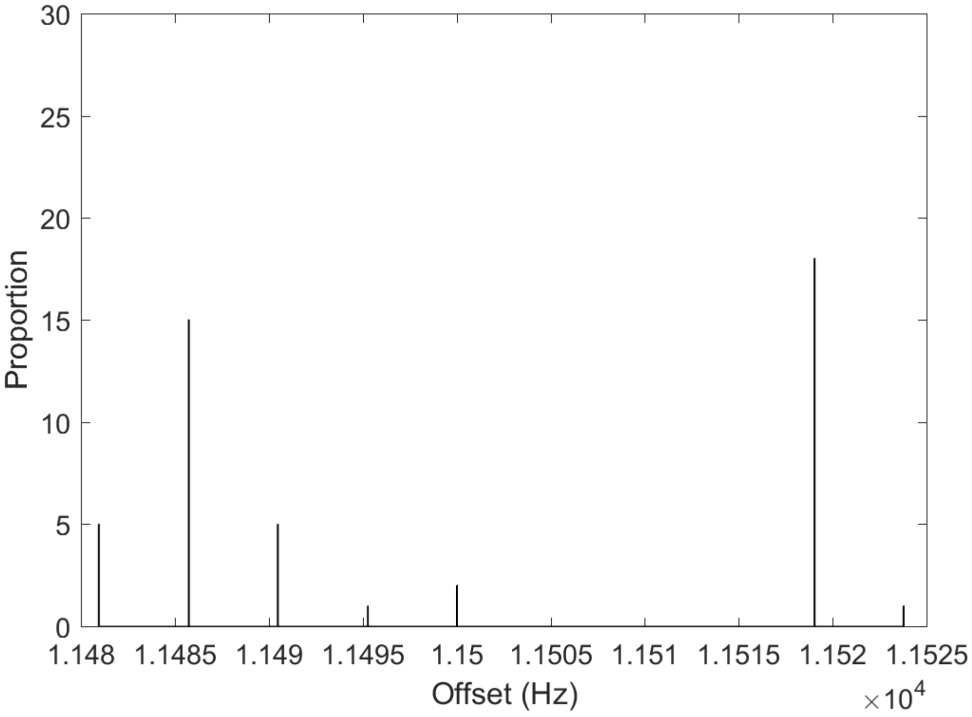

(a)

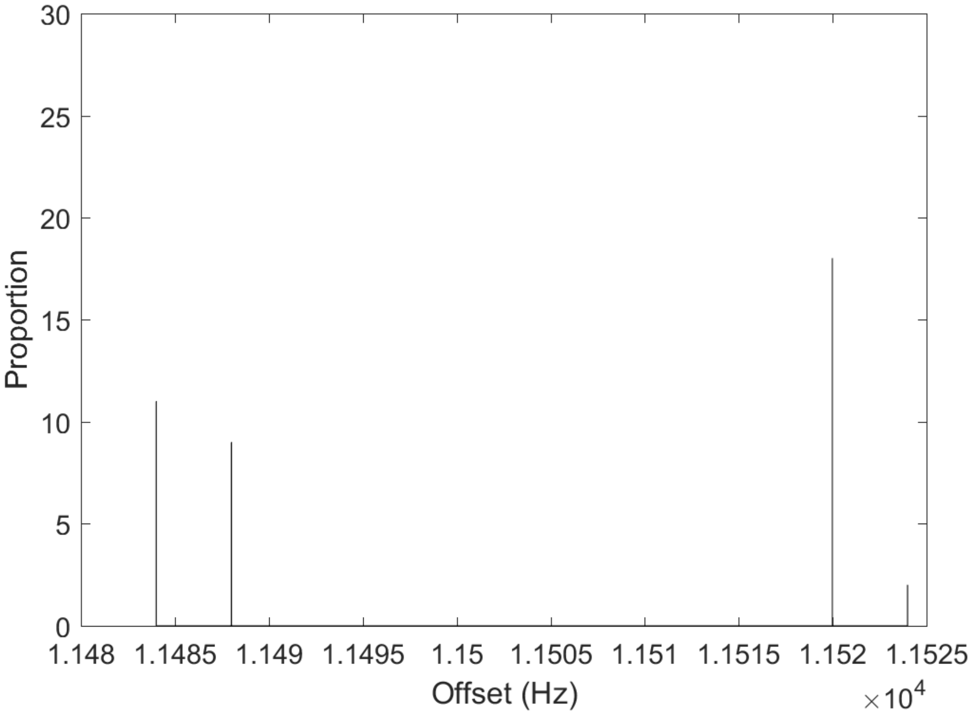

(b)

Figure B.7 – Histograms evidencing the most recurrent offsets between a given pair of transmitted and received signals. They were obtained from the offset curves illustrated in Fig. B.6. (a) Window size $= 21 \times 10^3$ samples. (b) Window size $= 25 \times 10^3$ samples.

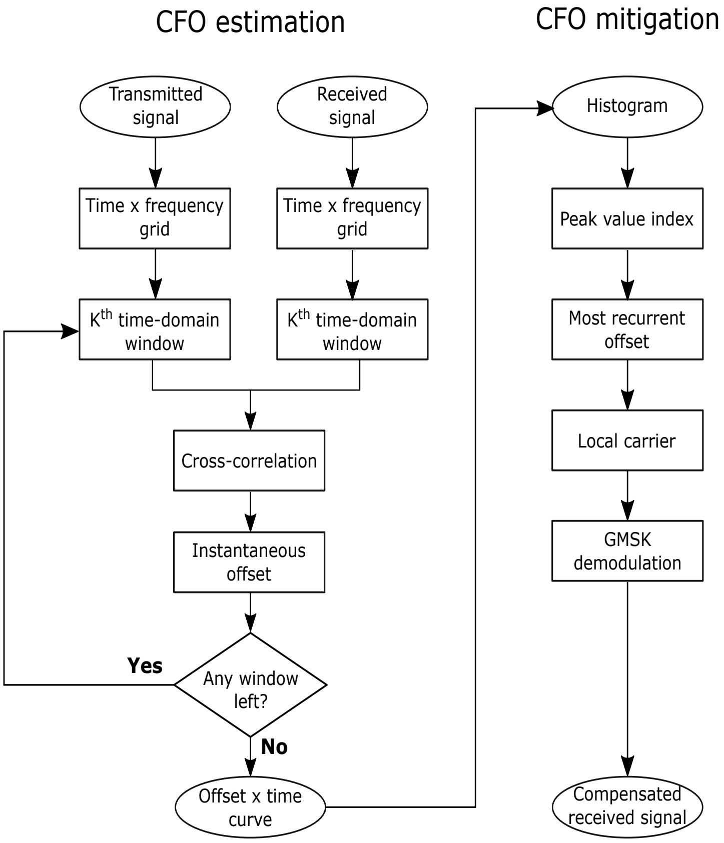

Figure B.8 – Summary of the proposed CFO estimation and mitigation techniques. This procedure is run for every pair of transmitted and received signals samples.

Each window size results in a certain offset estimate. Each of these estimates in turn generates an offset correction that results in a certain BER reduction. We define this performance metric as the difference between the received signal BER prior and after the CFO mitigation. Finally, the chosen window length is the one that produces the smallest BER. Figure B.8 summarizes the whole CFO mitigation technique by means of a flowchart.

B.3.3 SDR-based tests

To run the SDR-based experiments, we use the test setup from Fig. B.9. In this illustration, it is possible to see not only the equipment but also the signal flow and other information. As a first step, a binary sequence is generated by the software installed in the laptop from Fig. B.9 (GNU Radio). The same software modulates this sequence, generating a complex IQ signal in the time domain. This signal is a simple model for the GSM-R communication between train and base-station. Once generated by GNU Radio, it is then sent to the transmitting unit, which consists in an electronic circuit with an external antenna. This process continues until we manually stop the bits generation.

In a second moment, the signal captured by the receiver is stored in the laptop. In this particular arrangement, we used the same laptop to generate and receive the signal. These signal records refer to the complex IQ signal at the receiver level. They are used for

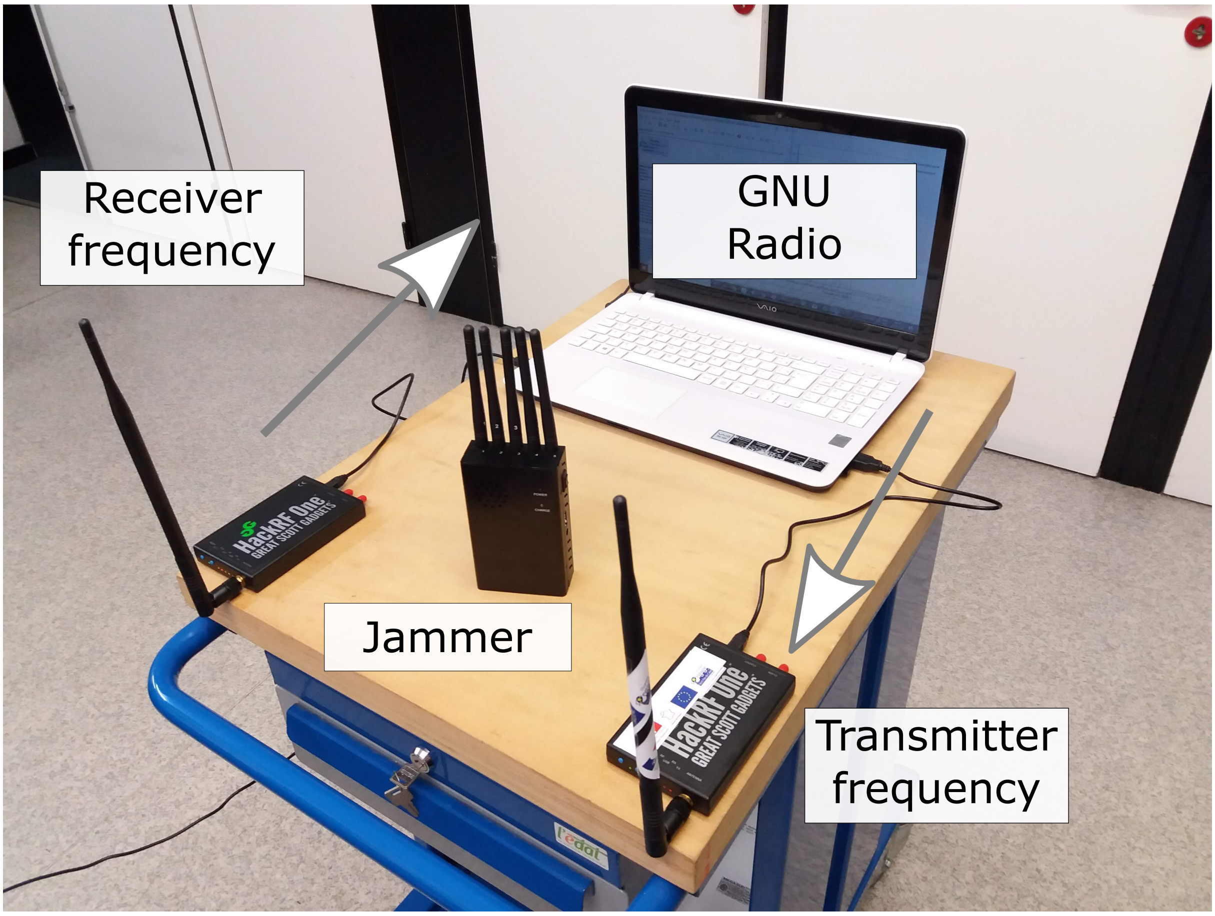

Figure B.9 – Illustration of the signal flow inherent to the SDR-based experiments performed during this investigation. This figure highlights GNU Radio, which is the software used to generate and receive the signals, the jammer device used to introduce noise to the communication process and the transmitter and receiver frequencies, which are related to the CFO problem.

the offline filtering process and for further demodulation and BER calculation. This whole process is run 10 times with the jammer located inside a shielded device, 300 cm distant from the transmitter and receiver set. During this process, we used an ALE filter with the following parameters: step-size=0.0001, length = 100, Δ=250 and number of copies for data reuse = 1.

An important issue we faced during this stage is related to the frequencies used during the transmission and reception processes. For a successful communication, it is necessary that the transmitter and receiver frequencies are the same. Otherwise, a *beat frequency*, which is equal to the difference between the mentioned frequencies, can cause problems to the signal recovering process at the receiver. If this frequency offset is constant over time, then a new down-conversion stage (which is essentially a local oscillator tuned to the beat frequency and a mixer) can fix this problem. Unfortunately, we noticed a randomly time-varying carrier frequency offset, CFO, which severely compromised the communication. As a result, the BER was excessively high, reaching average levels of

Table B.1 – Effects of the proposed CFO adjustment over the SDR-based GSM-R communication without jamming, in terms of BER.

Sample	BER before adj. (%)	Adj. (kHz)	BER after adj. (%)	Adj. gain (%)
1	49.85	11.5217	28.95	20.9
2	50.3	11.5233	38.05	12.25
3	51.2	11.5233	35.45	15.75
4	52	11.4917	30.35	21.65
5	50.15	11.4900	32.15	18
6	48.9	11.4850	32.15	16.75
7	50.1	11.4867	35.95	14.15
8	48.85	11.4517	44.85	4
9	50.05	11.4867	34.3	15.75
10	48	11.4900	38.25	9.75
Mean	49.94	11.4950	35.045	14.90
Std. dev.	1.16	0.0223	4.63	5.26

50% even with the jammer off. In an attempt to mitigate this undesirable effect, we developed a methodology which is described in Appendix B. Unfortunately, even with this methodology we were not able to fully mitigate the CFO effects. This compromised the ASP-2 evaluation, as discussed in the following paragraphs.

The CFO mitigation efficiency is summarized in Table B.1. According to this table, the BER before the adjustment is close to 50%, meaning no reliable communication. After the CFO compensation, an average gain of 14.9% is observed. At this point, two important aspects shall be highlighted. First, the number of decimal digits in the third column from Table B.1 indicates the sensitivity of the proposed CFO compensation technique to small frequency changes. During our analyses, we observed that a few Hz of difference from the optimal values are sufficient to deteriorate the CFO compensation gain. The second aspect is the BER standard deviation increase, which is equal to 3.5% (compare the second and fourth columns of Table B.1, last line). This can be explained by the fact that the performance of the proposed technique can vary according to the offset behavior in a given signal sample. The CFO compensation is better when the period during which the offset frequency is constant predominates. If most of the times the offset frequency keeps on changing, our approach can lose performance. An alternate in this case would be to collect many signal samples and keep only those who attend these requirements.

We proceed with the signal analysis, but now with the IEMI effects. Tables B.2 and B.3 evidence the CFO and filter gains, respectively, in terms of BER reduction. Again, the raw measurement data indicate a non-reliable communication scenario with a 49.81% average BER. The pre-conditioning stage ensures a 11.41% gain. When compared to the no jamming scenario, we note a performance decrease of 3.48%, indicating that the IEMI can limit the offset estimates. This Table also evidences a 5.15% average filter gain, which

Table B.2 – Effects of the proposed CFO adjustment over the SDR-based GSM-R communication with jamming, in terms of BER. Jammer distance from the SDR system: 300 cm.

Sample	BER before adjustment (%)	Adjustment (kHz)	BER after adjustment (%)	Adjustment gain (%)
1	49.45	11.4867	34.2	15.25
2	50.4	11.4900	33.5	16.9
3	53.6	11.4900	37.85	15.75
4	49	11.4900	40.9	8.1
5	49.35	11.4900	43	6.35
6	48.85	11.4900	43	5.85
7	49.75	11.4950	41.9	7.85
8	49.45	11.4917	39.1	10.35
9	48.95	11.4933	31	17.95
10	49.31	11.4950	39.44	9.87
Mean	49.81	11.4912	38.389	11.42
Std. dev.	1.40	0.0026	4.20	4.60

produces an average BER of 33.24%. This is similar to the 35.05% BER level observed after the CFO adjustment without jamming. Such a behavior was already expected, since the filter can eliminate the IEMI but not the CFO. Again, we note a BER standard deviation increase of approximately 4% in each stage for the same previously discussed reasons.

Unfortunately, these standard deviation increases can limit our analyses. In Table B.2, the BER sample mean and standard-deviation before the adjustment define the following range of values: $49.81\% \pm 1.40\%$. This range changes to $38.389\% \pm 4.20\%$ with the proposed CFO mitigation technique. Since these regions do not overlap, we can state that this stage introduces an actual BER gain. Nevertheless, if we compare the PDFs before and after the filter, we notice an overlap between the one standard deviation confidence intervals ($38.389\% \pm 4.20\%$ before the filter and $33.24\% \pm 7.58\%$ after it).

As a last remark on the Table B.3 data, we highlight the presence of an outlier. A careful look at the fourth sample, last column, reveals a negative filter gain. This indicates a BER increase introduced by the filter. This can eventually happen since the adaptive filter is highly dependent on the input signal autocorrelation behavior. Such a statistical property, on the other hand, is influenced by the random CFO. Therefore, in the mentioned case, the chosen value of Δ no longer produces the decorrelation effects to which it was initially conceived.

Table B.3 – Effects of the filter over the SDR-based GSM-R communication with jamming, in terms of BER. Jammer distance from the SDR system: 300 cm.

Sample	BER without the filter (%)	BER with the filter (%)	Filter gain (%)
1	34.2	22.1	12.1
2	33.5	24.3	9.2
3	37.85	32.25	5.6
4	40.9	46.3	-5.4
5	43	40.7	2.3
6	43	39.1	3.9
7	41.9	35.7	6.2
8	39.1	34.4	4.7
9	31	27.3	3.7
10	39.44	30.25	9.19
Mean	38.389	33.24	5.15
Std. dev.	4.20	7.58	4.78

B.4 Other results

Finally, we show the remaining results concerning the measurements taken with the jammer at 140 cm and 20 cm from the test setup. These results can be seen in Tables B.4, B.5, B.6 and B.7. In the 140 cm case, the CFO mitigation presented almost the same performance as the previous one obtained with 300 cm, reaching an average gain of 12.7%. The cascade effect of CFO mitigation and filtering allowed the signal to return to the same BER level of 35% from the no-jamming case (compare the fourth column of Table B.1 with the third one from Table B.5). On the other hand, we notice a reduction from 12.7% to 5.2% of CFO mitigation performance when we compare the 140 cm and 20 cm cases. Furthermore, the filtering stage presented a negative average gain of -2.62%. This suggests that our approach might not work properly if the jammer device is very close to the GSM-R transmitter or receiver.

The same comments about the PDFs overlapping made for the 300 cm case can be extended to the 140 cm distance. For the 20 cm case, there is a very small difference between them before and after the filter, suggesting that the it can degrade the BER.

Table B.4 – Effects of the proposed CFO adjustment over the SDR-based GSM-R communication with jamming, in terms of BER. Jammer distance from the SDR system: 140 cm.

Sample	BER before adjustment (%)	Adjustment (kHz)	BER after adjustment (%)	Adjustment gain (%)
1	49.40	11.4767	38.15	11.25
2	46.5	11.4750	45.05	1.45
3	46.2	11.4733	37.55	8.65
4	50.7	11.4750	29.3	21.4
5	50.8	11.4767	38.7	12.1
6	50.39	11.4783	38.89	11.5
7	50.55	11.4783	37.3	13.25
8	49.2	11.4750	40.5	8.7
9	49.7	11.4783	25.3	24.4
10	49.95	11.4783	35.65	14.3
Mean	49.34	11.4765	36.64	12.7
Std. dev.	1.67	0.0018	5.60	6.48

Table B.5 – Effects of the filter over the SDR-based GSM-R communication with jamming, in terms of BER. Jammer distance from the SDR system: 140 cm.

Sample	BER without the filter (%)	BER with the filter (%)	Filter gain (%)
1	38.15	35.55	2.6
2	45.05	50.05	-5
3	37.55	33.05	4.5
4	29.3	26.3	3
5	38.7	42.9	-4.2
6	38.89	18.67	20.22
7	37.3	50.45	-13.15
8	40.5	36.7	3.8
9	25.3	24.3	1
10	35.65	37.65	-2
Mean	36.64	35.56	1.08
Std. dev.	5.60	10.52	8.62

Table B.6 – Effects of the proposed CFO adjustment over the SDR-based GSM-R communication with jamming, in terms of BER. Jammer distance from the SDR system: 20 cm.

Sample	BER before adjustment (%)	Adjustment (kHz)	BER after adjustment (%)	Adjustment gain (%)
1	50.75	11.4800	45.6	5.15
2	49.4	11.5133	45.05	4.35
3	48.9	11.5283	45.8	3.10
4	51.25	83.0033	45.6	5.65
5	52.05	86.8867	44.35	7.70
6	47.90	67.3300	45.25	2.65
7	50.5	11.6617	44.75	5.75
8	53.55	78.9317	44.9	8.65
9	50.4	69.5067	45.4	5
10	49.3	11.4767	45.4	3.9
Mean	50.4	44.3318	45.21	5.19
Std. dev.	1.64	35.0324	0.4471	1.8863

Table B.7 – Effects of the filter over the SDR-based GSM-R communication with jamming, in terms of BER. Jammer distance from the SDR system: 20 cm.

Sample	BER without the filter (%)	BER with the filter (%)	Filter gain (%)
1	45.6	47.5	-1.9
2	45.05	48.15	-3.1
3	45.8	47.5	-1.7
4	45.6	49.7	-4.1
5	44.35	49	-4.65
6	45.25	44.5	0.75
7	44.75	48.4	-3.65
8	44.9	47.5	-2.6
9	45.4	48.3	-2.9
10	45.4	47.75	-2.35
Mean	45.21	47.83	-2.62
Std. dev.	0.4471	1.3718	1.51